



저작자표시-비영리-변경금지 2.0 대한민국

이용자는 아래의 조건을 따르는 경우에 한하여 자유롭게

- 이 저작물을 복제, 배포, 전송, 전시, 공연 및 방송할 수 있습니다.

다음과 같은 조건을 따라야 합니다:



저작자표시. 귀하는 원저작자를 표시하여야 합니다.



비영리. 귀하는 이 저작물을 영리 목적으로 이용할 수 없습니다.



변경금지. 귀하는 이 저작물을 개작, 변형 또는 가공할 수 없습니다.

- 귀하는, 이 저작물의 재이용이나 배포의 경우, 이 저작물에 적용된 이용허락조건을 명확하게 나타내어야 합니다.
- 저작권자로부터 별도의 허가를 받으면 이러한 조건들은 적용되지 않습니다.

저작권법에 따른 이용자의 권리는 위의 내용에 의하여 영향을 받지 않습니다.

이것은 [이용허락규약\(Legal Code\)](#)을 이해하기 쉽게 요약한 것입니다.

[Disclaimer](#)

**A Dissertation for the Degree of Doctor of Philosophy
in Mechanical and Automotive Engineering**

**Crystal Plasticity Finite Element Analysis of Formability
and Deformation Behavior in Ultra-thin Steel Sheet
for Fuel Cell Bipolar Plate**

**School of Mechanical Engineering
Graduate School
University of Ulsan**

By

Minh Tien Tran

Advisor Professor Doo-Man Chun

Co-advisor Professor Dong-Kyu Kim

August 2022

**Crystal Plasticity Finite Element Analysis of Formability
and Deformation Behavior in Ultra-thin Steel Sheet
for Fuel Cell Bipolar Plate**

Advisor Professor Doo-Man Chun

Co-advisor Professor Dong-Kyu Kim

**Submitted to
the Graduate School of the University of Ulsan
in Partial Fulfillment of the Requirements
for the Degree of
Doctor of Philosophy in Mechanical and Automotive Engineering**

August 2022

**School of Mechanical Engineering
Graduate School
University of Ulsan**

**By
Minh Tien Tran**

To Approve the Submitted Dissertation for the Degree of
Doctor of Philosophy in Mechanical and Automotive Engineering

By
Minh Tien Tran

**Title: Crystal Plasticity Finite Element Analysis of Formability and
Deformation Behavior in Ultra-thin Steel Sheet
for Fuel Cell Bipolar Plate**

August 2022

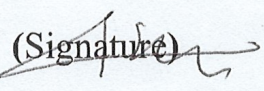
Committee Chair

Professor Kyoungsik Chang

(Signature) 

Committee

Professor Doo-Man Chun

(Signature) 

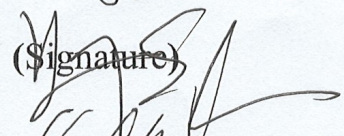
Committee

Professor Dong-Kyu Kim

(Signature) 

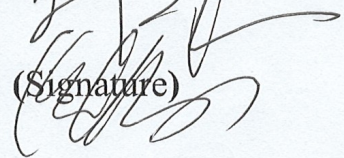
Committee

Professor Sung-Tae Hong

(Signature) 

Committee

Professor Koo-Hyun Chung

(Signature) 

Graduate School

University of Ulsan, South Korea

ABSTRACT

Crystal Plasticity Finite Element Analysis of Formability and Deformation Behavior
in Ultra-thin Steel Sheet for Fuel Cell Bipolar Plate

Minh Tien Tran

School of Mechanical Engineering

Graduate School

University of Ulsan

(Supervised by Professor Doo-Man Chun and Professor Dong-Kyu Kim)

This dissertation is devoted to demonstrating the virtual material testing via microstructure-based simulation using crystal plasticity finite element method (CPFEM) as a robust and potential modelling tool and its application for the prediction of macroscopic mechanical behavior of automotive sheet metals. The focuses are on the investigations on the forming limit diagram (FLD), size effect on the formability and deformation behavior of the ultra-thin ferritic stainless steel (FSS) sheet, and then the process design of multi-stage forming for bipolar plate (BPP) in proton exchange membrane (PEM) fuel cell is proposed. These objectives are comprehensively addressed and summarized as follows.

Firstly, the CPFEM model was successfully developed by accurately reproducing mechanical behavior and yield loci of the material. Then, the CPFEM model was combined with Marciniak–Kuczynski approach in the analysis of forming limits. It revealed that the CPFEM–MK simulations using voxel-typed representative volume element (RVE) with the consideration of measured texture well matched with the experimental FLD.

Secondly, a hybrid cellular automata–Monte Carlo (CA–MC) model was developed to generate a ‘realistic’ RVE that accurately reconstructed the measured texture and grain boundary misorientation distribution (GBMD). The predicted FLD by the CPFEM–MK model with the realistic RVE shows a good agreement with the experimental results. In order to explore the size effect on the formability, the forming limit analyses were conducted using RVEs with various thickness-to-grain size ratios ($t/d = 2\sim 10$). The results revealed a significant degradation of the formability of the ultra-thin FSS sheet as t/d decreased. With decreasing number of grains through the thickness, the stress and strain heterogeneities in the surface grains were noticeably increased due to the less constraint by the subsurface grains, which played an important role in the size effect. Furthermore, it was found that the surface strain hot spots in the material with low t/d could act as the geometrical imperfection to accelerate the failure, together with the increased stress triaxiality in the surface grains as the results of the localized strains and premature necking during the deformation. This attributed the decrease of forming limit strains to the early plastic flow instability in the ultra-thin sheet material with low thickness-to-grain size ratio.

Thirdly, the effect of free surface roughening on the formability of ultra-thin FSS sheet were addressed by in-situ electron backscatter diffraction (EBSD) and CPFEM simulation. The microstructural evolution during uniaxial tension was monitored by the in-situ EBSD technique.

It revealed that as the strain increased, the microstructure of ultra-thin FSS sheet exhibited more significant heterogeneities in terms of surface morphology, kernel average misorientation (KAM) and geometrically necessary dislocation (GND) density distributions. The initial microstructure was then directly mapped onto the finite element mesh in the CPFEM simulation. The results showed that CPFEM predictions of stress and strain heterogeneities and the local hot spots of the ductile fracture initiation well matched with the experimental results. It was found that the localized deformation primarily distributed in the free surface grains which were less constrained and deformed easily, leading to the increased stress and strain heterogeneities. Furthermore, the free surface exhibited a considerable roughness due to the heterogeneous plastic deformation of grains under the applied strains, resulting in the increased thickness inhomogeneity which facilitated the strain localization, consequently the premature necking and fracture in the ultra-thin FSS sheet. This finding strongly supported to the previous elucidation that the early plastic flow instability induced from the localized deformation at subsurface grain was responsible for the decrease of forming limit strains.

Finally, based on these above findings, a special remedy of new multi-stage die design approach was proposed in order to prevent the local thinning and fracture in the ultra-thin FSS sheet for fuel cell BPP. The process design parameters of the proposed die shape were successfully optimized by the developed artificial neural network (ANN) model integrated with the genetic algorithm (GA). The micro-channel analysis by 2D finite element (FE) simulation of two-step forming process revealed a significantly decrease in the local thinning due to the decreased stress/strain heterogeneity. It also showed the more uniform distribution of thickness reduction in addition to the improved minimum thickness and thickness deviation in the micro-channel BPP. Furthermore, the 3D FE simulation of macro-scale BPP channel disclosed the noticeable reduction in the

springback and distortions in terms of twist angle (~18%) and local curvature (~30%). This demonstrated the promising two-step multi-stage forming with a novel die design approach to significantly enhance the formability of ultra-thin metallic BPP by reducing the ruptures and shape error due to the excessively localized thinning and springback, respectively. In addition, this research suggested the beneficial method in the fabrication technologies of ultra-thin metallic BPP for PEM fuel cell.

DEDICATION

This dissertation is devoted to my beloved parents and family whose continuous love and support encouraged me to overcome all the difficulties I have met and to achieve my goals in the past, present and future.

ACKNOWLEDGEMENTS

My deepest gratitude is devoted to my supervisors, Professor Doo-Man Chun and Professor Dong-Kyu Kim, for their continuous instruction, guidance, advice, inspiration, encouragement and support in all aspects during my Ph.D program.

I would like to express my sincere thanks to Professor Kyoungsik Chan, Professor Sung Tae Hong, Professor Koo-Hyun Chung, for being my committee members and valuable suggestions, and to all administrative people from the school and the university.

My sincere appreciation goes to my collaborators, Dr. Ho Won Lee, Dr. Sun-Kwang Hwang, Professor Huai Wang and others for their support and valuable comments on my studies.

I am grateful to the funding supports and scholarships from the Korean government, University of Ulsan and industrial collaborators.

Many thanks to my colleagues in Computational Advanced Materials Processing Lab, Mr. Zhengtong Shan, Mr. Dae-Ho Lee, Mr. Tri Hoang Nguyen, Mr. Minh Sang Pham among others, for their assistance.

I would like to express my special thanks to my family for their support and encouragement. I also thank many other Korean and Vietnamese friends who helped me a lot during my stay in South Korea!

TABLE OF CONTENTS

ABSTRACT	i
DEDICATION	v
ACKNOWLEDGEMENTS	vi
TABLE OF CONTENTS	vii
LIST OF FIGURES	xi
LIST OF TABLES	xix
CHAPTER 1 INTRODUCTION	1
1.1. Introduction	2
1.1.1 Bipolar plate for PEM fuel cell.....	2
1.1.2. Forming limit diagram.....	6
1.1.3. Crystal plasticity model	7
1.2. Literature review	9
1.2.1. Formability of metallic bipolar plate.....	9
1.2.2. Forming limit diagram prediction.....	11
1.2.3. Effect of grain size on the formability and deformation behavior	13
1.2.3. In-situ tensile deformation behavior.....	15
1.3. Research motivation and objectives.....	18
1.4. Structure of this research.....	20
CHAPTER 2 VIRTUAL MATERIAL TESTING BY CRYSTAL PLASTICITY FINITE ELEMENT METHOD	22
2.1. Crystal plasticity finite element method.....	23
2.1.1. Crystal plasticity theory	23

2.1.2. Rate-dependent crystal plasticity constitutive model	25
2.1.3. Virtual microstructure model.....	30
2.2. Experimental procedure	32
2.1.1. Materials	32
2.1.2. Uniaxial tensile test	33
2.1.3. Microstructure measurement	35
2.3. Results and discussion.....	36
2.3.1. Mechanical properties.....	36
2.3.2. Crystallographic texture	37
2.3.3. Constitutive parameter identification	38
2.3.4. Prediction of yield loci	40
2.4. Conclusions	44
Appendix of Chapter 2	46
A1. Flowchart of UMAT calculation procedure	46
A2. Hill’s 1948 quadratic yield function.....	47
A3. Yld2000-2d non-quadratic anisotropic yield function	48
CHAPTER 3 FORMING LIMIT DIAGRAM OF ULTRA-THIN STEEL SHEET.....	51
3.1. Experimental procedure	52
3.1.1. Specimen preparation	52
3.1.2. Formability test.....	53
3.2. Theoretical approach.....	54
3.2.1. Combined CPFEM and MK model	54
3.2.2. Necking instability criterion (NIC) model.....	58
3.3. Results and discussion.....	60
3.3.1 Experimental FLD	60

3.3.2 Effect of imperfection factor and initial texture on the FLD prediction	63
3.3.3 Role of geometrical imperfection in the FLD prediction	66
3.4. Conclusions	68
CHAPTER 4 SIZE EFFECT ON FORMABILITY OF ULTRA-THIN STEEL SHEET...	69
4.1. Methodology	70
4.1.1. Experiment.....	70
4.1.2. CPFEM simulation	70
4.1.3. A hybrid cellular automata and Monte Carlo model	70
4.2. Results and discussion.....	73
4.2.1. Generation of the realistic RVEs.....	73
4.2.2. Size effect on the formability	79
4.3. Conclusions	90
CHAPTER 5 FREE SURFACE ROUGHENING EFFECT ON THE FORMABILITY OF ULTRA-THIN STEEL SHEET.....	93
5.1. Methodology	94
5.1.1. In-situ tensile test with a miniaturized specimen.....	94
5.1.2. Microstructural characterization.....	96
5.1.3. Micromechanical simulation	97
5.3. Results and discussion.....	98
5.3.1. In-situ EBSD microstructure	98
5.3.2. CPFEM simulation of micromechanical deformation.....	102
5.3.3. Free surface effect on the failure behavior	106
5.4. Conclusions	113
CHAPTER 6 DESIGN OF MULTI-STAGE FORMING PROCESS OF ULTRA-THIN BIPOLAR PLATE FOR FORMABILITY IMPROVEMENT	115

6.1. Multi-stage forming process.....	116
6.2. Process design of multi-stage forming.....	117
6.2.1. Propose of pe-forming die design.....	117
6.2.2. Micro-channel BPP simulation.....	119
6.2.3. Optimization of process design parameters with ANN	121
6.2.4. Macro-scale BPP simulation	126
6.3. Results and discussion.....	127
6.3.1. ANN-GA optimization	127
6.3.2. Evaluation of formability in the micro-channel BPP	129
6.3.2. Evaluation of formability in the macro-scale BPP	136
6.4. Conclusions	142
CHAPTER 7 SUMMARY AND CONCLUSIONS.....	144
REFERENCES.....	149
PUBLICATIONS	169

LIST OF FIGURES

Fig. 1.1 (a) Forming limit diagram and (b) definition of major and minor strains.

Fig. 1.2 Illustration of punch geometries and apparatus used in the Nakazima and Marciniak experiments to measure the FLD [26].

Fig. 1.3 Representative schematic of CPFEM simulations considering (a) one deformation mechanism (lattice dislocation) and one phase, (b) multiple deformation mechanisms (dislocations, twinning), multiple orientations, phases and homogenization schemes [47].

Fig. 1.4 Virtual material testing by CPFEM and its application to the prediction of yield locus for the automotive sheet component [47,48].

Fig. 2.1 Schematical representation of aggregate (polycrystal), single crystal and slip systems in FCC and BCC crystals.

Fig. 2.2 Illustration of resolved shear stress acting on the slip system.

Fig. 2.3 Shear stress-strain curve in single crystal.

Fig. 2.4 Schematic of deformation gradient decomposed into its elastic and plastic parts.

Fig. 2.5 Mesoscopic representative volume elements (RVEs): (a) voxel, (b) realistic and (c) microstructure mapping.

Fig. 2.6 Mesoscopic voxel-typed RVEs (Euler angles φ_1 , ϕ and φ_2 indicated by color).

Fig. 2.7 Schematic of uniaxial tensile specimen of ultra-thin FSS sheet.

Fig. 2.8 Illustrations of (a) UTM uniaxial tension instrument, (b) digital image correlation (DIC) monitor and (c) ARAMIS 3D 5M system.

Fig. 2.9 (a) True stress-strain and (b) r-value curves of ultra-thin FSS sheet obtained from digital image correlation (DIC) analysis.

Fig. 2.10 (a) Reconstruction of three-dimensional view of IPF map, (b) ND IPF map and (c) grain size distribution of ultra-thin FSS sheet.

Fig. 2.11 (a) The ODF sections of measured textures of ultra-thin FSS sheet and (b) typical fiber texture for the position of important BCC orientations at $\varphi_2 = 45^\circ$.

Fig. 2.12 Comparison of experimentally measured and CPFEM predicted stress-strain curves of ultra-thin FSS sheet in the (a) rolling direction (RD), (b) diagonal direction (DD) and (c) transverse direction (TD).

Fig. 2.13 Yield loci predictions of ultra-thin FSS sheet compared with the experimental results.

Fig. 2.14 Effect of crystallographic texture on the yield loci predictions of ultra-thin FSS sheet.

Fig. 3.1 Illustration of initial geometry of the ultra-thin FSS sheet specimens for the FLD test.

Fig. 3.2 Illustration of (a) Erichsen universal sheet testing machine, digital image correlation (DIC) camera and (b) hemisphere punch used in the FLD test.

Fig. 3.3 Illustration of digital image correlation (DIC) analysis for measuring the strain history of FLD specimens during the loading process.

Fig. 3.4 Schematic of combined CPFEM–MK model for FLD prediction of ultra-thin FSS sheet.

Fig. 3.5 Illustration of (a) voxel-typed RVE and (b) FE mesh with definition of nodes at vertices.

Fig. 3.6 Flowchart of combined CPFEM–MK model for FLD prediction of ultra-thin FSS sheet.

Fig. 3.7 Fractured specimens of ultra-thin FSS sheet from the formability test for the (a) first and (b) second Nakazima experiments.

Fig. 3.8 Digital image correlation (DIC) analysis of the specimens with the blank widths of 20~80 during the first and second Nakazima experiments.

Fig. 3.9 Digital image correlation (DIC) analysis of the specimens with the blank widths of 100~200 mm during the first and second Nakazima experiments.

Fig. 3.10 Experimental FLD of ultra-thin FSS sheet by the Nakazima test.

Fig. 3.11 FLD prediction of ultra-thin FSS sheet depending on (a) imperfection factor and (b) initial texture in comparison with experimental measurement.

Fig. 3.12 FLD prediction of ultra-thin FSS sheet by different NIC models in comparison with experimental measurement.

Fig. 4.1 (a) Flowchart of cellular automata–Monte Carlo (CA–MC) hybrid algorithm and (b) schematic of realistic RVE generation.

Fig. 4.2 Generation of realistic RVEs with the average grain size of 13 μm to determine the minimum number of elements per grain (E/G) used in the CPFEM analysis.

Fig. 4.3 The CPFEM predicted stress-strain curves (a) with various number of elements per grain (E/G) in comparison with the experimental results and (b) with and without constrained surface in Z (ND) direction using $E/G = 50$.

Fig. 4.4 The realistically generated RVEs for FLD prediction with the same number of elements per grain ($E/G = 50$), number of grains ($N_{\text{grain}} = 1,074\sim 1,097$) and number of elements ($N_{\text{element}} = 53,900\sim 54,760$): (a) $d = 8 \mu\text{m}$, $t/d = 10$; (b) $d = 13 \mu\text{m}$, $t/d = 6$; (c) $d = 20 \mu\text{m}$, $t/d = 4$; (d) $d = 40 \mu\text{m}$, $t/d = 2$. Note that the thickness of 80 μm is the same for all RVEs.

Fig. 4.5 The reconstructions of grain size distribution of the realistic RVEs with different average grain sizes.

Fig. 4.6 The reconstructions of (a) orientation distribution function (ODF) (Δ represents normalized texture different) and (b) grain boundary misorientation distribution (GBMD) of the realistic RVEs with different average grain sizes.

Fig. 4.7 (a) The CPFEM predicted stress-strain curves and (b) the estimated grain boundary density in the four RVE models with different average grain sizes.

Fig. 4.8 FLD prediction using the realistic RVEs with imperfection factor to verify the CPFEM–MK model in comparison with experimental measurement.

Fig. 4.9 Size effect on formability of ultra-thin FSS sheet using the realistic RVEs with various thickness-to-grain-size ratios (t/d).

Fig. 4.10 The CPFEM results of the accumulated slip, effective strain, stress triaxiality and effective stress distributions in the deformed RVEs ($e = 0.26$) with the thickness-to-grain size ratios: (a) $t/d = 10$ ($d = 8 \mu\text{m}$) and (b) $t/d = 2$ ($d = 40 \mu\text{m}$), and (c) histograms of these damaging indicators. Note that the thickness of $80 \mu\text{m}$ is the same for both RVEs.

Fig. 4.11 The CPFEM results of the accumulated slip, effective strain, stress triaxiality and effective stress distributions in the RD plane of the deformed RVEs ($e = 0.26$) with the thickness-to-grain size ratios: (a) $t/d = 10$ ($d = 8 \mu\text{m}$) and (b) $t/d = 2$ ($d = 40 \mu\text{m}$). Note that the black dash lines indicate some but not all shear bands. Note that the thickness of $80 \mu\text{m}$ is the same for both RVEs.

Fig. 4.12 Correlated stress triaxiality with (a) accumulated slip, (b) effective strain and (c) normalized effective stress (σ/σ_Y) in the deformed RVE with coarse grain ($t/d = 2$). Note that the results were obtained at a critical element as indicated by a small yellow rectangular in Fig. 4.11(b).

Fig. 4.13 Correlated stress triaxiality (η) with the accumulated slip (γ represent accumulated shear strain), effective strain and normalized effective stress (σ/σ_Y) in the deformed RVEs ($e = 0.26$) with thickness-to-grain size ratios: (a–c) $t/d = 10$ ($d = 8 \mu\text{m}$) and (d–f) $t/d = 2$ ($d = 40 \mu\text{m}$). Note that the results were obtained along the two representative white dash lines as indicated in Fig. 4.10(b).

Fig. 5.1 Schematic of miniaturize tensile specimen with the notched gauge for in-situ tensile test.

Fig. 5.2 (a) Contour plot of maximum principal strain distribution in the miniaturized tensile specimen and (b) correlation between strains and applied displacement determined from the isotropic elasto-plastic finite element analysis.

Fig. 5.3 Illustrations of (a) JSM-7900F instrument, (b) in-situ EBSD device and (c) enlarged figure of grooved gauge part in the miniaturized tensile specimen.

Fig. 5.4 Stress-strain curve during in-situ tensile test.

Fig. 5.5 (a) RVE model consisting of the buffer and FSS with microstructure mapping and (b) prescribed boundary conditions.

Fig. 5.6 SEM, boundary, IPF, KAM and GND density maps of undeformed and deformed microstructures of in-situ tensile specimen at different engineering strain levels: (a) $e = 0$, (b) $e = 2\%$, (c) $e = 5\%$, (d) $e = 10\%$ and (e) $e = 30\%$.

Fig. 5.7 (a) Evolutions of boundary density with misorientation angle and (b) boundary density for LAGBs and HAGBs with the strains.

Fig. 5.8 (a) The CPFEM results of the accumulated slip, effective strain, effective stress and stress triaxiality distributions in the deformed RVEs ($e = 30\%$) and (b) histograms of these damaging indicators.

Fig. 5.9 The CPFEM results of IPF maps and accumulated slip in the deformed RVEs in comparison with the in-situ EBSD measurements at different engineering strain levels: (a) $e = 2\%$, (b) $e = 5\%$, (c) $e = 10\%$ and (d) $e = 30\%$.

Fig. 5.10 The CPFEM results of surface morphology in the (a) free surface and (b) quarter layer in the deformed RVE ($e = 30\%$).

Fig. 5.11 The CPFEM results of accumulated slip and displacement in ND distributions in the free surface and quarter layer in the deformed RVE ($\epsilon = 30\%$) along the two representative white solid lines as indicated in Fig. 5.9: (a,c) AC and (b,d) BD.

Fig. 5.12 Correlated thickness uniformity parameter and accumulated slip in the free surface and quarter layer in the deformed RVE ($\epsilon = 30\%$) along the two representative white solid lines (AC and BD) as indicated in Fig. 5.9.

Fig. 5.13 Evolutions of mean surface roughness and average thickness uniformity parameter with the strains in the free surface in the deformed RVEs along the two representative white solid lines (AC and BD) as indicated in Fig. 5.9.

Fig. 5.14 (a) Microstructure of RVE in term of the first Euler angle ϕ_1 and (b) deformation behavior of the critical grains with the strains.

Fig. 5.15 The CPFEM results of accumulated slip distribution along the thickness direction.

Fig. 6.1 Schematic of the bipolar plate (a) before and after forming.

Fig. 6.2 Illustration of process design parameter in the conventional die forming process.

Fig. 6.3 Schematic of the microchannel deformation aspect of the (a) conventional and (b) proposed approaches.

Fig. 6.4 Illustration of proposed pre-forming die approach with (a) the process design parameters and (b) its effect on the deformation aspect.

Fig. 6.5 (a) Illustration of cross-sectional and symmetrical plane and 2D finite element mode for (a) first and (b) second stages forming.

Fig. 6.6 Architecture of artificial neural network (ANN) for prediction of minimum thickness and standard deviation of thickness.

Fig. 6.7 Artificial neural network (ANN) integrated with genetic algorithm (GA) for optimization of process design parameters.

Fig. 6.8 3D finite element model for multi-stage forming simulation of macro-scale BPP channel.

Fig. 6.9 Finite element meshes of die and punch tools and BPP sheet for the multi-stage forming simulation.

Fig. 6.10 ANN model prediction with coefficient of determinations for (a) training, (b) validation, (c) all, and (d) compared results between the target and predicted minimum thickness.

Fig. 6.11 ANN model prediction with coefficient of determinations for (a) training, (b) validation, (c) all, and (d) compared results between the target and predicted thickness standard deviation.

Fig. 6.12 (a) Final formed shape of BPP channel without clamping and corresponding (b) von Mises effective stress and (c) effective plastic strain distributions in the single BPP channel, and (d) histogram of maximum value of these variables compared between the conventional and proposed die design approaches.

Fig. 6.13 (a) Final formed shape of BPP channel with clamping and corresponding (b) von Mises effective stress and (c) effective plastic strain distributions in the single BPP channel, and (d) histogram of maximum value of these variables compared between the conventional and proposed die design approaches.

Fig. 6.14 (a) 2D finite element results of thickness distributions in the micro-channel BPP without clamping and (b) histogram of minimum thickness and standard deviation of thickness compared between the conventional and proposed die design approaches.

Fig. 6.15 (a) 2D finite element results of thickness distributions in the micro-channel BPP with clamping and (b) histogram of minimum thickness and standard deviation of thickness compared between the conventional and proposed die design approaches.

Fig. 6.16 3D finite element results of thickness distributions in the macro-scale BPP channel compared between the conventional and proposed die design approaches.

Fig. 6.17 3D finite element results of (a) local minimum thickness distributions in the macro-scale BPP channel and (b) histogram of minimum thickness and standard deviation compared between the conventional and proposed die design approaches.

Fig. 6.18 3D finite element results of (a) contour plot of thickness distribution in the macro-scale BPP channel with the proposed die design approach and histogram of (b) minimum thickness and (c) standard deviation at twelve channel corners as indicated in Fig. 6.18(a).

Fig. 6.19 3D finite element results of displacement in ND for the (a) conventional and (b) proposed die design approaches, and histograms of (c) twist angle and (d) local curvature at the center. Note that the results were measured along two representative lines as indicated in Fig. 6.18(a).

Fig. 6.20 3D finite element results of von Mises effective stress distributions in the macro-scale BPP channel compared between the (a) conventional and (b) proposed die design approaches.

Fig. 6.21 Distribution of maximum effective stress at the twelve channel corners as indicated in Fig. 6.19 (a) compared between the conventional and proposed die design approaches.

LIST OF TABLES

Table 1.1. DOE targets for fuel cell bipolar plate performance [13].

Table 1.2. Advantages and disadvantages of different bipolar plate materials [13].

Table 1.3. Advantages and challenges for manufacturing processes of fuel cell bipolar plate.

Table 2.1. Chemical compositions of the FSS sheet materials developed by POSCO steel company.

Table 2.2 Tensile properties of the ultra-thin FSS sheet.

Table 2.3. Crystal plasticity hardening parameters of ultra-thin ferritic stainless steel.

Table 6.1. Definition of process design parameters of the proposed die approach with their initial values (mm).

Table 6.2. Optimized process design parameters obtained by ANN-GA model (mm).

CHAPTER 1

INTRODUCTION

This chapter presented an introduction to the research background from the industrial and academic points of view. Based on this, the research motivation and objectives of the present dissertation were given. The structure of this dissertation was also described in this chapter.

1.1. Introduction

1.1.1 Bipolar plate for PEM fuel cell

With the growing demand for the development of alternative energy sources in order to replace the internal combustion engine, the proton exchange membrane (PEM) fuel cell has recently received more attention due to its unique advantages such as environment-friendly features, low operation temperature, rapid start up capacity and high energy efficiency [1]. Such advantages in the PEM fuel cell can overcome the recent problems related to climate change, greenhouse gas and energy shortage. Therefore, the PEM fuel cell has been considered as the most promising energy source and energy conversion device for various applications such as automotive, portable and stationary.

The bipolar plates (BPPs), which take 60–80% and 30–45% of the total weight and cost [2], respectively, are key multifunctional components in the PEM fuel cell. The 2020 and 2025 DOE technical targets for the BPP performance are given in Table 1.1.

The BPP has been commonly fabricated by three different materials categorized as graphite [3], composite [4] and metal [5]. The advantages and disadvantages of different BPP materials are given in Table 1.2. For metallic materials, a lot of attempts have been made on the various metals and alloys such as titanium [6], stainless steel [7], aluminum [8], carbon steels [9], aluminum alloys [10], nickel alloys [11] and copper alloys [12] for the fabrication of the BPP.

Table 1.1. DOE targets for fuel cell bipolar plate performance [13].

Functions	Characteristic	Units	2025 DOE target	2020 DOE target
Connect cells electrically one by one;	Electrical conductivity	Scm^{-1}	>100	100
conduct electrical current	Areal specific resistance	Ωcm^2	<0.01	0.01
Separate the reaction gases	H_2 permeability	$\text{cm}^3\text{sec}^{-1}\text{cm}^{-2}$	2×10^{-6}	1.3×10^{-14}
Facilitate heat management	Thermal conductivity	$\text{Wm}^{-1}\text{K}^{-1}$	/	10
Durability	Corrosion, anode	μAcm^{-2}	<1 and no active peak	1 and no active peak
	Corrosion, cathode	μAcm^{-2}	<1	1
	Lifespan	hours	8000	5000
Light weight	Plate weight	kg/kW	0.18	0.4
Economy	Cost	$\text{\$/kW}^{-1}$	2	3
Good mechanical properties	Flexural strength	MPa	>40	25

Among these materials, the ferritic stainless steel (FSS) BPPs have attracted the attention of many researchers owing to their excellent mechanical properties, superior formability, good electrical conductivity, high corrosion resistance and low cost [13]. In consideration of reducing cost, space and weight, the FSS sheet is the most promising candidate in automotive application for manufacturing of fine width micro-channel BPPs as thin as 0.1 mm or even thinner in mass production with the good mechanical properties and formability.

Table 1.2. Advantages and disadvantages of different bipolar plate materials [13].

Material	Advantages	Disadvantages
Graphite	Excellent corrosion resistance, high thermal and electrical conductivity, stable chemical properties, mature manufacture technology	Poor mechanical properties (brittleness), high weight and volume, poor machinability, high processing cost
Composite	Corrosion resistance, small volume, lightweight, high strength	Poor mechanical strength, low electrical conductivity, difficult for mass production, high price
Metal	High thermal and electrical conductivity, superior mechanical properties, ease of fabrication, low cost, excellent structural durability against shock and vibration, can form ultra-thin BPP	Prone to corrosion (membrane and catalysts poisoning, passive film formation)

Table 1.3 summarizes the advantages and challenges of plastic forming processes for fuel cell BPPs. Generally, hydroforming [14,15], rubber pad forming [16,17] and stamping [18–20] processes are widely used in the fabrication of ultra-thin metallic BPPs.

Table 1.3. Advantages and challenges for manufacturing processes of fuel cell bipolar plate.

Process	Advantages	Challenges
Stamping	<ul style="list-style-type: none"> • Good mechanical properties • Relatively lower cost • High production rate • Long life molds of stamping 	<ul style="list-style-type: none"> • Flow channel geometries • Quality problems: excessive thinning, wrinkles, microcracks, springback
Hydroforming	<ul style="list-style-type: none"> • Reducing time and cost for die manufacturing • Better surface quality, less springback • Capability of forming complicated parts 	<ul style="list-style-type: none"> • Flow channel geometries • Lower production rate • Dimensional accuracy • Expensive equipment
Rubber pad forming	<ul style="list-style-type: none"> • Higher surface quality • Reducing time and cost for die manufacturing 	<ul style="list-style-type: none"> • Flow channel geometries • Rubber pad hardness and thickness • Longer production cycle time
Direct roll forming	<ul style="list-style-type: none"> • Fine parallel flow channel • Higher efficiency and lower cost 	<ul style="list-style-type: none"> • Springback • Serpentine flow fields or complex flow channel geometries
Hot stamping	<ul style="list-style-type: none"> • Fine flow channel • Higher dimensional accuracy • Smaller springback 	<ul style="list-style-type: none"> • Longer production time

1.1.2. Forming limit diagram

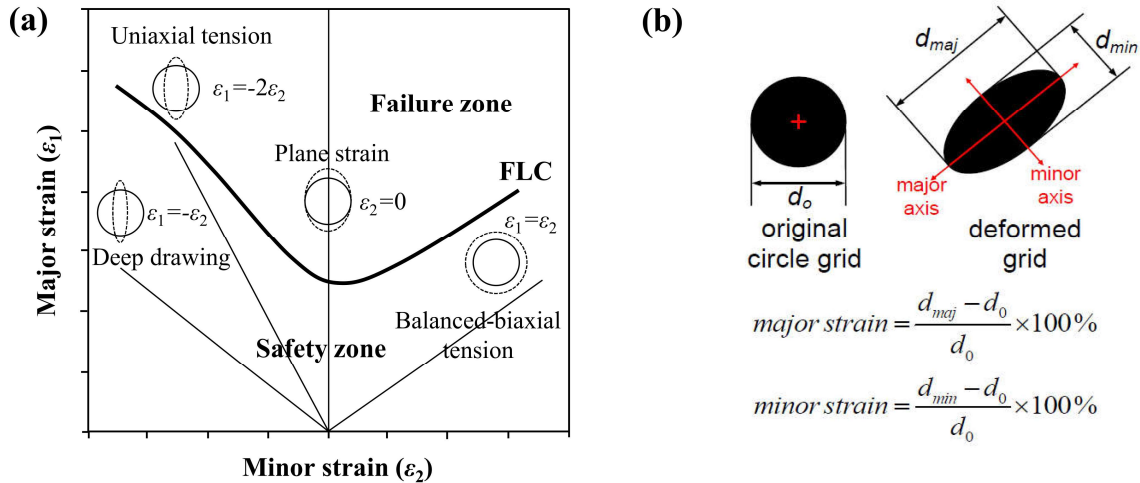


Fig. 1.1 (a) Forming limit diagram and (b) definition of major and minor strains.

The forming limit diagram (FLD) introduced by Keeler [21] and Goodwin [22] has been extensively used in the analysis of sheet metal forming in order to evaluate the formability [23–25]. As shown in Fig. 1.1(a), the FLD is commonly designated by the forming limit curve (FLC) to separate two regions. The region above the FLC corresponds the failure strain states, in contrast, the safe strain states are represented by the region below the FLC. The FLC is generally constructed by mapping the major and minor strains under the different loading paths. Fig. 1.1(b) illustrates the major and minor strains which can be measured using the sheet with a grid. The major and minor strains are defined as the strains in the major and minor loading directions, respectively.

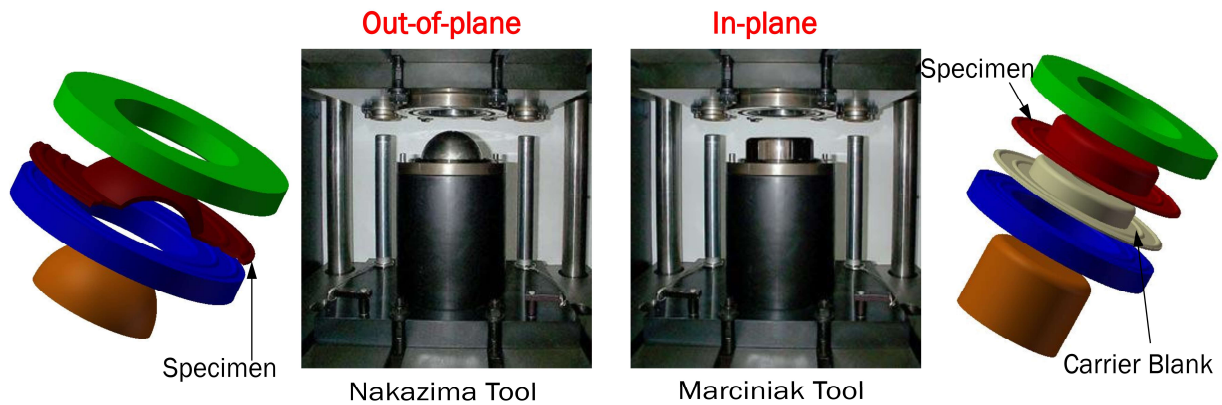


Fig. 1.2 Illustration of punch geometries and apparatus used in the Nakazima and Marciniak experiments to measure the FLD [26].

The FLD of sheet metals is commonly determined by the Nakazima [27] and Marciniak [28] tests following the ISO12004-2:2008 [29]. In the Nakazima test, the hemispherical dome punch is used to deform a sheet for the out-of-plane measurement, meanwhile the in-plane measurement is represented by the Marciniak test using the flat-bottom cylindrical punch as an alternative approach, as shown in Fig. 1.2. Extensive studies have successfully performed the Nakazima and Marciniak tests to determine the FLD of sheet metals [30–32].

1.1.3. Crystal plasticity model

Crystal plasticity has been proven to be the most potential approach as a virtual tool for exploring microstructural evolution during the deformation [33–39]. Moreover, researchers have made substantially advanced development to incorporate crystal plasticity with continuum damage mechanics model [40–42], phase field model [43,44] and thermomechanical framework [45,46] for taking into account more complex physical system in the microstructural analysis of the materials. The use of crystal plasticity models for capturing the microscopic and macroscopic

properties of polycrystalline materials has rapidly increased due to its unique advances in the computational power and wide range of applications.

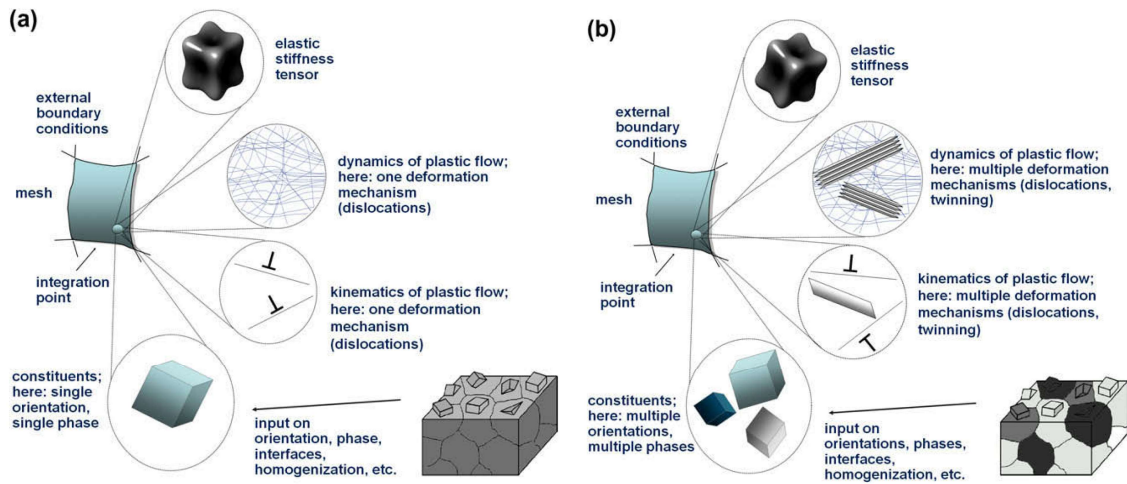


Fig. 1.3 Representative schematic of CPFEM simulations considering (a) one deformation mechanism (lattice dislocation) and one phase, (b) multiple deformation mechanisms (dislocations, twinning), multiple orientations, phases and homogenization schemes [47].

Crystal plasticity finite element method (CPFEM) is an approach with significant advantage explicitly taking into account the mechanical interactions among the crystals in a polycrystal under the complex external and internal boundary conditions [47]. It allows to simulate the different deformation mechanisms as dislocation slip, twinning, martensite, grain boundary shear, grain interactions (Fig. 1.3). Its greatest potential lies in the microscopic and macroscopic applications for the predictions of grain size effect, lattice defects (dislocations, twins, martensite), texture evolution, mechanical behavior, forming limits, material failure. For example, the macroscopic application of CPFEM for the concept of virtual material testing using representative volume element (RVE) was reported in the previous study [48]. Kraska et al. [48] demonstrated the CPFEM as a virtual tool to reproduce the actual shape of the yield locus and corresponding

Lankford parameters. By using this information, the parameters in the empirical constitutive model were calibrated. The study was applied to the commercial stamping part used, for example, in the automotive industry (Fig. 1.4). It has been demonstrated the CPFEM is a robust modelling tool to address the mechanical problems in the field of materials science and engineering. The more details in the CPFEM regarding kinematics and constitutive laws will be presented in Chapter 2.

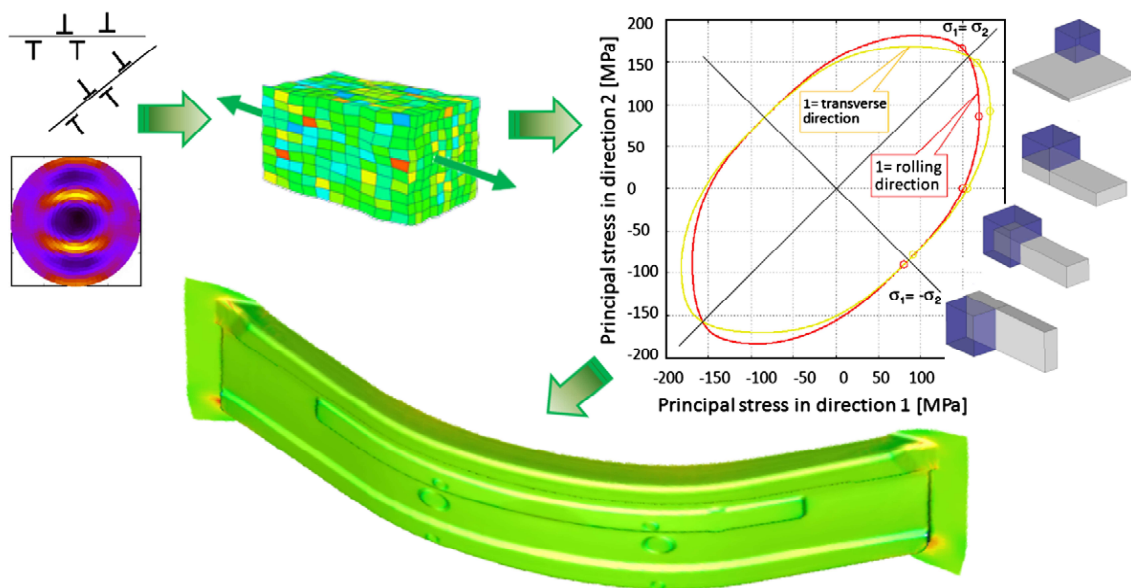


Fig. 1.4 Virtual material testing by CPFEM and its application to the prediction of yield locus for the automotive sheet component [47,48].

1.2. Literature review

1.2.1. Formability of metallic bipolar plate

Zhang et al. [49] investigated the formability of pure copper bipolar plate by using rigid die and flexible die forming processes. The results showed that the greater depth and more uniform wall thickness distribution were found in the micro channel of bipolar plate by using the flexible die forming process. Although the formability of metallic bipolar plate was improved, both rigid and flexible die forming processes still showed local thinning or even fracture in the fillets of micro

channel. In the rigid die forming process, the thinning and fracture was attributed to the stress concentration and large tensile stresses in the internal fillet of the sheet. While the larger degree of bending deformation resulted in the thinning or fracture in the outer fillet of the channel in the flexible die forming process.

Wang et al. [50] studied the formability of bipolar plates during flexible micro forming of Cu/Ni clad foils. They found that the formability of the micro channel was noticeably affected by the feature size, surface roughness and grain size. It revealed that the increased surface roughness and decreased micro channel width resulted in the decreased forming depth and increased local thinning. The results showed that the local thinning at the inner filler of micro channel due to the coarse grain of copper layer. Because the surface roughness was dependent on the plastic deformation and grain size, when the material exhibited the coarse grain, the surface roughness became significantly, consequently the reduction of formability.

Xu et al. [51] employed the single- and multi- stages forming processes to investigate the formability of titanium bipolar plate. They reported that the severe thinning and larger thickness reduction of micro channel were found in the single stage forming process. On the contrary, the multi-stage forming process showed an improvement in the local thinning and the reduction in thickness of micro channel. It was found that the higher deformation localization due to the significantly twisted grains in the single-stage formed part was responsible for the severe thinning. Although the elongated grains in the multi-stage formed part showed little distortion, a severe plastic deformation were also observed which could affect the formability of micro channel.

Zhang et al. [52] experimentally and numerically studied the formability of SS 316L bipolar plate by single- and multi- stages forming process. They reported that the simulation of single-

stage forming process showed deviation due to the springback compared to the experimental result. While it was unobservable in the multi-stage forming simulation. It revealed that the concentration of maximum stress around the fillets of micro channel resulted in the severe thickness reduction and the rupture in the single-stage forming. For multi-stage forming, however, it revealed the uniform thickness distribution because the maximum stress was found in on the rib of micro channel.

1.2.2. Forming limit diagram prediction

Yang et al. [53] investigated the forming limit diagram of face-centered cubic (FCC) sheet under non-proportional strain-path by coupling CPFEM with MK model. They reported that the predicted FLD was significantly influenced by uniaxial pre-tension and plane equibiaxial pre-tension while it was less affected by plane strain pre-tension. It was also found that the texture evolution and slip system hardening induced by pre-strain showed a noticeable effect on the FLD. Kim et al. [54] investigated effect of different slip systems on the FLD of ferritic stainless steel sheet by using the combined CPFEM and MK model. The results showed that the forming limits strains could not be captured when a single slip mode or a combined slip mode with the same hardening parameters was used.

Mohammed et al. [55] studied the forming limit diagram for multiphase advanced high strength steels (QP980 steel) by the coupled CPFEM–MK model. It revealed that the more realistic prediction of the localized necking phenomenon was obtained with the presence of microstructural inhomogeneity. Subsequently, the limit strains for the T-shaped part stamping process of multiphase advanced high strength steels was successfully predicted. Park et al. [56] employed the

combined CPFEM–MK modeling in consideration of martensitic phase transformation to predict the forming limit diagram for the multiphase 3rd generation advanced high strength steels (QP980 and QP1500 steels). The results showed that the improvement of forming limit strains for all strain paths was obtained by at least 10% for the QP980 steel. While it was decreased for all deformation paths by at least 10% for the QP1500 steel due to the increase in the untampered martensite phase.

Isavand et al. [57] proposed a microstructure-based micromechanical approach using CPFEM model to predict the forming limits of ferrite-pearlite steels. The predicted FLD was successfully verified in comparison with the Nakazima formability test. It was found that the intense stress/strain partitioning in form of localized deformation bands was observed, together with the high dependency of local deformation pattern on the microstructural morphology and loading direction. Zhang et al. [58] developed the CPFEM model with a micro-mechanics based transformation criteria in combination with the MK approach to predict the forming limit diagram for the duplex stainless steel consisting of 65% ferrite and 35% retained austenite by volume. They found that the formability of duplex stainless steel by considering martensite phase transformation was enhanced by at least 20% compared to without transformation. It was reported that the localization at critical moments during the deformation was suppressed by the transformation-induced plasticity effect.

Bong et al. [30,35,59] experimentally and numerically investigated the forming limit diagrams for magnesium alloys and ferritic stainless steel sheets. Recently, Bong and Lee [59] addressed the effect of surface roughness on the forming limit diagram of 0.1 and 1 mm thick ultra-thin ferritic stainless steel (FSS) sheets based on the CPFEM in conjunction with the MK model. It revealed that the CPFEM–MK model by considering surface roughening effect well reproduced the

experimental FLD of two FSS sheets. The results pointed out the importance of surface roughening in thinner FSS sheet where the surface roughness in micron scale was an order higher than that in the thicker sheet.

1.2.3. Effect of grain size on the formability and deformation behavior

The effect of grain size on the mechanical behavior of the materials have been extensively investigated. Chan et al. [60] explicitly simulated individual grains with different stress-strain behaviors to investigate the grain size effect on micro deformation behavior in micro-forming of pure copper. It was found that as the grain size increased, the flow stress of the pure copper material decreased due to the weakening of grain boundary strengthening effect. They also reported that the heterogeneity of deformation was attributed to the nonuniform distribution of the grains with different sizes, shapes and orientations when the specimen consisted of only a few grains through the thickness.

Chen et al. [61] performed the grain level finite element analysis in combination with the CPFEM model to address the effect of grain size and heterogeneity on the mechanical behavior of foil rolling. They showed that the deteriorative effects of grain size and heterogeneity on the mechanical properties of pure copper foils with the CPFEM was well correlated to the reduction of the number of grains through the thickness. It was found that the surface grain effect regarding to grain orientations, slip systems activation and interaction between interior and surface grains resulted in the softening behavior of the materials.

Zhang et al. [62] employed crystal plasticity modeling with high-fidelity representative microstructures to explore the grain-level plastic heterogeneity and fracture mechanism of thin

sheet metals in micro-forming operations. It was found that the specimen with low thickness-to-grain size ratio exhibited a pure shear failure in addition to the primary micro-crack initiation at the free surfaces, which increased the heterogeneous deformation, lattice rotation and activity of slip systems while the stress heterogeneity and work-hardening were decreased. They also reported that the damage initiation originated from the grain-scale undulation and necking was due to the interaction between local shear bands and free surfaces.

Shang et al. [63] proposed the full-field CPFEM simulations to address the grain size effect on micro-void evolution and ductile fracture in an austenite steel 316LN. The results showed that the void growth and heterogeneous deformation increased with the grain size, resulting in the degradation of ductility. They reported that the transition of fracture modes was due to the variation of void growth with the grain size. The fracture initiation was dominated by the coalescence of densely distributed voids in the fine grain specimen. While the fracture occurrence was controlled by the growth and coalescence of individual large void in the coarse grain specimen.

Not only the mechanical behavior, but also the formability of the sheet materials was significantly affected by the grain size, which was comprehensively studied by many researchers. Shakeri et al. [64] presented that as the grain size increased, the formability of low carbon steel ST12 and austenitic stainless steel 331 shifted down due to the higher heterogeneity of the coarse grain in the specimens. Assempour et al. [65] also showed that the forming limit diagram of low carbon steel ST12 decreased with the increasing grain size.

Xu et al. [66] investigated grain size effects on the formability of pure copper sheets in micro-scaled plastic deformation through experiments and modelling. It was found that the forming limit strains of the material decreased with the decrease in the thickness-to-grain size ratio, i.e., the

increasing grain size. The results showed that the different behaviors of individual grains affected the formability when the specimen consisted of only one or two grains through the thickness. They reported that the early strain localization and heterogeneity of deformation were responsible for the decrease in the forming limit strains.

Xu et al. [67] employed an extended GTN (Gurson-Tvergaard-Needleman) and Thomason model in couple with the finite element simulations to investigate the grain size effect on the formability of thin copper sheet materials. The significant grain size effect on the forming limit strains was observed. It revealed that the formability was shifted down due to the early initiation of strain localization affected by the individual grain with the reduction of thickness-to-grain size ratio. In addition, they also addressed the geometry and grain size effects on the void nucleation, growth and coalescence in the ductile fracture process of micro/meso scaled sheet metals based on the macro scaled damage-coupled model.

Weiss et al. [68] investigated experimentally the grain size effect on the forming limit diagram of stainless steel foils. In order to produce different grain sizes, the specimens was subjected to the annealing heat treatment under different conditions. It was also found that the formability of stainless steel foils significantly decreased with the increasing grain size. They reported that the increased inhomogeneous deformation in addition to the softening of the surface grains resulted in the earlier strain localization and necking, consequently the decrease in the forming limit strains.

1.2.3. In-situ tensile deformation behavior

Chen et al. [69] performed in-situ EBSD technique to investigate the active slip systems and lattice rotation behavior of surface grains in a polycrystalline aluminum alloy during uniaxial

tension. The results showed the heterogeneous lattice rotation of individual grains, in terms of rotation path and rotation rate which might change as the plastic deformation proceeded, leading to the formation of subregions. It also revealed the difference in the lattice deformation behavior of surface grains from that of inner grains due to the different activation of slip systems with a fewer independent slip systems in the surface grains than that of the grains in the interior of the material.

Sinha et al. [70] employed the combinations of in-situ EBSD and CPFEM simulations to investigate the evolution of microstructure during the deformation in the 316L austenitic stainless steel. They found that the deformation at the initial stage was caused by the dislocation slip, however, as the strain increased the deformation was dominated by the twinning along with the evolution of intragranular misorientation and concomitant roughness evolution in the deformed state. It was also found that the material failure was attributed to the grains with higher roughness evolution in addition to the saturation in twinning, consequently lower work hardening rate, as addressed by CPFEM simulations.

Wang et al. [71] investigated the twin boundary evolution and crack initiation behavior during uniaxial tension in 316L stainless steel by means of in-situ EBSD technique. The results showed the gradual decrease in the percentage of the twin boundaries with increasing deformation and the initiation of crack at the twin boundaries after a certain deformation. It revealed that the crack initiation was attributed to the continuous increase in the strain concentration and dislocations density.

Yvell et al. [72] studied the in-situ tensile deformation behavior of a high-nickel austenitic stainless steel. The results revealed the increase in the number of low-angle grain boundaries

(LAGBs) and their respective misorientation when the strain increased, together with the evolution of some of them into high-angle grain boundaries (HAGBs). They showed that the increasing spread of orientations and grains moving parallel to the tensile direction characterized the change of individual grains. It was also reported that the dislocation slip was a dominant factor to the deformation due to the absence of deformation twins in the microstructure of the material.

Li et al. [73] employed in-situ EBSD technique to investigate the plastic deformation behavior of DP600 steel during uniaxial tension. They reported that the plastic strain localization was predominantly observed in the ferrite grains where fracture could usually occur. The results revealed the increased fraction of LAGBs and the decreased average misorientation angle as the strain increased. It was also found that the activation of different slip systems resulted in the subdivision of some grains into the different regions which indicated that the plastic deformation could take place in these grains.

Wu et al. [74] investigated the changes in microstructure and texture during uniaxial tension of pure nickel by using in-situ EBSD. The result revealed the easier rotation of crystallographic orientations which were parallel to the tensile direction into a cubic orientation than the other orientations which were not parallel to the tensile direction. It was found that the dislocation movement resulted in the increase of the fraction of LAGBs and the formation of deformation-induced grain boundaries led to the increase of total grain boundaries. They also reported that the grains with hard orientation were less affected by dislocation while it was readily involved in the dislocation movement for the grain with the soft orientation.

1.3. Research motivation and objectives

The use of ultra-thin metallic materials in the sheet forming is still challenged to the formability because the thin sheet forming more often fails after abruptly severe strain localization. Such a failure is due to the commonly occurrence of the ruptures induced by excessively localized thinning during the forming process.

To date, several studies have been carried out to address the formability of thin metallic materials in the sheet forming process [75–78]. Experimental measurement of FLD often requires excessive time and high manufacturing cost, therefore, various theoretical models have been proposed as an alternative to direct experiments [24,79–81]. Among these approaches, a Marciniak-Kuczynski (MK) model [28] has been widely and successfully adopted to estimate the FLD [79,82–85]. The MK model assumes that under various plane stress states, the strain localization in necking band is initiated by a pre-existing imperfection due to a higher thinning rate in the groove region than that in the homogeneous region. In order to further improve the prediction accuracy of the FLD, Wang et al. [79] proposed the modified MK model by introducing the integration of through-thickness normal stress and friction stress. Recently, Banabic et al. [86] reported a historical perspective on the different developments made in the MK model. Indeed, a lot of attempts have been reported to incorporate different advanced constitutive models with the MK approach for reproducing the experimental FLD [87–92].

Phenomenological constitutive models can account for the yield surface shape and its evolution. However, the yield surface shape is predominantly controlled by microstructure of the material, which noticeably evolves during deformation, consequently the forming limit strains can be inaccurately predicted with non-proportional loading. It is noteworthy to mention that the FLD

and mechanical responses of polycrystalline materials are significantly affected by crystallographic texture evolution [93–98]. In addition, extensive mechanical tests are often required to identify constitutive parameters of phenomenological model.

The CPFEM are being widely used for predicting the mechanical responses under various loading conditions, and thereby directly addressing the material anisotropy, crystal orientation and dislocation slips in the forming limit analysis of various sheet metals. Yang et al. [53] presented that the predicted FLD by coupling CPFEM with MK model was significantly influenced by uniaxial pre-tension and plane equibiaxial pre-tension while it was less affected by plane strain pre-tension. Kim et al. [54] investigated effect of different slip systems on the FLD of FSS sheet by using the combined CPFEM and MK model. Mohammed et al. [55] reported that the predicted FLD by CPFEM–MK model was successfully validated by the T-shaped part stamping process of multiphase advanced high strength steels. Recently, Bong and Lee [59] addressed the effect of surface roughness on the formability of ultra-thin FSS sheets based on the CPFEM in conjunction with the MK model. It reveals that the CPFEM–MK model by considering surface roughening effect well reproduced the experimental FLD.

The BPPs for PEM fuel cell are made of ultra-thin metallic materials for the sake of reducing cost and weight. Ultra-thin sheet metals may show a deviation from the conventional mechanical behavior, so-called size effect, once the thickness of the polycrystalline sheet becomes comparable to the grain size. In order to characterize the size effect, the thickness-to-grain size ratio (t/d) has been adopted by many researchers [68,99,100]. It has been reported that when the thickness-to-grain size ratio is less than 10, the size effect will disclose a significant effect on the mechanical responses and formability of thin metallic materials [61,99,101]. As the t/d decreases, i.e., number

of grains through the thickness becomes less, an individual grain will play an important role on overall mechanical behavior of the materials. To the best of the author's knowledge, there has been no report on size effect on the forming limit of ultra-thin FSS sheet for the BPs in PEM fuel cell.

The present dissertation comprehensively investigates the formability, particularly the size effect on the FLD, and deformation behavior and design of multi-stage forming process for the ultra-thin FSS sheet for the BPPs in PEM fuel cell by experimental and numerical modelling approaches. The main framework of this dissertation is:

- Experimental characterization of mechanical properties by uniaxial tensile test and FLD determination by the Nakazima test for the ultra-thin FSS sheet.
- Microstructure observation for the crystallographic texture, grain size of the ultra-thin FSS sheet by electron backscatter diffraction (EBSD) measurements.
- Development of a combined CPFEM–MK model for predicting the mechanical behavior and FLD of the ultra-thin FSS sheet by considering the measured texture.
- Investigation of size effect on the FLD of the ultra-thin FSS sheet by a combined CPFEM–MK model and realistic representative volume elements (RVEs) with various t/d ratios.
- Investigation of free surface roughening effect on the formability of the ultra-thin FSS sheet by in-situ EBSD technique and CPFEM simulation.
- Design of new multi-stage forming process of ultra-thin bipolar plate for formability improvement.

1.4. Structure of this research

The present dissertation is structured into seven chapters. The research background, literature review, motivation and objectives of this dissertation are introduced in Chapter 1. Chapter 2

presents the virtual material testing with the concept of CPFEM and its application for predictions of mechanical response and yield loci of the ultra-thin FSS sheet. The investigation of FLD and size effect on the formability of the ultra-thin FSS sheet are addressed in Chapter 3 and Chapter 4, respectively. The coupled in-situ EBSD and CPFEM for the investigation of free surface roughening on the formability of the ultra-thin FSS sheet is presented in Chapter 5. Chapter 6 presents the design of multi-stage forming process for the formability improvement. Finally, Chapter 7 summarizes and draws the main conclusions of this dissertation.

CHAPTER 2

VIRTUAL MATERIAL TESTING BY

CRYSTAL PLASTICITY FINITE ELEMENT METHOD

This chapter briefly presents the virtual material testing with the concept of crystal plasticity finite element method (CPFEM) and its application for prediction of mechanical behavior and yield loci of the ultra-thin steel sheet for bipolar plate in PEM fuel cell. Uniaxial tensile tests were performed to characterize the macroscopic properties of the material. The crystallographic texture of the FSS sheet was characterized by electron backscatter diffraction (EBSD) measurement. The CPFEM simulations of uniaxial tensile test using representative volume element (RVE) were carried out to identify the hardening parameters by the trial and error method. The predicted stress-strain response was compared with the experimental results. Then, a series of CPFEM simulations were performed to determine the stress states located on the yield loci.

2.1. Crystal plasticity finite element method

2.1.1. Crystal plasticity theory

Crystal plasticity is a novel class of anisotropic elastoviscoplastic behavior of the materials. Depending on the loading direction, crystalline aggregates will behave differently the elastic-plastic deformation. This implies that crystalline aggregates are mechanically anisotropic [47]. In the mesoscale approach with crystal plasticity, grains and slip system are discrete and then the anisotropy of single crystal properties and crystallographic texture are considered in modelling the mechanical behavior of polycrystalline materials (Fig. 2.1).

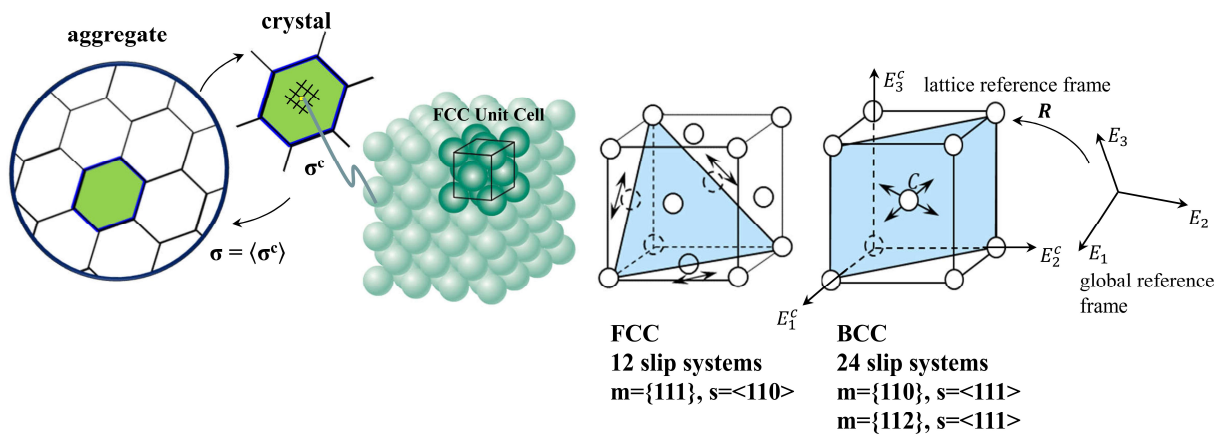


Fig. 2.1 Schematic representation of aggregate (polycrystal), single crystal and slip systems in FCC and BCC crystals.

At the macroscale level, the mechanical behavior, particularly plastic anisotropy, is controlled by the microstructural features which are anisotropy of single crystal properties (crystal structure/slip systems) and crystallographic texture (totality of crystallite orientations). In polycrystal plasticity, constitutive model is incorporated to link these features for modelling the plastic anisotropy of the material. As shown in Fig. 2.1, the single crystal will deform plastically on the deformation mode (slip systems) when the applied stress is enough to activate mode. Then,

the mechanical behavior of the material is calculated by averaging over the aggregate of polycrystals.

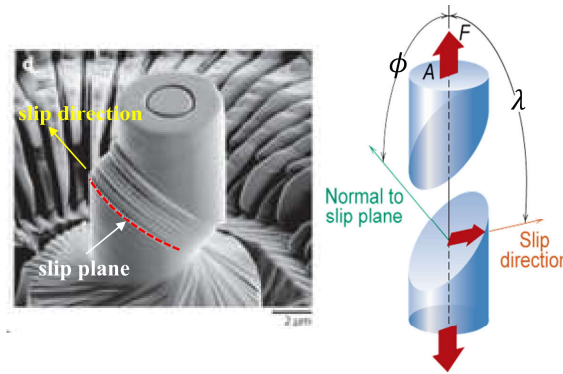


Fig. 2.2 Illustration of resolved shear stress acting on the slip system.

The majority of plastic deformation mechanism in most polycrystalline material is the dislocation slip. Schmid [102] performed uniaxial tension of zinc single crystal and analyzed the yield strength based on the experimental data. According to his conclusion, the resolved shear stress that acted in the slip direction on the slip plane drove the initiation of plastic deformation. As shown in Fig. 2.2, the resolved shear stress can be defined as

$$\tau_{\text{RSS}} = \sigma \cdot \cos\phi \cdot \cos\lambda \quad (2.1)$$

where σ is the uniaxial applied stress, ϕ and λ are the angle between the loading axis and the normal direction of the slip plane and the slip direction, respectively. According to the Schmid's law, a crystal deforms plastically when the resolved shear stress reaches a critical value that is called the critical resolved shear stress (CRSS, τ_c), at which the dislocation or dislocation slip starts movement. Dislocation slip is more likely to move on the slip plane with the most closely packed of the atoms than other crystal planes having a Burger vectors in the direction with the most closely packed of the atoms. For FCC crystal, the dislocation slip is along the $\langle 110 \rangle$ direction on the $\{111\}$

planes, for BCC crystal, the major slip system is along the $\langle 111 \rangle$ direction on $\{110\}$, $\{112\}$ and $\{123\}$ planes.

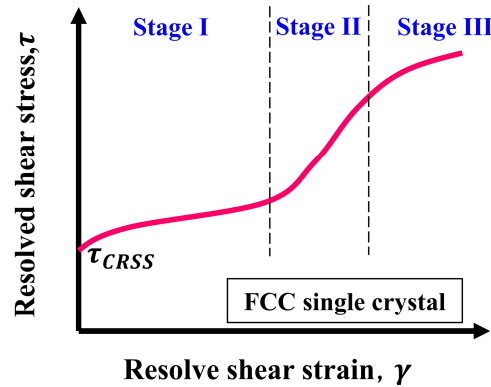


Fig. 2.3 Shear stress-strain curve in single crystal.

During the continuous plastic deformation, the dislocations are accumulated and the frequency of self and latent hardening interactions is increased. This affects the resistances to the movement of dislocations, consequently the strain hardening [103,104]. Fig. 2.3 shows the typical strain hardening behavior in the FCC single crystal followed by a three-stage scheme. Stage I is called ‘easy glide’ with low hardening rates because the dislocation can move without any interaction with each other and only one single slip system is operative. In stage II, there is a linear increase of shear stress with high and constant hardening rate to continue plastic deformation and multiple slip systems are operative. The strain hardening is due to the pile-ups of dislocation at obstacles. In stage III, there is a decrease in the hardening rate due to the escape of dislocations from the obstacles with high shear stress.

2.1.2. Rate-dependent crystal plasticity constitutive model

In the constitutive model of rate-dependent crystal plasticity originally proposed by Rice [105] and Asaro [106], the deformation gradient \mathbf{F} and velocity gradient \mathbf{L} are used to describe the local

deformation behavior of single crystal. As shown in Fig. 2.4, the total deformation gradient \mathbf{F} is multiplicatively decomposed into the elastic and plastic parts as

$$\mathbf{F} = \mathbf{F}^e \mathbf{F}^p \quad (2.2)$$

where \mathbf{F}^e is the elastic deformation gradient associated with elastic distortion and rigid body rotation and \mathbf{F}^p is the plastic deformation gradient associated with dislocation slip on specific slip system.

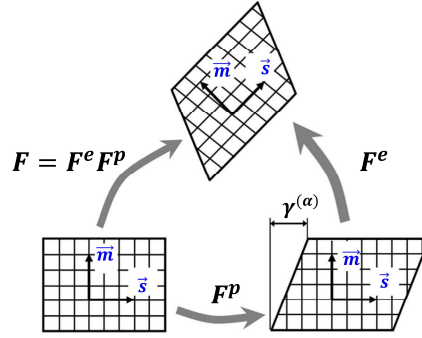


Fig. 2.4 Schematic of deformation gradient decomposed into its elastic and plastic parts.

The velocity gradient is defined as

$$\mathbf{L} = \dot{\mathbf{F}}\mathbf{F}^{-1} = (\dot{\mathbf{F}}_e \mathbf{F}_p + \mathbf{F}_e \dot{\mathbf{F}}_p) \mathbf{F}_e^{-1} \mathbf{F}_p^{-1} = \dot{\mathbf{F}}_e \mathbf{F}_e^{-1} + \mathbf{F}_e (\dot{\mathbf{F}}_p \mathbf{F}_p^{-1}) \mathbf{F}_e^{-1} \quad (2.3)$$

The velocity gradient can be further expressed by using the sum of symmetric deformation rate tensor \mathbf{D} and skew-symmetric spin rate tensor \mathbf{W} as

$$\mathbf{D} = \frac{1}{2}(\mathbf{L} + \mathbf{L}^T) = \mathbf{D}^e + \mathbf{D}^p \quad (2.4)$$

$$\mathbf{W} = \frac{1}{2}(\mathbf{L} - \mathbf{L}^T) = \mathbf{W}^e + \mathbf{W}^p \quad (2.5)$$

where the lattice spin rate is defined by the rigid body rotation of the lattice \mathbf{R}^e as

$$\mathbf{W}^e = \dot{\mathbf{R}}^e (\mathbf{R}^e)^T \quad (2.6)$$

The rate of plastic deformation gradient is represented by

$$\dot{\mathbf{F}}^p = \mathbf{L}^p \mathbf{F}^p \quad (2.7)$$

where \mathbf{L}^p is the plastic velocity gradient associated with dislocation motion and is expressed by the sum of crystallographic slip deformations of all slip systems as

$$\mathbf{L}^p = \sum_{\alpha=1}^N \dot{\gamma}^{(\alpha)} \mathbf{s}^{(\alpha)} \otimes \mathbf{m}^{(\alpha)} \quad (2.8)$$

where N is the total number of slip systems and $\dot{\gamma}^{(\alpha)}$ is the slip shear strain rate in the slip system α . $\mathbf{s}^{(\alpha)}$ and $\mathbf{m}^{(\alpha)}$ are the slip direction and slip plane normal to the slip system α in the undeformed configuration, respectively.

The plastic velocity gradient can be further written as the rate of deformation tensor \mathbf{D}^p and spin tensor \mathbf{W}^p for plastic deformation as

$$\mathbf{L}^p = \mathbf{D}^p + \mathbf{W}^p \quad (2.9)$$

where

$$\mathbf{D}^p = \sum_{\alpha} \dot{\gamma}^{(\alpha)} \mathbf{P}^{(\alpha)} \quad (2.10)$$

$$\mathbf{W}^p = \sum_{\alpha} \dot{\gamma}^{(\alpha)} \mathbf{W}^{(\alpha)} \quad (2.11)$$

where \mathbf{P}^{α} and spin tensor \mathbf{W}^{α} are defined respectively by

$$\mathbf{P}^{(\alpha)} = \frac{1}{2} (\mathbf{s}^{(\alpha)} \otimes \mathbf{m}^{(\alpha)} + \mathbf{m}^{(\alpha)} \otimes \mathbf{s}^{(\alpha)}) \quad (2.12)$$

$$\mathbf{W}^{(\alpha)} = \frac{1}{2} (\mathbf{s}^{(\alpha)} \otimes \mathbf{m}^{(\alpha)} - \mathbf{m}^{(\alpha)} \otimes \mathbf{s}^{(\alpha)}) \quad (2.13)$$

The shear strain rate $\dot{\gamma}^{(\alpha)}$ on the slip system α is dependent on the resolved shear stress and the resistance to shearing by using the power law [107] to describe the shearing kinetics on the active slip systems as

$$\dot{\gamma}^{(\alpha)} = \dot{\gamma}_0 \text{sign}(\tau^{(\alpha)}) \left(\frac{\tau^{(\alpha)}}{\tau_c^{(\alpha)}} \right)^{\frac{1}{m}} \quad (2.14)$$

where $\dot{\gamma}_0$ is the reference shear strain rate, $\tau^{(\alpha)}$ is the resolved shear stress, $\tau_c^{(\alpha)}$ is the critical resolved shear stress (CRSS), and m is the strain rate sensitivity. The resolved shear stress is given in the form of Schmid law as

$$\tau^{(\alpha)} = \mathbf{T} : \mathbf{S}^{(\alpha)} = \mathbf{T} : (\mathbf{s}^{(\alpha)} \otimes \mathbf{m}^{(\alpha)}) \quad (2.15)$$

The constitutive equation of single crystal is given as

$$\mathbf{T} = \mathbf{C}^e : \mathbf{E} = \det(\mathbf{F}^e) \mathbf{F}^{e^{-1}} \boldsymbol{\sigma} \mathbf{F}^{e^{-T}} \quad (2.16)$$

where \mathbf{T} is the second-order Piola-Kirchhoff stress tensor, $\boldsymbol{\sigma}$ is the Cauchy stress tensor, \mathbf{C}^e is a fourth-order anisotropic elasticity tensor, \mathbf{E} is the elastic Lagrangian strain tensor as expressed

$$\mathbf{E} = \frac{1}{2} (\mathbf{F}^{eT} \mathbf{F}^e - \mathbf{I}) \quad (2.17)$$

The critical resolved shear stress evolves with plastic strain on all slip systems as follows

$$\tau_c^{(\alpha)} = \sum_{\beta=1}^N \mathbf{h}_{\alpha\beta} |\dot{\gamma}^{(\beta)}| \quad (2.18)$$

where $\mathbf{h}_{\alpha\beta}$ is the hardening matrix which is introduced to take into account the interaction among the slip systems including the self-hardening ($\alpha = \beta$) and latent-hardening ($\alpha \neq \beta$). The $\mathbf{h}_{\alpha\beta}$ is expressed as

$$\mathbf{h}_{\alpha\beta} = qh + (1 - q)h\delta_{\alpha\beta} \quad (2.19)$$

where h is the hardening modulus, $\delta_{\alpha\beta}$ is the Kronecker delta, and q is the latent hardening rate due to the slip activity on other slip systems. The hardening law for a slip system is defined as [108]

$$h = h_0 \left(1 - \frac{\tau_c^{(\alpha)}}{\tau_s}\right)^a \quad (2.20)$$

where h_0 is the initial hardening rate, τ_s is the saturation value of the slip resistance, and a is the hardening exponent.

During the deformation, the macroscopic loading is applied to the material co-rotational coordinate system while the deformation takes place in the crystal coordinate system. A crystal orientation matrix, \mathbf{Q} , is used to define the orientation of the crystal coordinate system with respect to the material co-rotational coordinate system as

$$\mathbf{Q} = \begin{bmatrix} \cos\varphi_1\cos\varphi_2 - \sin\varphi_1\sin\varphi_2\cos\phi & \sin\varphi_1\cos\varphi_2 + \cos\varphi_1\sin\varphi_2\cos\phi & \sin\varphi_2\sin\phi \\ -\cos\varphi_1\sin\varphi_2 - \sin\varphi_1\cos\varphi_2\cos\phi & -\sin\varphi_1\sin\varphi_2 + \cos\varphi_1\cos\varphi_2\cos\phi & \cos\varphi_2\sin\phi \\ \sin\varphi_1\sin\phi & -\cos\varphi_1\sin\phi & \cos\phi \end{bmatrix} \quad (2.21)$$

where φ_1 , ϕ and φ_2 are the Bunge Euler angles of a grain in the undeformed state. Then the stress tensor in the crystal coordinate system can be expressed as (hat signs indicates the variable in the material co-rotational coordinate system)

$$\boldsymbol{\sigma} = \mathbf{Q}^T \hat{\boldsymbol{\sigma}} \mathbf{Q} \quad (2.22)$$

The resolved shear stress can be calculated from the stress tensor in the coordinate system as

$$\tau^{(\alpha)} = \boldsymbol{\sigma} : \mathbf{P}^\alpha \quad (2.23)$$

The backward Euler implicit scheme [109] is used in the numerical implementation to update the stress state. In the present dissertation, the rate-dependent constitutive crystal plasticity equations were employed in the commercial finite element program Abaqus Standard via a user material subroutine, UMAT (see Appendix A1).

2.1.3. Virtual microstructure model

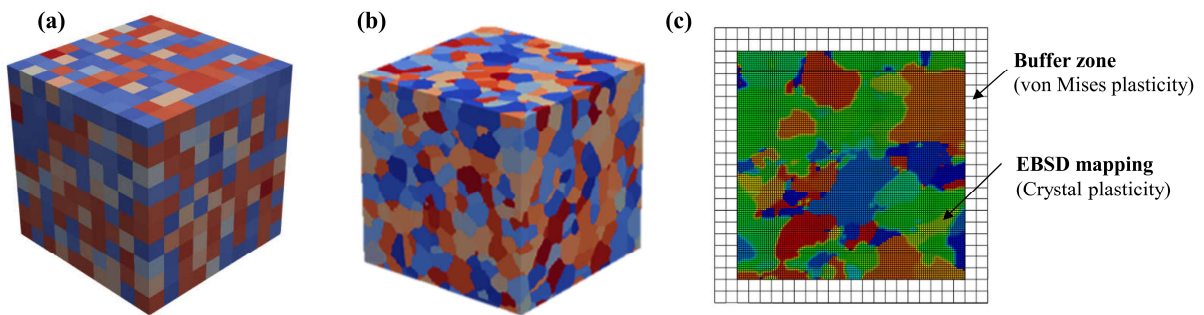


Fig. 2.5 Mesoscopic representative volume elements (RVEs): (a) voxel, (b) realistic and (c) microstructure mapping.

A virtual microstructure model known as representative volume element (RVE) is used to represent the microstructure morphology and properties of the polycrystalline material. Fig. 2.5 shows three types of RVEs which are assigned the crystallographic texture from the macroscopic EBSD measurement. For a voxel-typed RVE as shown in Fig. 2.5(a), each voxel element represents one grain and crystallographic texture information is assigned to each element. A voxel-typed RVE is widely used to simulate the macroscopic properties of the material owing to the low computational cost. For a realistic RVE as shown in Fig. 2.5(b), microstructure morphology with the grain structure is well reproduced and each grain consists of many voxel elements. The crystallographic texture is assigned to each grain. Its greatest advantage is to treat the interactions

among neighboring grains more realistically in the grain-scale analysis as grain size effect on macroscopic properties, grain growth during the recrystallization. However, it may increase the computational cost owing to the many elements in a single grain. For microstructure mapping RVE as shown in Fig. 2.5(c), the initial EBSD microstructure is directly mapped onto the finite element mesh. When coupling with advanced technique (in-situ EBSD), it is applicable for the analysis of surface grains effect on the deformation and failure behavior of the material. For specific mechanical problem, different boundary conditions are imposed on these mesoscopic RVEs in the CPFEM simulation. Then, the virtual material testing by CPFEM using mesoscopic RVE is performed to determine the macroscopic mechanical behaviors of the material as stress-strain response, plastic anisotropy, formability, phase constitutive properties and damage.

In this chapter, a voxel-typed RVE consisted of 1,000 elements (C3D8R, 8-node solid element with reduced integration) was used in the CPFEM predictions of mechanical behavior and yield loci of ultra-thin FSS sheet. Then the measured texture (Euler angles φ_1 , ϕ and φ_2) composed of 1,000 crystallographic orientations was assigned to the RVE as shown in Fig. 2.6. The deformation of RVE can be controlled by imposing the displacement boundary conditions on three representative nodes 100, 010 and 001 using the keyword “equation” in Abaqus input as follows

$$u^{X^+} = u^{X^-} + \varepsilon u^{n100} \quad (2.24)$$

where ε is the applied strain tensor, and u^{n100} is the displacement of the node 100. X^+ and X^- are the positive X-and negative X-planes, respectively.

Similarly, the following relations for the nodes on the Y-and Z-planes are paired as

$$u^{Y^+} = u^{Y^-} + \varepsilon u^{n010} \quad (2.25)$$

$$u^{Z^+} = u^{Z^-} + \varepsilon u^{n001} \quad (2.26)$$

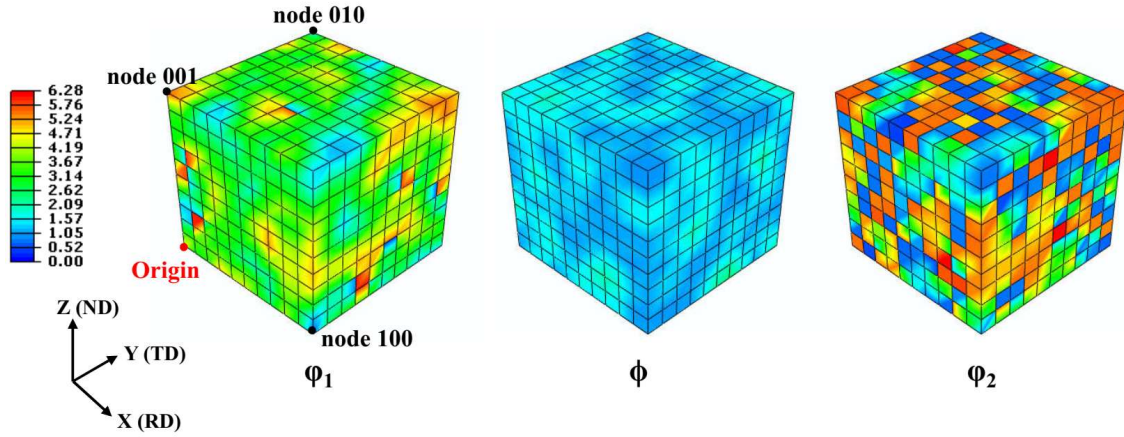


Fig. 2.6 Mesoscopic voxel-typed RVEs (Euler angles φ_1 , ϕ and φ_2 indicated by color).

2.2. Experimental procedure

2.1.1. Materials

In this study, the ultra-thin ferritic stainless steel (FSS) sheet with thickness of 0.08 mm was investigated. The FSS sheet materials were developed for the BPs of PEM fuel cell by the POSCO steel company. The FSS sheet materials consist of approximately 30% Cr which is one important characteristic of the materials. The chemical composition of the FSS sheet materials developed by POSCO [110] is shown in Table 2.1. With a very strong Cr passive layer, the FSS sheet materials will exhibit a very high corrosion resistance, which is one of the most important properties for not only fuel cell vehicle application but also home appliance and mobile products.

Table 2.1. Chemical compositions of the FSS sheet materials developed by POSCO steel company.

C	Si	Mn	P	S	Cr	Ni	Mo	N	Cu	Other elements
0.02	0.40	0.20	0.040	0.030	25.0-32.0	0.5	-	0.02	2.0	Nb/Ti

2.1.2. Uniaxial tensile test

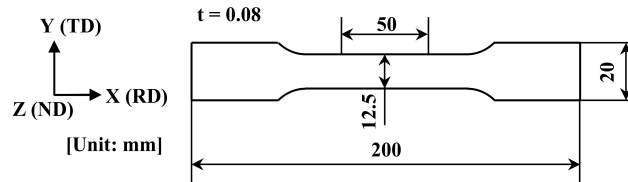


Fig. 2.7 Schematic of uniaxial tensile specimen of ultra-thin FSS sheet.

As shown in Fig. 2.1, rectangular dog-bone shaped tensile specimens were prepared to characterize the mechanical behavior of the ultra-thin FSS sheet. Uniaxial tensile tests were performed along rolling direction (RD), diagonal direction (DD) and transverse direction (TD). The tests were conducted at an engineering strain rate of 10^{-3} s^{-1} at room temperature. The directions in 0° , 45° and 90° correspond to the RD, DD and TD, respectively. The thickness direction corresponds to the normal direction (ND). The width and parallel gauge length of the specimen were 12.5 mm and 50 mm along the TD and RD, respectively. The tensile tests were carried out three times for each condition in order to verify the repeatability.

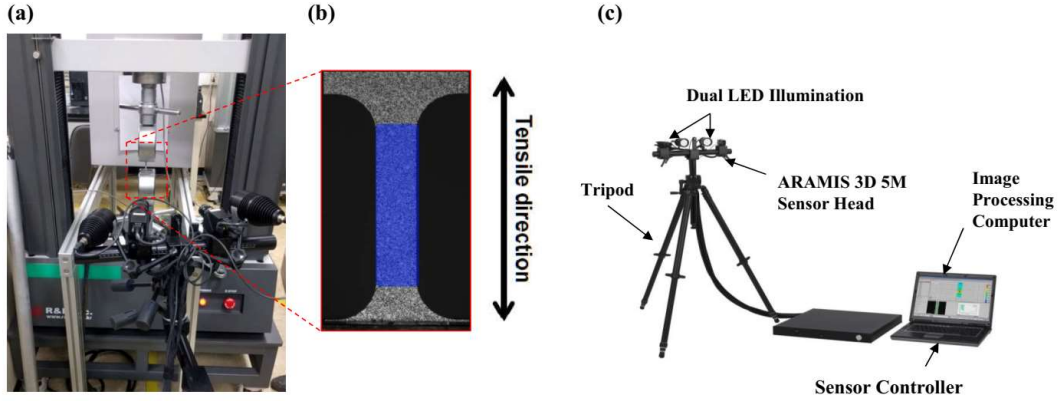


Fig. 2.8 Illustrations of (a) UTM uniaxial tension instrument, (b) digital image correlation (DIC) monitor and (c) ARAMIS 3D 5M system.

Fig. 2.8(a) shows the illustration of UTM instrument used for the uniaxial tensile tests of the ultra-thin FSS sheet. During the tests, the deformation behavior of tensile specimens was monitored by the digital image correlation (DIC) camera as shown in Fig. 2.8(b). Fig. 2.8(c) shows the ARAMIS 3D 5M system to measure the strains in the longitudinal and width directions. The image processing computer was used to observe the strains during the deformation. The r-value represents the plastic anisotropy of the material was calculated as follows

$$r = \frac{d\varepsilon_w}{d\varepsilon_t} \quad (2.27)$$

where $d\varepsilon_w$ and $d\varepsilon_t$ are the width and thickness strain increments, respectively. It is difficult to measure the strain in the thickness direction during the deformation, therefore, $d\varepsilon_t$ is generally calculated based on the volume consistency using the following equation as

$$d\varepsilon_l + d\varepsilon_w + d\varepsilon_t = 0 \quad (2.28)$$

where $d\varepsilon_l$ is the longitudinal strain increment. In addition, the planar anisotropy, Δr , is calculated as

$$\Delta r = \frac{r_0 + r_{90} - 2r_{45}}{2} \quad (2.29)$$

2.1.3. Microstructure measurement

Crystallographic texture of the FSS sheet specimen were characterized using an electron backscatter diffraction (EBSD) measurement in a field emission scanning electron microscope (FE-SEM). In order to obtain the crystallographic texture, a small square sample of 12 x 12 mm² was prepared from the as-received sheet specimen. The sample was resin-mounted and polished by a SiC paper, diamond suspensions up to 1 μm and colloidal silica. Then, the measurements were examined in three orthogonal planes perpendicular to the RD, TD and ND, respectively. The analyses were performed in an EBSD system (Hitachi SU-6600) with step sizes of 0.4 μm for the planes perpendicular to RD and TD, and 0.8 μm for the plane perpendicular to ND. Prior to the analyses of EBSD data, a cleanup procedure consisting of grain confidence index standardization followed by grain dilation was applied with a grain misorientation of 5° and an equivalent grain size of minimum 4 pixels. According to this procedure, the orientations of isolated pixels around identified grains were changed to match that of adjacent neighbors. A successful orientation correlation during the cleanup procedure was ensured by introducing a fine step size. The EBSD data of the FSS sheet was analyzed using the EDAX TSL OIM Analysis v.7.1.

2.3. Results and discussion

2.3.1. Mechanical properties

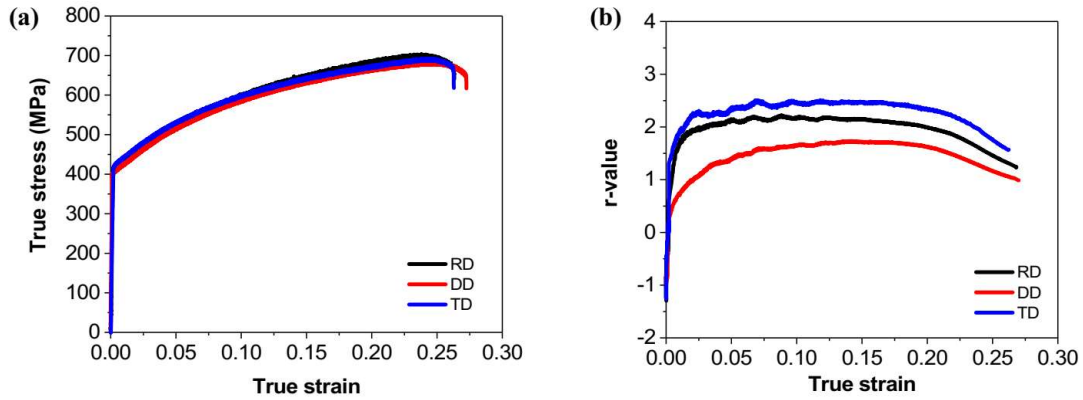


Fig. 2.9 (a) True stress-strain and (b) r-value curves of ultra-thin FSS sheet obtained from digital image correlation (DIC) analysis.

Table 2.2 Tensile properties of the ultra-thin FSS sheet.

	Yield stress [MPa]	Tensile stress [MPa]	Total elongation [%]	r-value	Δr
RD	416	702	27.8	1.84	0.59
DD	401	684	28.7	1.39	
TD	417	692	28.0	2.12	

Fig. 2.9(a) shows the true stress-strain curves of ultra-thin FSS sheet obtained by performing uniaxial tensile test along the RD, DD and TD. The tensile properties are summarized in Table 2.2. It reveals a negligible difference in the stress-strain responses among the loading directions. However, the evolution of r-value with respect to the true strain shows an apparent discrepancy between the different directions, as shown in Fig. 2.9(b).

2.3.2. Crystallographic texture

The measured crystallographic texture of the ultra-thin FSS sheet is given in Fig. 2.10. As shown in Fig. 2.10(a), a three-dimensional view of inverse pole figure (IPF) map was reconstructed by examining three orthogonal planes perpendicular to RD, TD and ND. The ND IPF map in Fig. 2.10(b) reveals that the initial microstructure has orientations parallel to the $\langle 111 \rangle$ direction with an equiaxed grain structure. The microstructure of the material contains a large number of grain population, totally 1,478 grains. The ultra-thin FSS sheet exhibits a fine microstructure with the average grain size of around $13 \mu\text{m}$ as shown in the grain size distribution in Fig. 2.10(c).

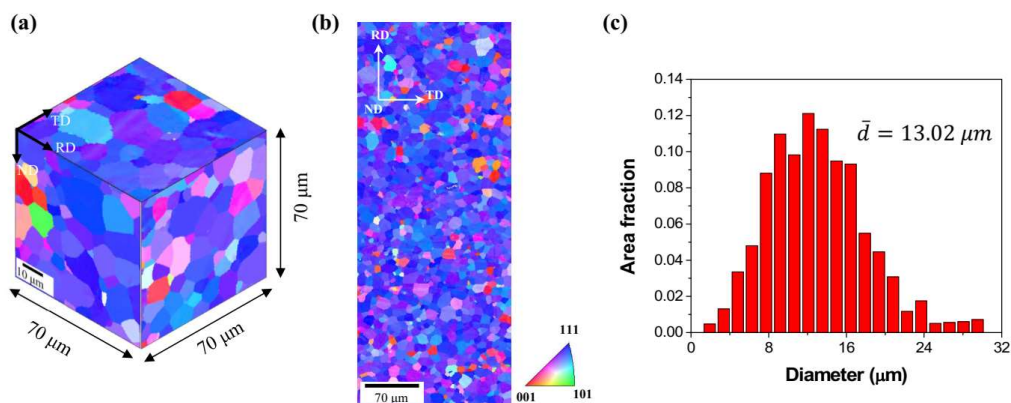


Fig. 2.10 (a) Reconstruction of three-dimensional view of IPF map, (b) ND IPF map and (c) grain size distribution of ultra-thin FSS sheet.

Fig. 2.11 shows the orientation distribution function (ODF) sections of measured texture of ultra-thin FSS sheet in comparison with the ideal orientations. The textures are shown in this figure using the $\varphi_2 = \text{constant}$ ($0-90^\circ$ in steps of 5°) ODF sections. It is found that the ultra-thin steel sheet clearly reveals a strong γ -fiber which are fiber textures with the $\langle 111 \rangle$ axis parallel to the ND. The γ -fiber is normally formed after cold rolling and annealing processes. It is noteworthy to mention that the strong γ -fiber can improve formability and reduce the effect of the planar anisotropy on

the material [111,112]. The measured crystallographic texture was used for CPFEM analysis as per Euler angles in Bunge definition.

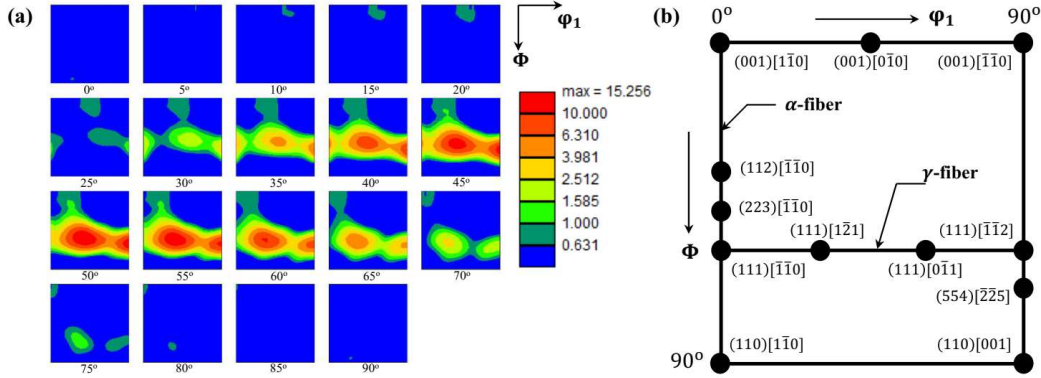


Fig. 2.11 (a) The ODF sections of measured textures of ultra-thin FSS sheet and (b) typical fiber texture for the position of important BCC orientations at $\varphi_2 = 45^\circ$.

2.3.3. Constitutive parameter identification

Table 2.3 shows the crystal plasticity hardening parameters used in the present study. For iron with cubic crystal structure, three anisotropic elasticity constants ($C_{11} = 242$ GPa, $C_{12} = 150$ GPa, $C_{33} = 112$ GPa) are adopted from literature [113]. Crystallographic slip was considered on the $12\{110\}\langle 111\rangle$ and $12\{112\}\langle 111\rangle$ slip systems for typical BCC metals. The constant parameters of reference shear strain rate, strain rate sensitivity and latent hardening coefficient are used as $\dot{\gamma}_0 = 0.001$ s $^{-1}$, $m = 0.05$ and $q = 1.4$, respectively. The initial hardening rate h_0 , initial CRSS τ_c , saturated CRSS τ_s , and strain hardening exponent a of two slip systems were assumed to be different and determined by fitting the measured stress-strain curves during uniaxial tensile tests along RD, DD and TD. The best fitted hardening parameters are given in Table 2.3. The CPFEM results show that the CRSS of $\{112\}\langle 111\rangle$ slip system is higher than that in the $\{110\}\langle 111\rangle$ slip

system. This is due to the addition of Cr atom in the FSS sheet material, which can lead to the increase of the CRSS for certain slip planes [114].

Table 2.3. Crystal plasticity hardening parameters of ultra-thin ferritic stainless steel.

	$\dot{\gamma}_0$ [1/s]	m	q	h_o [MPa]	τ_c [MPa]	τ_s [MPa]	a
{110}<111>	0.001	0.05	1.4	890	165	364	1.86
{112}<111>	0.001	0.05	1.4	1446	180	339	1.64

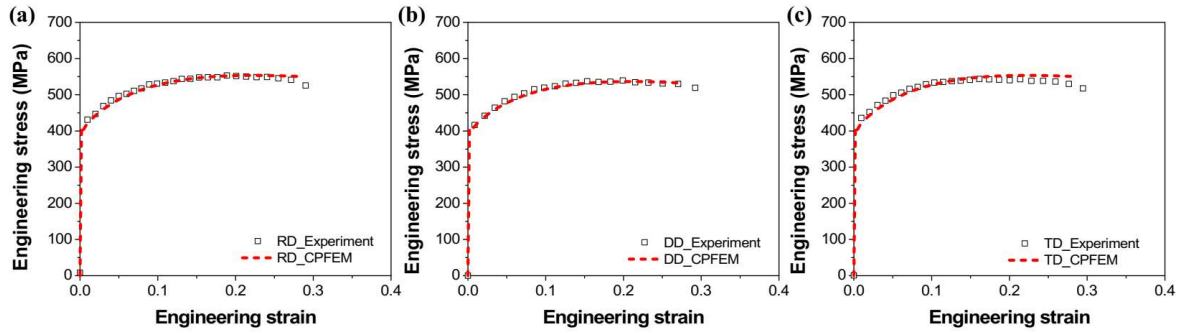


Fig. 2.12 Comparison of experimentally measured and CPFEM predicted stress-strain curves of ultra-thin FSS sheet in the (a) rolling direction (RD), (b) diagonal direction (DD) and (c) transverse direction (TD).

Fig. 2.12 shows the CPFEM predicted stress-strain curves in comparison with the experimental results along RD, DD and TD. It reveals that the CPFEM model can reproduce accurately the macroscopic responses of ultra-thin FSS sheet. The predicted stress-strain curves along RD, DD and TD are in good agreement with the experiments. In order to compare quantitatively, a measure of relative difference between predicted and experimental results is given as

$$Error = \frac{1}{N} \sum_{i=1}^N \left| \frac{\sigma_i^{exp} - \sigma_i^{pre}}{\sigma_i^{exp}} \right| \times 100 \quad (2.30)$$

where σ_i^{exp} and σ_i^{pre} are the experimental and predicted stresses, respectively, and N is the total number of stress data points. The calculated errors between predicted and experimental results are 3.6%, 4.8% and 5.1% for RD, DD and TD, respectively. It indicates that the present CPFEM model reasonably well captures the stress-strain behaviors with the error less than 6%, thus the hardening parameters are successfully identified.

2.3.4. Prediction of yield loci

In this section, the yield loci of ultra-thin FSS sheet was predicted by the CPFEM simulations in addition to the phenomenological constitutive models by Hill's 1948 quadratic [115] and Yld2000-2d non-quadratic [116] yield functions. Due to the increased number of material parameters, it is tough and time-consuming to calibrate the yield functions. In addition, the most concerns in the community of sheet metal forming, the microstructural heterogeneity, is not considered in the phenomenological yield functions. In contrast, the CPFEM plays an important role in exploring the microstructural evolution and plastic anisotropy of sheet metals as well as calibrating advanced yield functions.

The details of Hill's 1948 and Yld2000-2d yield functions for calculating the yield loci are explained in Appendix A2 and A3, respectively. In the CPFEM simulations, the RVE in Fig. 2.6 was subjected to proportional deformation in different directions, then stress states located on the yield loci were obtained. Four series of simulations were performed by changing the prescribed deformation in the periodic boundary conditions. In the first series, the displacement in the representative node 100 in the RD (X) direction was kept constant while the displacement in the

representative node 010 in the TD (Y) direction was varied between the simulations. Thus, the prescribed displacements are defined as

$$u_x = u_0, u_y = \alpha u_0 \quad (2.31)$$

where u_0 is a constant reference displacement, α is varied within the range $[-1,+1]$ with the interval of 0.2. In the second series, the displacement in the representative node 100 in the RD (X) direction was varied between the simulations while the displacement in the representative node 010 in the TD (Y) direction was kept constant. Thus, the prescribed displacements are defined as

$$u_x = \alpha u_0, u_y = u_0 \quad (2.32)$$

In the first and second series, the CPFEM simulations of biaxial tension were performed. For the third and fourth series, the CPFEM simulations of biaxial pressure were carried out. Similarly, the prescribed displacements in the third and fourth series are defined, respectively, as

$$u_x = -u_0, u_y = \alpha u_0 \quad (2.33)$$

$$u_x = \alpha u_0, u_y = -u_0 \quad (2.34)$$

In order to determine the yield loci, the yield stress point for each simulation was calculated at the yield point of the material. In addition, the r-value and yield stress point obtained from the CPFEM simulation were used to calibrate the anisotropy coefficients of the Hill'1948 and Yld2000-2d yield functions. It is noted that the yield stress point for each simulation was normalized by the uniaxial flow stress in the RD.

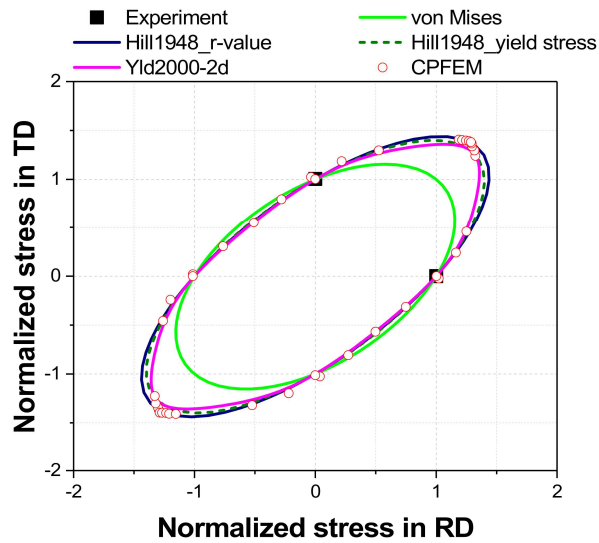


Fig. 2.13 Yield loci predictions of ultra-thin FSS sheet compared with the experimental results.

Fig. 2.13 shows the predictions of yield loci of ultra-thin FSS sheet by the CPFEM and phenomenological constitutive models (Hill'1948 and Yld2000-2d yield functions). The predicted result using von Mises yield function was also shown in Fig. 2.13. The experimental results of normalized yield stress along the RD and TD were included for the comparison. For the Hill'1948 yield function, the anisotropy coefficients were calibrated by two methods using r-value and yield stress, accordingly the yield loci. Fig. 2.13 reveals that the CPFEM prediction of yield loci is in good agreement with the experimental results in the uniaxial tension and consistent with the results of Hill'1948 and Yld2000-2d yield functions. In the equi-biaxial tension and pressure, the yield loci of the CPFEM, Hill'1948 and Yld2000-2d yield functions are sharper than that of the von Mises. It indicates that the shaper yield loci corresponds to the lower limit strains in the material at the biaxial stretching mode. The literature reported that the lower FLD in the equi-biaxial range is obtained as the yield loci is shaper [117–119].

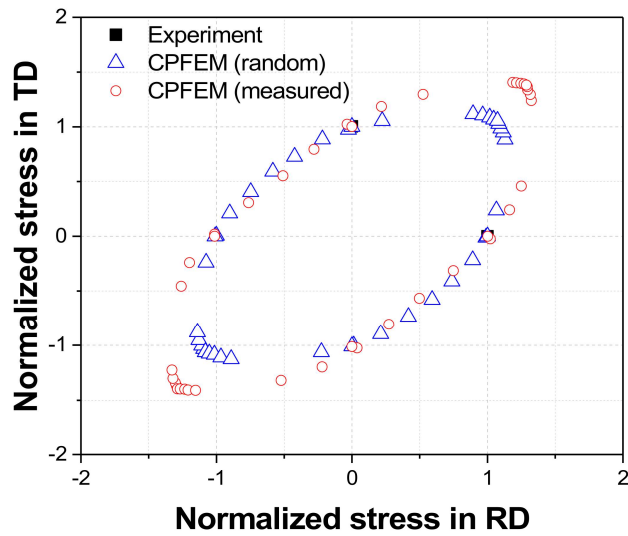


Fig. 2.14 Effect of crystallographic texture on the yield loci predictions of ultra-thin FSS sheet.

Furthermore, the effect of initial crystallographic texture on the prediction of yield loci is shown in Fig. 2.14. The CPFEM predictions of yield loci were performed using RVE by considering the measured and random textures. Compared to the random texture, the measured texture results in the lower yield stresses for stress states between uniaxial and shear regions and higher yield stresses for stress states between the uniaxial and equi-biaxial regions. The results show that the predicted yield loci by taking into account the measured texture is shaper that that of considering the random texture. This indicates that the predicted FLD by considering measured texture will be lower than that of considering random texture which be confirmed in following chapter. It can be concluded that the crystallographic texture significantly affects the macroscopic mechanical behavior of the material.

2.4. Conclusions

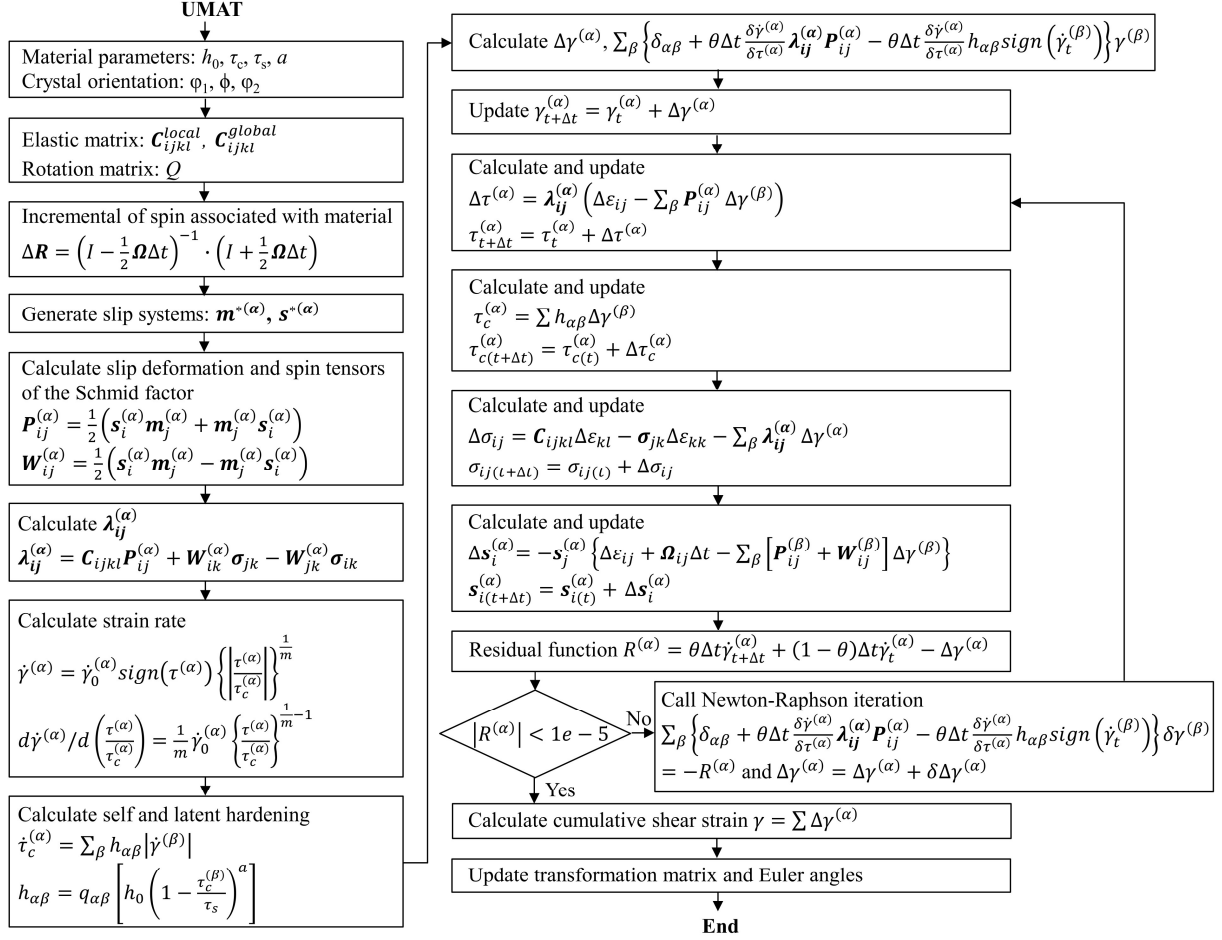
This chapter briefly introduced the virtual material testing with the concept of crystal plasticity finite element method (CPFEM) to be a robust and potential approach for remedying experimental methods. The CPFEM allows to simulate the different deformation mechanisms by explicitly taking into account the mechanical interactions among the crystals in a polycrystal under the complex external and internal boundary conditions. The CPFEM simulations can perform both at microscopic and macroscopic scales in the predictions of grain size effect, lattice defects (dislocations, twins, martensite), texture evolution, mechanical behavior, forming limits, material failure. The virtual material testing by microstructure-based simulation was performed using CPFEM.

The application of CPFEM in this chapter was for predictions of mechanical behavior and yield loci of the ultra-thin ferritic stainless steel (FSS) steel sheet for bipolar plate in PEM fuel cell. The macroscopic properties and the crystallographic texture of the FSS sheet were characterized by uniaxial tensile tests and electron backscatter diffraction (EBSD) measurement. The ultra-thin FSS sheet exhibited a fine microstructure with the average grain size of 13 μm . It was found that the ultra-thin steel sheet clearly revealed a strong γ -fiber which was a fiber texture with the $\langle 111 \rangle$ axis parallel to the normal direction. The CPFEM model was then developed and used in the prediction of stress-strain responses and yield loci. Firstly, the CPFEM simulations using representative volume element (RVE) in consideration of measured texture were carried out to identify the hardening parameters by the trial-error method. The predicted stress-strain response was compared with the experimental results. It revealed that the CPFEM model well reproduced the experimental stress-strain curves along the rolling direction (RD), diagonal direction (DD) and transverse direction (TD).

Then, a series of CPFEM simulations were performed to determine the stress states located on the yield loci. It revealed that the CPFEM prediction of yield loci was in good agreement with the experimental results and consistent with the results of Hill' 1948 and Yld2000-2d yield functions. The predicted yield loci of the CPFEM, Hill' 1948 and Yld2000-2d yield functions were sharper than that of the von Mises in the equi-biaxial tension and pressure regions. Furthermore, the crystallographic texture significantly affected the yield loci of the material. The results showed that the predicted yield loci by taking into account the measured texture was sharper than that of considering the random texture. The sharper yield loci indicated the lower forming limit strains in the material.

Appendix of Chapter 2

A1. Flowchart of UMAT calculation procedure



A2. Hill's 1948 quadratic yield function

The Hill's 1948 quadratic yield function [115] is one of the simplest and most widely used yield functions to determine the plastic anisotropy of the material. The Hill's 1948 yield function is given as follows

$$\phi = F(\sigma_{yy} - \sigma_{zz})^2 + G(\sigma_{zz} - \sigma_{xx})^2 + H(\sigma_{xx} - \sigma_{yy})^2 + 2L\sigma_{yz}^2 + 2M\sigma_{zx}^2 + 2N\sigma_{xy}^2 = 2\bar{\sigma}^2 \quad (\text{A.1})$$

where σ_{xx} , σ_{yy} and σ_{zz} are the stresses represented along the orthogonal sheet-symmetry directions in the rolling (RD or x), transverse (TD or y) and normal (ND or z) directions, respectively. σ_{xy} , σ_{yz} and σ_{zx} are the shear stresses in xy, yz and zx directions, respectively. The anisotropy coefficients of F, G, H, L, M and N can be determined from the results of the uniaxial tensile tests performed along RD, DD and TD. When $F = G = H = 1$ and $L = M = N = 3$, the Hill's 1948 quadratic yield function reduces to the von-Mises yield function. For the plane stress condition ($\sigma_{zz} = \sigma_{yz} = \sigma_{zx} = 0$), the anisotropy coefficients reduce to four as follows

$$\phi = (G + H)\sigma_{xx}^2 + (F + H)\sigma_{yy}^2 - 2H\sigma_{xx}\sigma_{yy} + 2N\sigma_{xy}^2 = 2\bar{\sigma}^2 \quad (\text{A.2})$$

The r-value and yield stress-based methods are commonly used to calculate the anisotropy coefficients of Hill's 1948 quadratic yield function. When the r-values along 0° , 45° and 90° with respect to the RD are obtained, the anisotropy coefficients are determined as follows

$$F = \frac{r_0}{r_{90}(1+r_0)} 2 \left(\frac{\bar{\sigma}}{\sigma_0} \right)^2 \quad (\text{A.3})$$

$$G = \frac{1}{1+r_0} 2 \left(\frac{\bar{\sigma}}{\sigma_0} \right)^2 \quad (\text{A.4})$$

$$H = \frac{r_0}{1+r_0} 2 \left(\frac{\bar{\sigma}}{\sigma_0} \right)^2 \quad (\text{A.5})$$

$$N = \frac{(r_0+r_{90})(2r_{45}+1)}{2r_{90}(1+r_0)} 2 \left(\frac{\bar{\sigma}}{\sigma_0} \right)^2 \quad (\text{A.6})$$

The four anisotropy coefficients of Hill's 1948 quadratic yield function can be also determined using the stress ratios as follows

$$F = (\bar{\sigma}/\sigma_{90})^2 + (\bar{\sigma}/\sigma_b)^2 - (\bar{\sigma}/\sigma_0)^2$$

$$G = (\bar{\sigma}/\sigma_b)^2 + (\bar{\sigma}/\sigma_0)^2 - (\bar{\sigma}/\sigma_{90})^2$$

$$H = (\bar{\sigma}/\sigma_0)^2 + (\bar{\sigma}/\sigma_{90})^2 - (\bar{\sigma}/\sigma_b)^2$$

$$N = 4(\bar{\sigma}/\sigma_{45})^2 - (\bar{\sigma}/\sigma_b)^2$$

where $\bar{\sigma} = \sigma_0$ or σ_b . σ_0 , σ_{45} , σ_{90} and σ_b are the yield stresses obtained by uniaxial tension tests at 0° , 45° and 90° with respect to the RD and balanced biaxial tension test, respectively.

A3. Yld2000-2d non-quadratic anisotropic yield function

The non-quadratic anisotropic yield function, namely, Yld2000-2d was firstly introduced by Barlat et al. [116] for plane stress states. In this study, the Yld2000-2d yield function was also employed to predict the plastic anisotropic properties and yield loci of ultra-thin FSS sheet. The Yld2000-2d yield function is defined as follows

$$\phi = \phi' + \phi'' = 2\bar{\sigma}^a \quad (\text{A.7})$$

where

$$\phi' = |X'_1 - X'_2|^a \text{ and } \phi'' = |2X''_2 + X''_1|^a + |2X''_1 + X''_2|^a \quad (\text{A.8})$$

\mathbf{X}' and \mathbf{X}'' are linearly transformed stress tensors and subscripts 1 and 2 indicate their principal values. “ a ” is the yield function exponent characterizing the crystal structure of the material. The exponent a is recommended to be 6 and 8 for body-centered cubic (BCC) and face-centered cubic (FCC) materials, respectively [120,121]. Two linear transformations of the Cauchy stress $\boldsymbol{\sigma}$ into \mathbf{X}' and \mathbf{X}'' are given as follows

$$\mathbf{X}' = \mathbf{C}'\mathbf{s} = \mathbf{C}'\mathbf{T}\boldsymbol{\sigma} = \mathbf{L}'\boldsymbol{\sigma} \quad (\text{A.9})$$

$$\mathbf{X}'' = \mathbf{C}''\mathbf{s} = \mathbf{C}''\mathbf{T}\boldsymbol{\sigma} = \mathbf{L}''\boldsymbol{\sigma} \quad (\text{A.10})$$

where

$$\mathbf{T} = \begin{bmatrix} 2/3 & -1/3 & 0 \\ -1/3 & 2/3 & 2/3 \\ 0 & 0 & 1 \end{bmatrix} \quad (\text{A.11})$$

Then, the product of two transformations are given in matrix forms of \mathbf{L}' and \mathbf{L}'' as follows

$$\begin{bmatrix} X'_{xx} \\ X'_{yy} \\ X'_{xy} \end{bmatrix} = \begin{bmatrix} L'_{11} & L'_{12} & 0 \\ L'_{21} & L'_{22} & 0 \\ 0 & 0 & L'_{66} \end{bmatrix} \begin{bmatrix} \sigma_{xx} \\ \sigma_{yy} \\ \sigma_{xy} \end{bmatrix} \quad (\text{A.12})$$

$$\begin{bmatrix} X''_{xx} \\ X''_{yy} \\ X''_{xy} \end{bmatrix} = \begin{bmatrix} L''_{11} & L''_{12} & 0 \\ L''_{21} & L''_{22} & 0 \\ 0 & 0 & L'_{66} \end{bmatrix} \begin{bmatrix} \sigma_{xx} \\ \sigma_{yy} \\ \sigma_{xy} \end{bmatrix} \quad (\text{A.13})$$

$$\begin{bmatrix} L'_{11} \\ L'_{12} \\ L'_{21} \\ L'_{22} \\ L'_{66} \end{bmatrix} = \begin{bmatrix} 2/3 & 0 & 0 \\ -1/3 & 0 & 0 \\ 0 & -1/3 & 0 \\ 0 & 2/3 & 0 \\ 0 & 0 & 1 \end{bmatrix} \begin{bmatrix} \alpha_1 \\ \alpha_2 \\ \alpha_7 \end{bmatrix} \quad (\text{A.14})$$

$$\begin{bmatrix} L''_{11} \\ L''_{12} \\ L''_{21} \\ L''_{22} \\ L''_{11} \end{bmatrix} = \frac{1}{9} \begin{bmatrix} -2 & 2 & 8 & -2 & 0 \\ 1 & -4 & -4 & 4 & 0 \\ 4 & -4 & -4 & 1 & 0 \\ -2 & 8 & 2 & -2 & 0 \\ 0 & 0 & 0 & 0 & 9 \end{bmatrix} \begin{bmatrix} \alpha_3 \\ \alpha_4 \\ \alpha_5 \\ \alpha_6 \\ \alpha_8 \end{bmatrix} \quad (\text{A.15})$$

Due to the orthotropic symmetry of the rolled sheet, the eight independent anisotropy coefficients $\alpha_1 - \alpha_8$ are used to determine the linear transformation tensors \mathbf{L}' and \mathbf{L}'' . The results of the uniaxial tension tests performed at 0° , 45° and 90° with respect to the RD and balanced biaxial tension tests are used to calculate the anisotropy coefficients $\alpha_1 - \alpha_8$.

CHAPTER 3

FORMING LIMIT DIAGRAM OF ULTRA-THIN STEEL SHEET

The purpose of this chapter was to determine the formability of ultra-thin FSS bipolar plate for PEM fuel cell. The Nakazima test was performed to obtain the experimental FLD. The coupled CPFEM–MK model was developed to predict the FLD of ultra-thin FSS sheet under various loading paths ($-0.5 \leq \rho \leq 1$). The voxel-typed RVE considering the measured texture was used in this analysis. The effects of imperfection factor and initial material texture on the formability were investigated. In addition, the evaluation of FLD by the Hill's, Swift's and Hora's necking instability criterion (NIC) models without consideration of geometrical imperfection were also studied to assess the role of geometrical imperfection in the FLD prediction.

3.1. Experimental procedure

3.1.1. Specimen preparation

The FSS sheet with the thickness of 0.08 mm was used to fabricate the FLD specimens using an electrical discharge machining (EDM). Fig. 3.1 shows the schematic of specimen geometries used in the FLD test. Eight [29] standard specimens with the blank width in range of 20~200 mm were prepared for the Nakazima test to obtain the entire FLD curve. The shaft length and fillet radius of specimens are 40 and 30 mm, respectively, as indicated in Fig. 3.1. All specimens were produced with the major and minor strains parallel to the transverse and rolling directions, respectively. Prior to conducting the Nakazima test, the speckle pattern was sprayed using black and white paint on the surface of specimens to measure and analyze the deformation of specimens by using ARAMIS digital image correlation (DIC) camera as shown in Fig. 3.2(a).

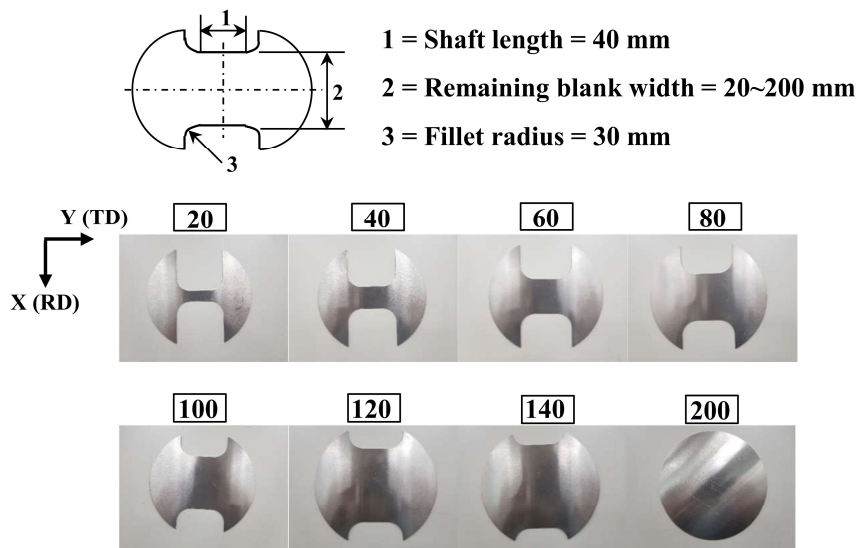


Fig. 3.1 Illustration of initial geometry of the ultra-thin FSS sheet specimens for the FLD test.

3.1.2. Formability test

The FLD of ultra-thin FSS sheet were determined by Nakazima test using Erichsen universal sheet testing machine as depicted in Fig. 3.2(a). The tests were performed using a hemisphere punch as shown in Fig. 3.2(b). The punch moved with speed of 0.5 mm/s and blank holding force of 40~55 kN was applied. The tests were conducted two times with the same conditions at room temperature for each strain path. During the Nakazima test, the undesired fracture can occur at the tool and specimen interaction due to the friction, which are the key to perform the test successfully. Therefore, graphite-teflon-graphite was used as a lubrication in order to minimize friction between the punch and sheets.

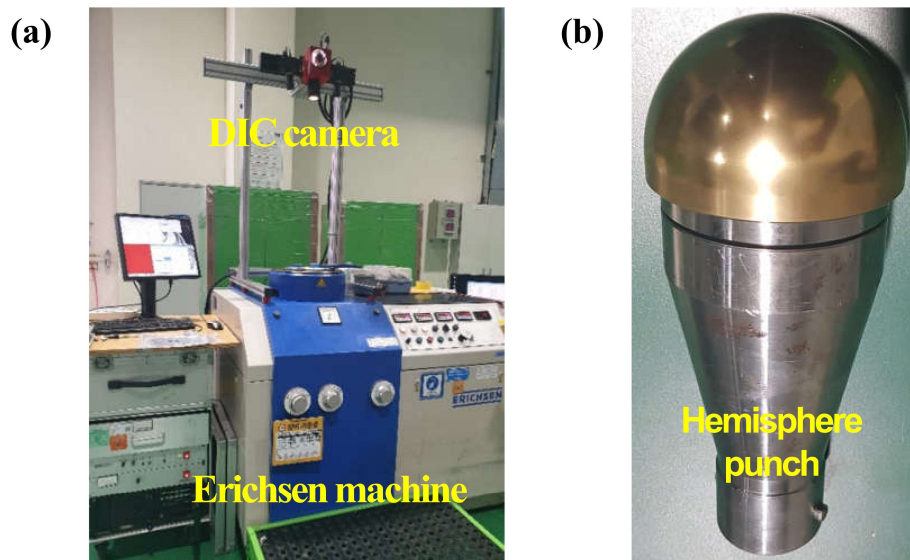


Fig. 3.2 Illustration of (a) Erichsen universal sheet testing machine, digital image correlation (DIC) camera and (b) hemisphere punch used in the FLD test.

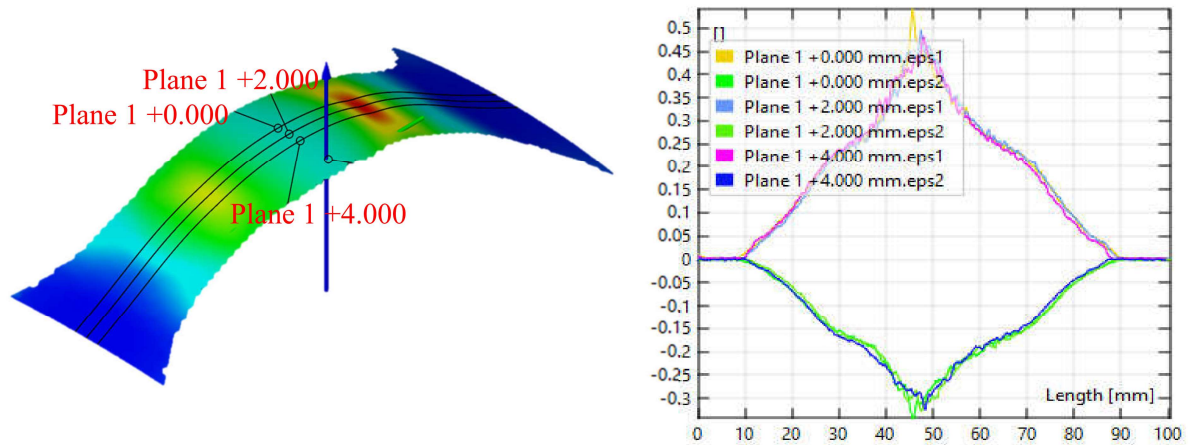


Fig. 3.3 Illustration of digital image correlation (DIC) analysis for measuring the strain history of FLD specimens during the loading process.

The strain history in the specimens during the loading process was measured using the ARAMIS DIC camera with a shooting speed of 6 shots/s. Then, as shown in Fig. 3.3, the three planes with interval of 2 mm perpendicular to the fracture line in the DIC analysis were defined to calculate the major and minor strains of FLD. For each specimen, three values of major and minor strains were obtained.

3.2. Theoretical approach

3.2.1. Combined CPFEM and MK model

In this work, CPFEM in conjunction with MK model was developed for forming limit analysis of ultra-thin FSS sheet as shown in Fig. 3.4. For the sake of simplifying the calculation and reducing the computational cost, the pre-existing imperfection or a groove defined by the inhomogeneity factor f_0 was assumed to be perpendicular to the major loading direction

corresponding to the X axis (RD). Two RVEs, namely RVE-A and RVE-B, were considered in order to simulate the responses of the polycrystalline material. As shown in Fig. 3.4, the groove thickness denoted as t_0^B is marginally reduced and defined by $t_0^B = f_0 t_0^A$, where t_0^A is the initial thickness and the superscripts A and B represent the outer and groove regions, respectively. Thus, the localization is initiated from the groove region due to the reduction of thickness.

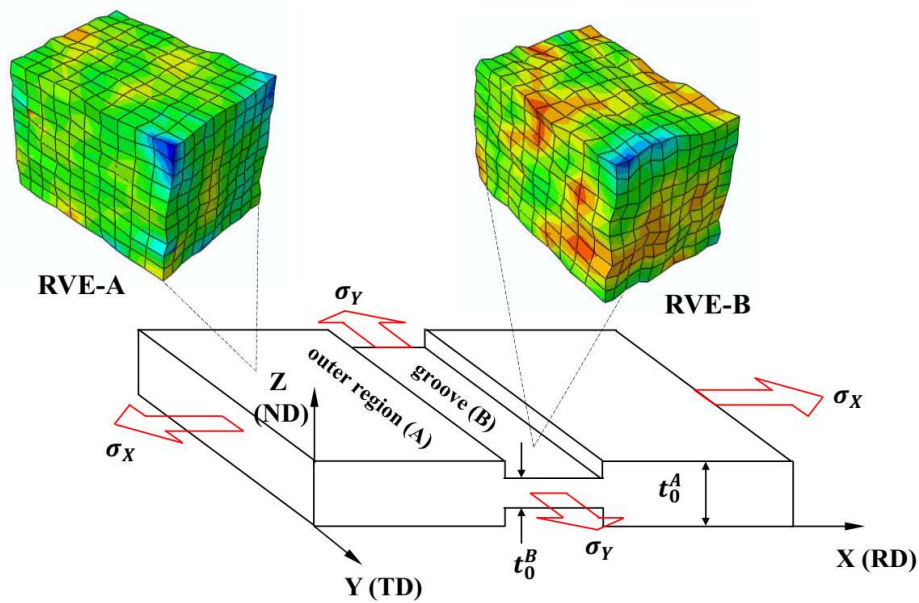


Fig. 3.4 Schematic of combined CPFEM–MK model for FLD prediction of ultra-thin FSS sheet.

The initial crystallographic texture was assigned to the virtual microstructure RVE for the forming limit analysis. As shown in Fig. 3.5(a), a voxel-typed RVE was generated by considering the measured texture. A total of 1,000 (10 x 10 x 10) crystallographic orientations were assigned to the RVEs composed of 1,000 elements (C3D8R, 8-node solid element with reduced integration), as shown in Fig. 3.5(b). In order to simulate a large part of the material by using RVE, a periodic boundary condition was commonly imposed. Fig. 3.5(b) shows a FE mesh with definition of four nodes at vertices. The origin is fixed and their representative nodes 100, 010 and 001 are used to

impose the displacement boundary conditions. The relationship between displacements of the nodes on the positive X-and negative X-planes, denotes as X^+ and X^- , were expressed by using the keyword “equation” in Abaqus input as follows

$$u^{X^+} = u^{X^-} + \varepsilon u^{n100} \quad (3.35)$$

where ε is the applied strain tensor, and u^{n100} is the displacement of the node 100, as shown in Fig. 3.5(b).

Similarly, the following relations for the nodes on the Y-and Z-planes are paired as

$$u^{Y^+} = u^{Y^-} + \varepsilon u^{n010} \quad (3.36)$$

$$u^{Z^+} = u^{Z^-} + \varepsilon u^{n001} \quad (3.37)$$

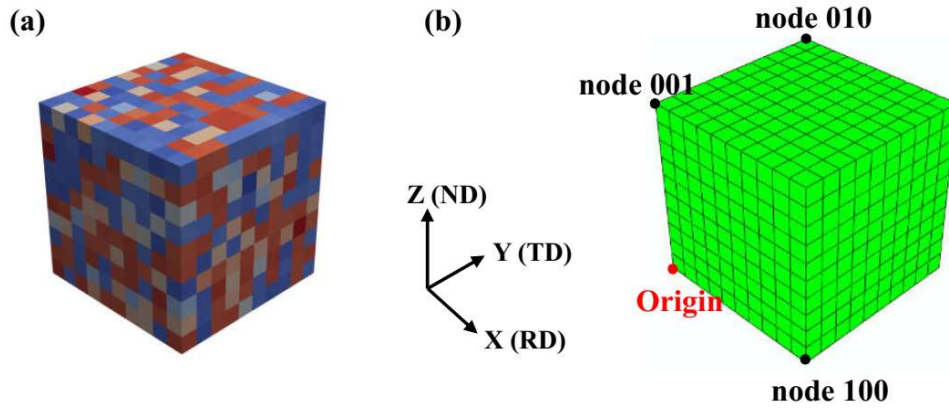


Fig. 3.5 Illustration of (a) voxel-typed RVE and (b) FE mesh with definition of nodes at vertices.

By imposing the displacement boundary conditions on three representative nodes 100, 010 and 001, the deformation of RVE can be controlled. In the MK model, the following equilibrium and compatibility conditions should be satisfied during loading with constant strain rate ratio ($\rho = \dot{\varepsilon}_Y^A / \dot{\varepsilon}_X^A$) as

$$F_X^A = F_X^B \text{ or } \sigma_X^A t_X^A = \sigma_X^B t_X^B \quad (3.38)$$

$$\varepsilon_Y^A = \varepsilon_Y^B \quad (3.39)$$

where F is the force, and t is the sheet thickness. It is noteworthy to mention that the effect of shear compatibility was negligible on the predicted forming limit strains as reported in the literature [35]. Therefore, the shear compatibility condition is not considered in the present study.

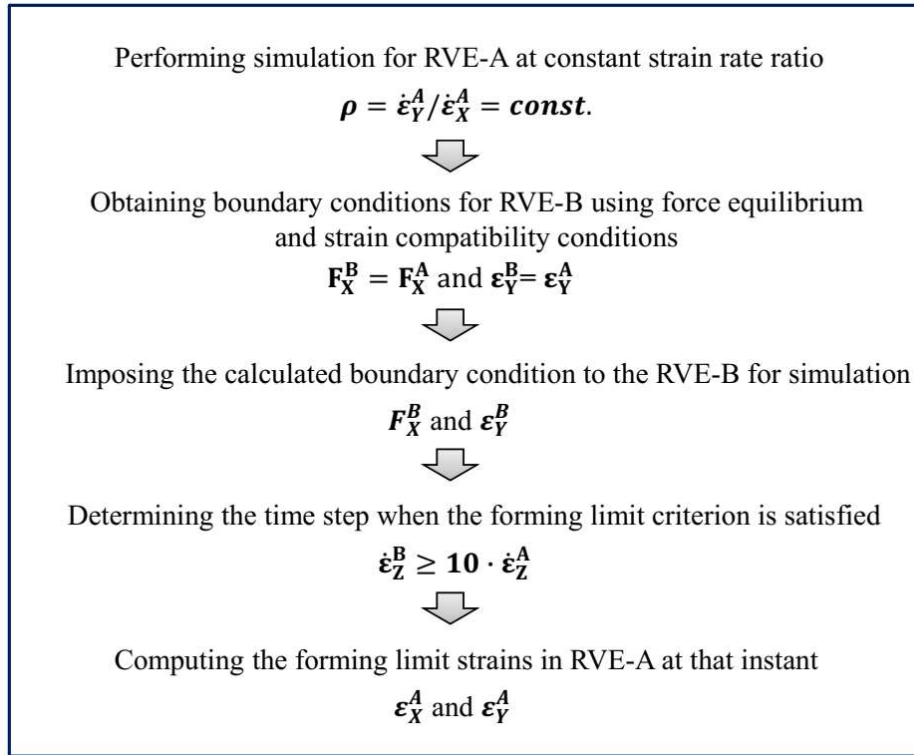


Fig. 3.6 Flowchart of combined CPFEM–MK model for FLD prediction of ultra-thin FSS sheet.

Fig. 3.6 shows the overall procedure to predict FLD using combined CPFEM–MK approach in this study. Firstly, the finite element analysis for RVE-A was performed at constant strain rate ratio ρ ($-0.5 \leq \rho \leq 1$) corresponding to the loading path. Then, the force and strain obtained from the RVE-A simulated results were calculated for the boundary conditions in the RVE-B using Eqs.

(3.4, 3.5). Next, RVE-B was simulated with the determined boundary conditions. The forming limit criterion was met when the ratio of thickness strain increment in the RVE-B to that in the RVE-A exceeded 10. Finally, the strains in the RVE-A at that instant was defined as the forming limit strains. The same procedure was repeated for different strain rate ratios to obtain the entire FLD curve.

3.2.2. Necking instability criterion (NIC) model

In addition to the MK approach considering the existed geometrical imperfection as a necking instability criterion (NIC), three different NICs originally proposed by Hill [122], Swift [123] and Hora et al. [124] were also used to evaluate the forming limit of ultra-thin FSS sheet. Normally, there are two different stages in the necking process, namely diffuse necking and localized necking. The condition for a diffuse necking is derived at the moment of the maximum force as

$$dF = d(\sigma_x A) = d\sigma_x A + \sigma_x dA = 0 \quad (3.40)$$

where F is the force, σ_x is the stress and A is the section area. Based on this condition, Hill [122] and Swift [123] proposed the criterions for localized necking as Eq. (3.7) and Eq. (3.8), respectively.

$$\frac{d\sigma_x}{d\varepsilon_x} = \sigma_x (1 + \beta) \quad (3.41)$$

$$\frac{d\sigma_x}{d\varepsilon_x} = \sigma_x \quad (3.42)$$

In the conventional NICs, only the effect of hardening behaviors was considered. Furthermore, Hora et al. [124] extended the formulation of NIC to take into account the strain ratio ($\beta = d\varepsilon_y / d\varepsilon_x$) as the additional hardening effect induced by the transformation of stress states. Therefore, the principal stress σ_x is expressed by a function of both strain hardening and strain ratio as

$$d\sigma_x = \frac{\partial\sigma_x}{\partial\varepsilon_x} d\varepsilon_x + \frac{\partial\sigma_x}{\partial\beta} \cdot d\beta \quad (3.43)$$

Substituting Eq. (3.9) into the Eq. (3.8), the Hora's NIC can be obtained as

$$\frac{\partial\sigma_x}{\partial\varepsilon_x} d\varepsilon_x + \frac{\partial\sigma_x}{\partial\beta} \cdot d\beta = \sigma_x d\varepsilon_x \quad (3.44)$$

Eq. (3.10) is rewritten as

$$\frac{\partial\sigma_x}{\partial\varepsilon_x} + \frac{\partial\sigma_x}{\partial\beta} \cdot \frac{\partial\beta}{\partial\varepsilon_x} = \sigma_x \quad (3.45)$$

The more detailed descriptions of Hill, Swift and Hora's NICs were described in the literature [122–124]. In this work, the simulated results in the outer region (RVE-A) were used to calculate the Eqs. (3.7, 3.8, 3.11) for the theoretical evaluation of FLD in comparison with the numerical calculation using MK model.

3.3. Results and discussion

3.3.1 Experimental FLD

Fig. 3.7 shows the fractured specimens obtained by the Nakazima tests. In the formability test, the Nakazima experiments were performed two times to evaluate the repeatability of the tests. As indicated in Fig. 3.7, buckles are observed in the fractured specimens near the biaxial stretching conditions. However, this may not significantly affect the final level and shape of the FLD curve. The literature also reported that although the wrinkling and buckles were observable in the fractured specimens in the Nakazima test, the FLD determination by Nakazima test was similar to the result obtained by the modified Marciniak test [30]. Furthermore, the undesired fracture is unobservable in the fractured specimens, indicating that the Nakazima test were successfully performed to determine the FLD of ultra-thin FSS sheet.

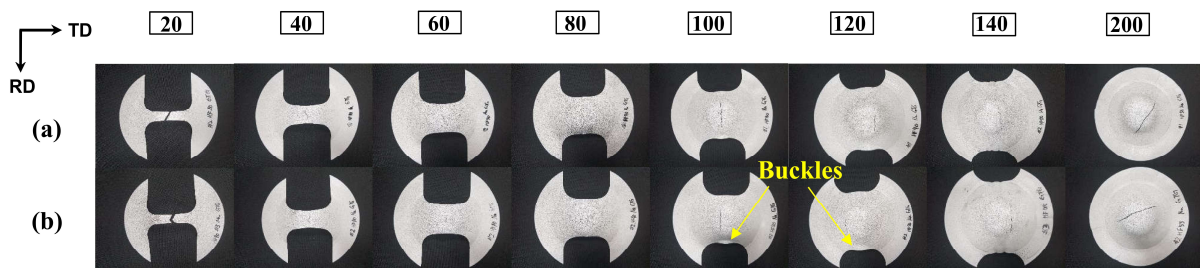


Fig. 3.7 Fractured specimens of ultra-thin FSS sheet from the formability test for the (a) first and (b) second Nakazima experiments.

Figs. 3.8 and 3.9 show the DIC analysis of specimens during the first and second Nakazima tests. The results are used to calculate the major and minor strains for plotting the FLD curve. The DIC results reveal that the localized deformation during the Nakazima test is apparently observed, except for the specimen with the largest blank width of 200 mm subjected to the equibiaxial

condition. Such a localized deformation results in the onset of fracture during the deformation of ultra-thin FSS sheet.

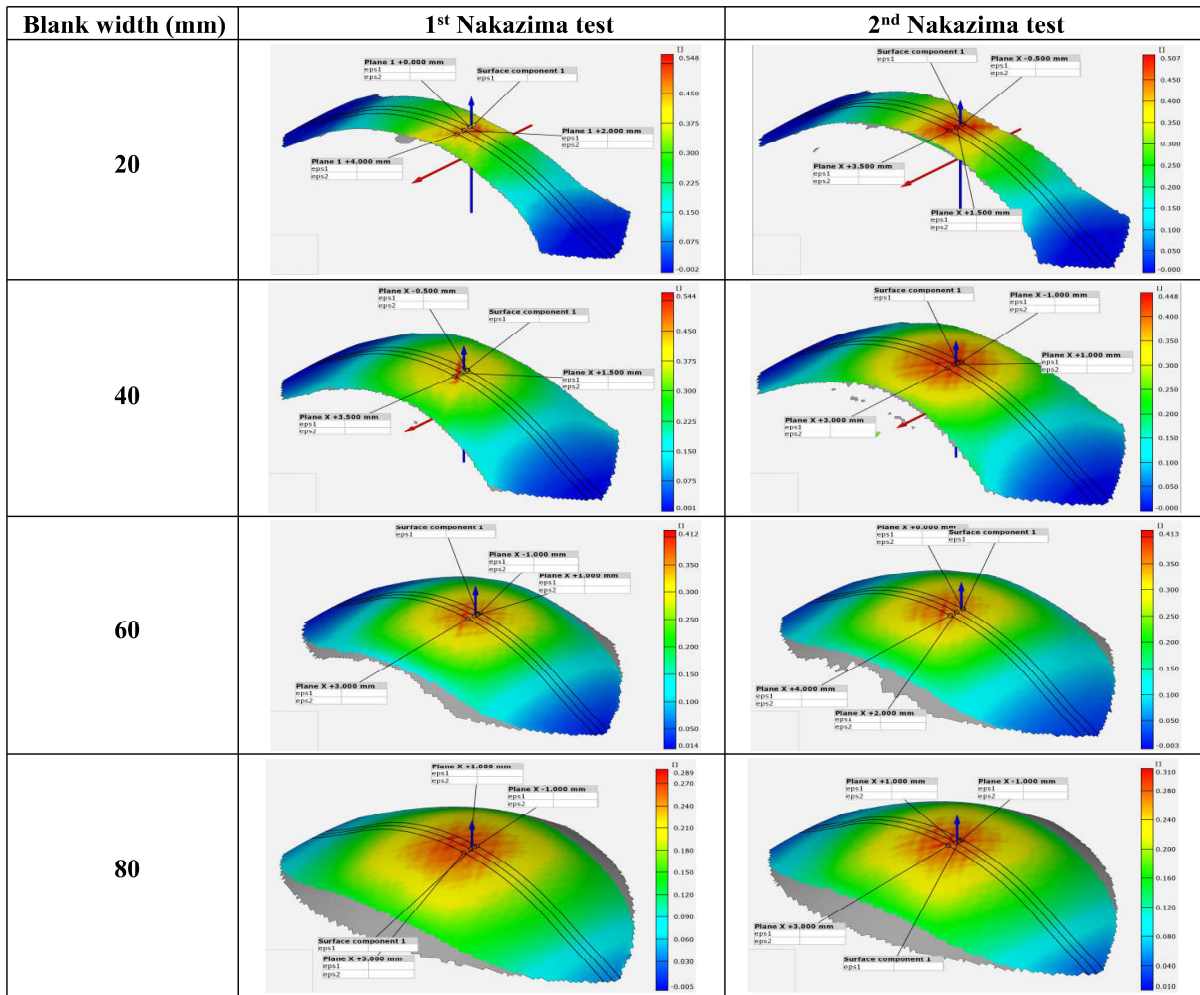


Fig. 3.8 Digital image correlation (DIC) analysis of the specimens with the blank widths of 20~80 during the first and second Nakazima experiments.

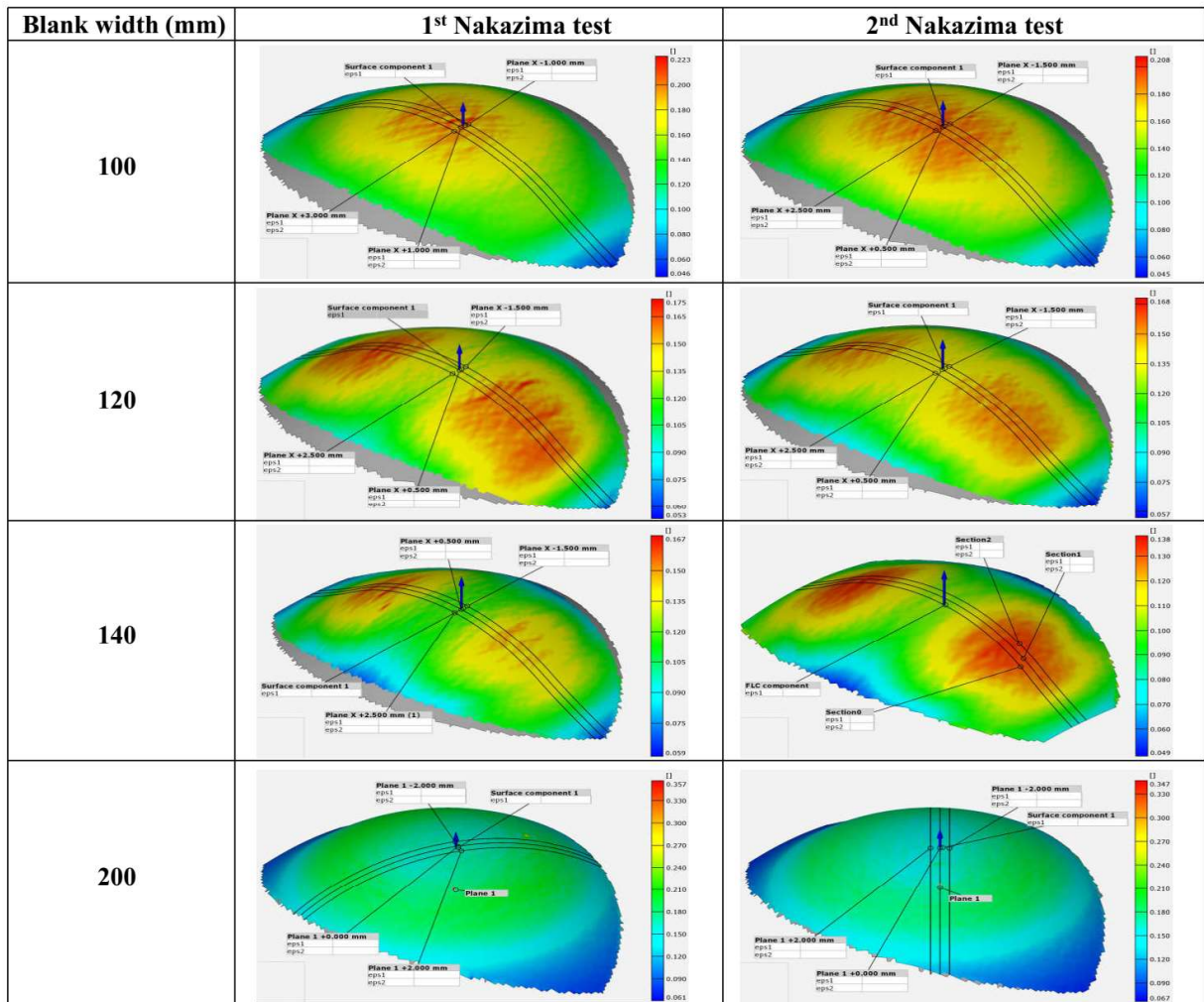


Fig. 3.9 Digital image correlation (DIC) analysis of the specimens with the blank widths of 100~200 mm during the first and second Nakazima experiments.

Fig. 3.10 shows the experimental FLD of ultra-thin FSS sheet under various loading paths. The FLD curve is plotted based on the major and minor strains which were obtained from the DIC analysis as shown in Figs. 3.8 and 3.9. The result shows that the Nakazima test is able to obtain the FLD which is used to evaluate the formability of ultra-thin FSS sheet. It reveals that the lowest forming limit strains are observed at near the plan strain condition while the greatest one is found

in the uniaxial condition. This implies that the majority of fracture in the sheet forming will take place in the plain strain condition.

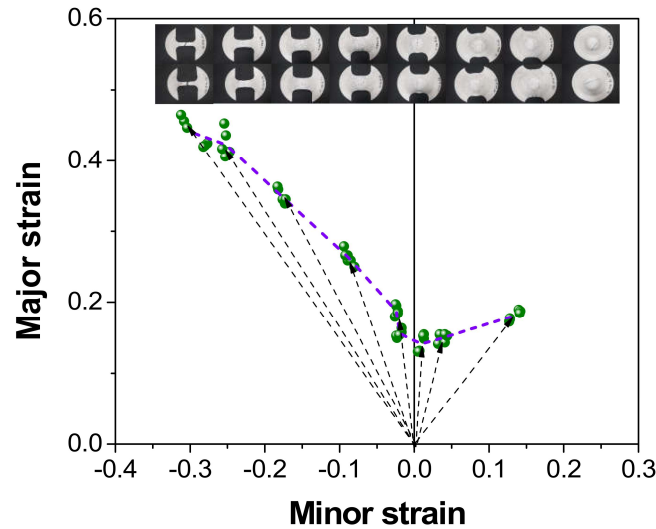


Fig. 3.10 Experimental FLD of ultra-thin FSS sheet by the Nakazima test.

Then, the experimental FLD is used to verify the CPFEM model for investigating the effects of imperfection factor and initial material texture in the following sections, especially the size effect on the formability of ultra-thin steel sheet in Chapter 5.

3.3.2 Effect of imperfection factor and initial texture on the FLD prediction

It should be noted that the calibrated hardening parameters of CPFEM model obtained in chapter 3 was used in this chapter. The coupled CPFEM–MK model was used to predict the FLD of ultra-thin FSS sheet under various loading paths ($-0.5 \leq \rho \leq 1$). Firstly, the forming limit analyses were conducted to investigate the effect of imperfection factor on the FLD prediction. Note that the voxel-typed RVE considering the measured texture was used in this analysis. As shown Fig. 3.11(a), the predicted FLD of ultra-thin FSS sheet under four initial imperfection factors are compared with the Nakazima test results. It is obviously observed that the FLD shifts downward

with the initial imperfection factor f_0 . In the MK model, the initial stress state of the groove region is determined by f_0 under the force equilibrium and strain compatibility conditions. When f_0 becomes smaller, the major strain increment ($d\varepsilon_x^B$) is larger by Eq. (3.4), while the minor strain increment ($d\varepsilon_y^B$) does not change by Eq. (3.5). Thus, the initial stress state of the groove region can be positioned more toward the plane strain ($\rho = 0$) with a smaller initial strain increment ratio [80], responsible for the lower formability. In fact, due to the reduction of groove thickness, the onset of necking localization can occur early, resulting in the decrease of formability. The results show that the imperfection of thickness in the sheet metals has a significant influence on the obtained FLD.

Fig. 3.11(a) reveals that the CPFEM–MK model under the condition of $f_0 = 0.95$ well predicts the forming limit of ultra-thin steel sheet. In order to evaluate the performance of FLD prediction, the following equation is used throughout the present study.

$$Error = \frac{1}{N} \sum_{i=1}^N \left| \frac{\varepsilon_{i,maj}^{exp} - \varepsilon_{i,maj}^{pre}}{\varepsilon_{i,maj}^{exp}} \right| \times 100 \quad (3.46)$$

where $\varepsilon_{i,maj}^{pre}$ and $\varepsilon_{i,maj}^{exp}$ are the predicted and experimental major strains, N is the total number of strain paths ($N = 9$). As indicated in inserted table in Fig. 3.11(a), the estimated error is $\sim 7.2\%$ for the f_0 of 0.95 which shows a good agreement with the experimental FLD.

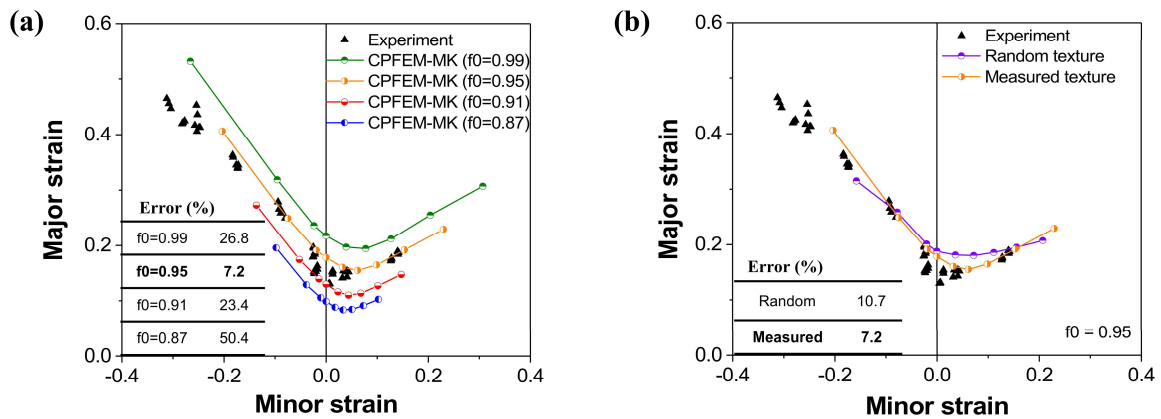


Fig. 3.11 FLD prediction of ultra-thin FSS sheet depending on (a) imperfection factor and (b) initial texture in comparison with experimental measurement.

Furthermore, the CPFEM–MK analyses were performed using initial imperfection factor of 0.95 to study the initial texture effect on the FLD. Normally, the formability of polycrystalline sheet metals is significantly affected by the crystallographic texture of materials. The effects of texture components on the formability of sheet metals has been investigated in the literature [95,96]. In the present study, the effect of random and measured textures on the FLD of ultra-thin FSS sheet are addressed by using the CPFEM–MK model with the voxel-typed RVEs.

Fig. 3.11(b) shows apparently different results in the prediction of FLD depending on the initial texture. For the random texture, it is obviously observed that the left hand-side of FLD can be well captured but it fails in predicting the FLD in the right hand-side. The higher formability for these strain paths ($\rho \geq 0$) may be due to the effect of cube texture component for a random texture [95]. Yoshida et al. [95] suggested that the geometrical hardening effect from the higher work-hardening rate for the cube texture resulted in the higher limit strains. As revealed in the calculated ODF in Chapter 2, the present material primarily exhibits the strong γ -fiber texture. Thus, the forming limit analysis by taking into account the measured texture can well fit the whole experimental FLD

curve as shown in Fig. 3.11(b). In equibiaxial stretching ($\rho = 1$), the predicted limit strains are higher than the experiments. The literature reported that such discrepancy can be caused by the decrease in the sharpness of the yield locus [96,125]. For a quantitative comparison, the measure of error was also calculated using Eq. (3.12) as depicted in Fig. 3.11(b). It suggests that the measured texture should be considered in the forming limit analysis of sheet metals to accurately reproduce the experimental measurement.

3.3.3 Role of geometrical imperfection in the FLD prediction

The evaluation of FLD by the Hill's, Swift's and Hora's NIC models without consideration of geometrical imperfection were studied to assess the role of geometrical imperfection on FLD predictions, as shown in Fig. 3.12. The obtained force and displacement from the CPFE analysis in the outer region of MK model are extracted to calculate the Eqs. (3.7, 3.8, 3.11).

Fig. 3.12 shows a comprehensive comparison of predicted FLD of ultra-thin FSS sheet by different NIC models. It is seen that the Swift's necking criterion fails in the prediction of limit strains with the large discrepancy. While both Hill's and Hora's models well capture the FLD experimental in their respective ranges of application with the reasonably quantitative error, as depicted in Fig. 3.12. Such results of FLD prediction with these NIC models are consonant with the investigation in the literature [126].

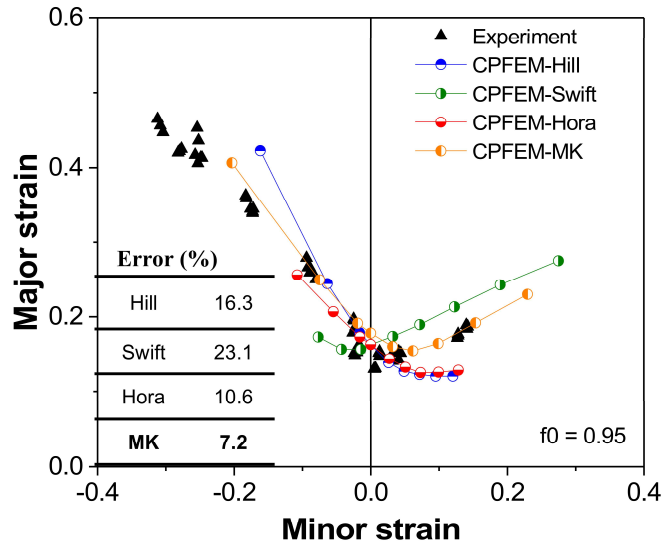


Fig. 3.12 FLD prediction of ultra-thin FSS sheet by different NIC models in comparison with experimental measurement.

In contrary to the NIC models, the MK model by taking into account geometric constraint shows a good capacity in representing the experimental FLD. Normally, the Hill's, Swift's and Hora's NIC models were derived based on the maximum force condition which suggests that the limit strains would be deformation path insensitive with the expression of effective strain. However, it is the path sensitive because the effective strain is expressed in term of strain components and dependence on the deformation mode. Chung et al. [80] reported that the maximum force-based model was not so realistic for addressing the deformation path sensitivity of the sheet forming limit criteria. To explain it, they presented two critical points that the model based on maximum force condition did not involve any geometric constraint and take into account material line rotation due to its Eulerian nature of the formulation. Unlike the maximum force condition-based NIC models, the MK approach is more realistic by imposing geometrical constraint condition, which is satisfied the force equilibrium condition in addition to the consideration of interface line rotation at the imperfection region. In the present study, therefore,

the MK model with assumption of the existing inhomogeneity can fairly well reproduce the entire curve of experimental FLD while NICs cannot. It can be discerned that the geometrical imperfection in the sheet material plays an important role as a fracture criterion in the evaluation of forming limit strains.

3.4. Conclusions

The FLD of ultra-thin FSS bipolar plate for PEM fuel cell was successfully determined by both experimental Nakazima test and theoretical predictions. The CPFEM–MK model using the voxel-typed RVE well reproduced the experimental FLD. It revealed that the initial imperfection factor significantly affected the formability of ultra-thin FSS sheet in which the formability decreased with the imperfection factor. This indicates that it is important to determine the proper imperfection factor in the FLD prediction.

In addition, the formability of ultra-thin FSS sheet was strongly influence by the initial material texture. The results showed that predicted FLD using the measured texture was in good agreement with the experimental measurement compared to the random texture. It implies that for accurately reproducing the experimental FLD, the measured texture should be considered in the forming limit analysis of sheet metals.

Furthermore, the capacity of MK model was comprehensively compared with the different NIC models for the FLD prediction. By consideration of geometrical constraint condition, the MK model well captured the entire of FLD curve while the NIC models could not. It suggests that the geometrical imperfection in the sheet material can be considered as a fracture criterion in the ductile fracture model for simulating the material failure.

CHAPTER 4

SIZE EFFECT ON FORMABILITY OF ULTRA-THIN STEEL SHEET

Ultra-thin sheet metals may show a deviation from the conventional mechanical behavior, so-called size effect, once the thickness of the polycrystalline sheet becomes comparable to the grain size. This chapter investigated the size effect on the formability of a 0.08 mm-thick metallic bipolar plate for proton exchange membrane (PEM) fuel cell by a combined crystal plasticity finite element method–Marciniak-Kuczynski (CPFEM–MK) model and realistic representative volume elements (RVEs). Firstly, the realistic RVEs were generated using a hybrid cellular automata–Monte Carlo (CA–MC) model by considering the measured texture and grain boundary misorientation distribution (GBMD) with a high fidelity. Then, the CPFEM–MK model was successfully validated in comparison with the in-plane tensile test results and the experimental FLD. Secondly, forming limit analyses were carried out using the realistic RVEs with various thickness-to-grain size ratio ($t/d = 2\sim 10$) in order to explore the size effect on the FLD. The stress and strain heterogeneities and stress triaxiality in the surface grains for the RVE with low thickness-to-grain size ratio was discussed in detail.

4.1. Methodology

4.1.1. Experiment

The descriptions of uniaxial tensile and formability tests were described in Chapters 2 and 3, respectively. The results of stress-strain and FLD curves were also used throughout this chapter.

4.1.2. CPFEM simulation

In this study, the developed CPFEM model described in Chapter 2 was used to simulate the uniaxial tensile test. While the predictions of FLD using the realistic RVEs with various thickness-to-grain size ratios were carried out by the combined CPFEM–MK model which was developed in Chapter 3.

4.1.3. A hybrid cellular automata and Monte Carlo model

The cellular automata (CA) and Monte Carlo (MC) models have been extensively used as a tool for precisely reproducing not only the realistic behavior of grain growth [127,128] but also the microstructure and texture evolution during recrystallization of the materials [129,130]. The unique advantages of these micro-mesoscale models are relative simplicity, high computational efficiency and flexibility in simulating different physical phenomena at a microscopic level [131–133], thus the macroscopic behavior of the material can be successfully predicted as the most attractive point to many researchers [134,135]. Here, the capabilities of CA and MC models as well as their coupling effects are important for reconstructing a realistic representative volume element (RVE) of polycrystal grain structure of the material.

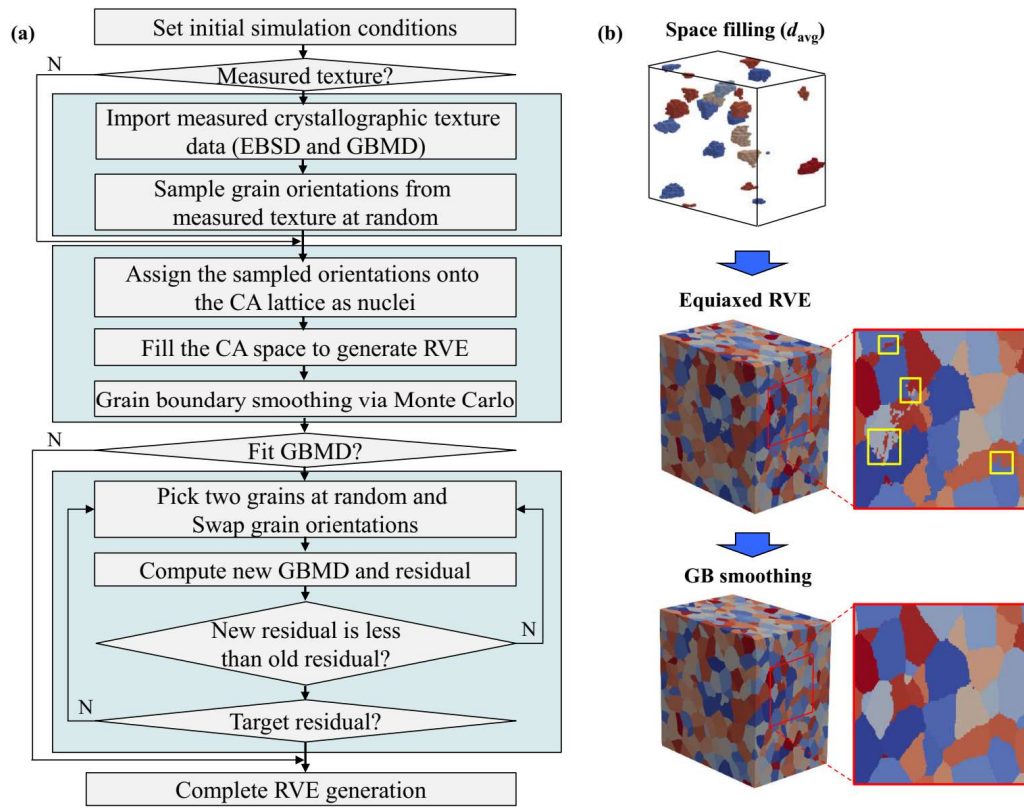


Fig. 4.1 (a) Flowchart of cellular automata–Monte Carlo (CA–MC) hybrid algorithm and (b) schematic of realistic RVE generation.

In this work, a hybrid CA–MC model was developed and used to construct the realistic RVE for investigating the size effect on the FLD. Fig. 4.1(a) shows the flowchart of CA–MC algorithm used for generation of realistic RVE. The measured texture and GBMD obtained from the EBSD measurement were imported as an input for the simulation. At the beginning of simulation, the nucleation sites were randomly selected from the cells to assign the sampled orientations with the measured texture. The Moore neighborhood was accounted for the state switching rule of neighboring cell. The CA simulation proceeded by switching the cells through the local switching probability. After completing space filling of RVE, the MC algorithm was applied to smooth the

grain boundary and accordingly the unrealistic islands as indicated by yellow rectangles in Fig. 4.1(b) were removed by smoothing artificial jagged grain boundary.

The fitting GBMD was performed by randomly picking two grains and swapping their orientations if the residual of grain boundary misorientation distribution was decreased. In order to calculate disorientation, the Euler angles were converted into the orientation matrix. Then the misorientation matrix M was computed from the two neighboring grains, namely grain A and grain B, using the following equation as

$$M = g_A g_B^{-1} \quad (4.1)$$

where g_A and g_B are the orientation matrices for each grain. The rotation angle $\Delta\theta$ could be extracted from the orientation matrix M as follows

$$\Delta\theta = \arccos\left[\frac{\{tr(M) - 1\}}{2}\right] \quad (4.2)$$

The minimum among all the possible 24 crystallographically equivalent misorientations was selected in consideration of cubic crystal symmetry. The process of fitting GBMD was repeated until the target residual was met. The residual R between reconstructed and experimental GBMDs was computed as

$$R = \sum_{i=0}^N \left(F_{\Delta\theta_i}^{\text{exp}} - F_{\Delta\theta_i}^{\text{sim}} \right)^2 \quad (4.3)$$

where $F_{\Delta\theta_i}^{\text{exp}}$ and $F_{\Delta\theta_i}^{\text{sim}}$ define the GBMD of experiment and simulation, respectively. The schematic of realistic RVE generation using the hybrid CA–MC model was given as shown in Fig. 4.1(b).

4.2. Results and discussion

4.2.1. Generation of the realistic RVEs

4.2.1.1. Determining number of elements per grain

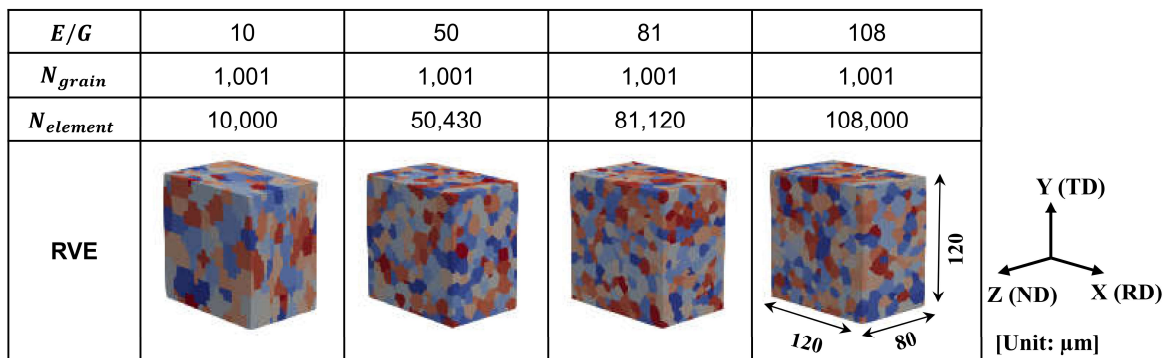


Fig. 4.2 Generation of realistic RVEs with the average grain size of $13 \mu\text{m}$ to determine the minimum number of elements per grain (E/G) used in the CPFEM analysis.

It should be emphasized that the purpose of this chapter is to assess the size effect on the formability of ultra-thin FSS sheet by using the CPFEM–MK approach. In the previous section, the prediction of FLDs were performed using the RVEs with the voxel type. In the reality, however, the microstructure of as-received sheet materials generally exhibits the grain structure with an equiaxed morphology. Therefore, the realistic RVE which shows a fully equiaxed grain microstructure should be considered in the forming limit analysis in addition to the investigation of size effect.

Since the number of elements that represents one grain has a significant effect on the macroscopic response of the materials [136,137], the same number of elements per grain should be used regardless of the t/d ratio. Hence, the CPFEM simulations of uniaxial tension were

conducted to determine the minimum number of elements per grain (E/G). It should be noted that the developed CPFEM model in chapter 2 was used in this analysis. As shown in Fig. 4.2, the realistic RVEs with different number of elements per grain ($E/G = 1\sim 108$) were generated by the hybrid CA–MC model in consideration of the measured texture and GBMD. Note that the RVE with $E/G = 1$ that has a voxel shape was not shown in Fig. 4.2. The average grain size of $13\ \mu\text{m}$ was selected to be identical for all RVEs consisting of 1,001 grains.

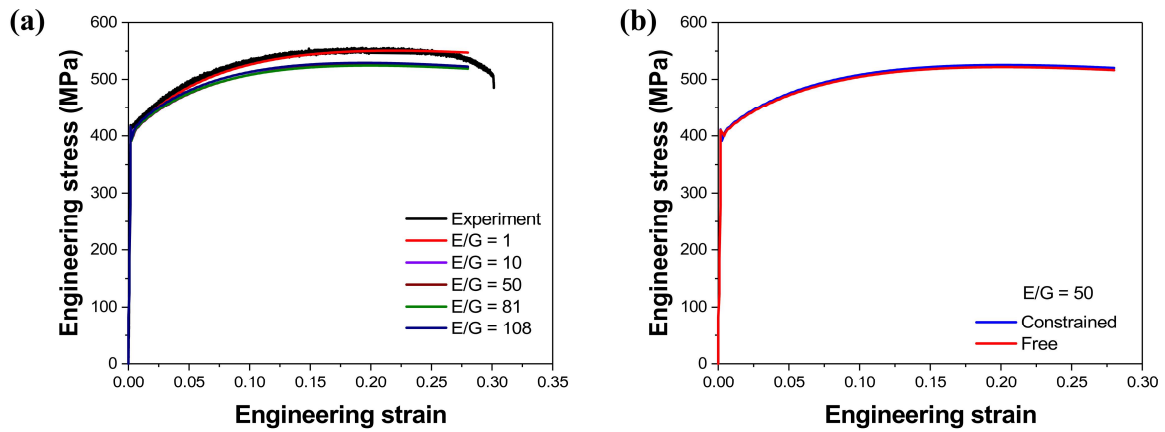


Fig. 4.3 The CPFEM predicted stress-strain curves (a) with various number of elements per grain (E/G) in comparison with the experimental results and (b) with and without constrained surface in Z (ND) direction using $E/G = 50$.

Fig. 4.3(a) shows the predicted stress-strain curves with respect to the number of elements per grain, together with the experimental result. It reveals that the macroscopic response is almost identical as the E/G increases, except for the $E/G = 1$ which leads to a stiffer response in tension. Such results of stress-strain prediction with respect to the E/G are consonant with the investigation in the literature [137]. In order to represent each grain with more realistic microstructure, therefore, the $E/G = 50$ is selected for further CPFEM analysis. In addition, the effect of boundary condition with and without constrained surface, i.e., periodic boundary condition, in the Z (ND) direction

was investigated. Fig.4.3(b) shows a negligible difference in the predicted macroscopic behavior compared between free and constrained surfaces in the Z (ND) direction. Nevertheless, there is a decrease in the flow stress in the RVE with the free surface condition, which is similar to the previous report [62].

4.2.1.2. Generating the realistic RVEs

As shown in Fig. 4.4, four RVEs with different average grain sizes were generated by considering the measured texture and GBMD in order to explore the size effect on the FLD. The thickness of all RVEs is the same with the actual material ($t = 0.08$ mm) and kept constant to avoid the distribution from the other size effect. In the present study, the average grain sizes of RVEs are assumed to be 8, 13, 20 and 40 μm corresponding to the thickness-to-grain size ratios (t/d) of 10, 6, 4 and 2, respectively. The domain size of all RVEs is adjusted to obtain the same number of elements per grain ($E/G = 50$) and number of elements ($N_{\text{element}} = 53,900 \sim 54,760$). As depicted in Fig. 4.4, all RVEs have a sufficient population of grains ($N_{\text{grain}} = 1,074 \sim 1,097$).

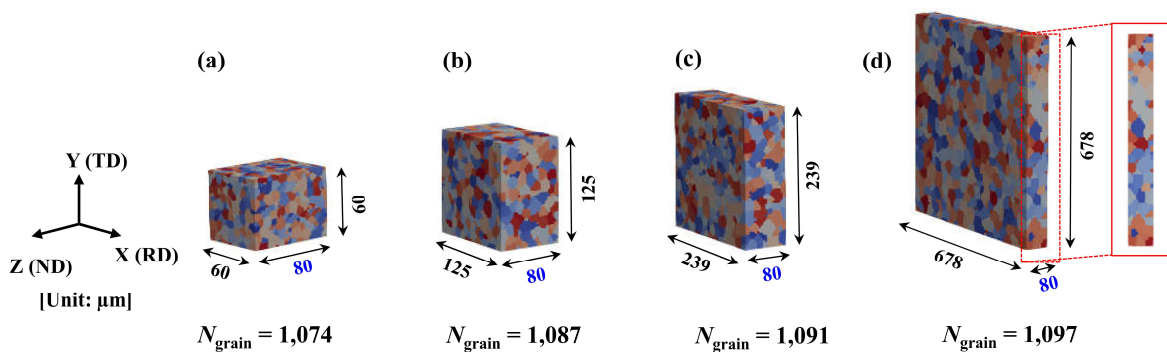


Fig. 4.4 The realistically generated RVEs for FLD prediction with the same number of elements per grain ($E/G = 50$), number of grains ($N_{\text{grain}} = 1,074 \sim 1,097$) and number of elements ($N_{\text{element}} =$

53,900~54,760): (a) $d = 8 \mu\text{m}$, $t/d = 10$; (b) $d = 13 \mu\text{m}$, $t/d = 6$; (c) $d = 20 \mu\text{m}$, $t/d = 4$; (d) $d = 40 \mu\text{m}$, $t/d = 2$. Note that the thickness of $80 \mu\text{m}$ is the same for all RVEs.

Generally, the as-received materials will exhibit strongly heterogenous microstructures in term of grain size and morphology after different heat treatments. It is difficult to deconvolute the effects of grain size and crystallographic orientation on the mechanical behaviors and plastic deformation of the materials. Hence, the same measured crystallographic texture of ultra-thin FSS sheet with the actual average grain size of $13 \mu\text{m}$ was used in the generation of all RVEs. Such assumption facilitates a comprehensive study on the grain size effect without the interference of crystallographic texture effect. As shown in Fig. 4.4, the realistic RVEs with equiaxed grain structure were generated by the hybrid CA–MC model. It reveals an apparent difference in grain size among the RVEs as confirmed in the grain size distribution in Fig. 4.5.

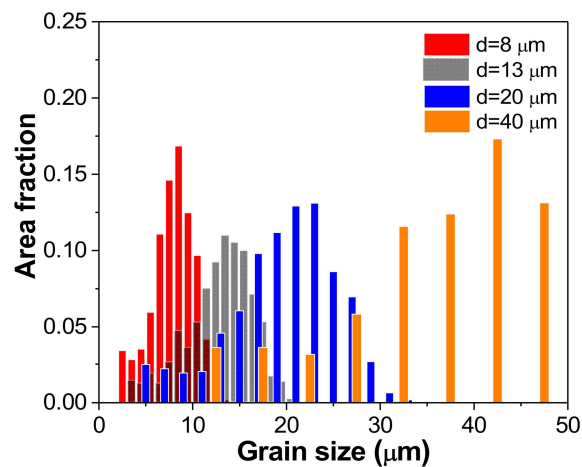


Fig. 4.5 The reconstructions of grain size distribution of the realistic RVEs with different average grain sizes.

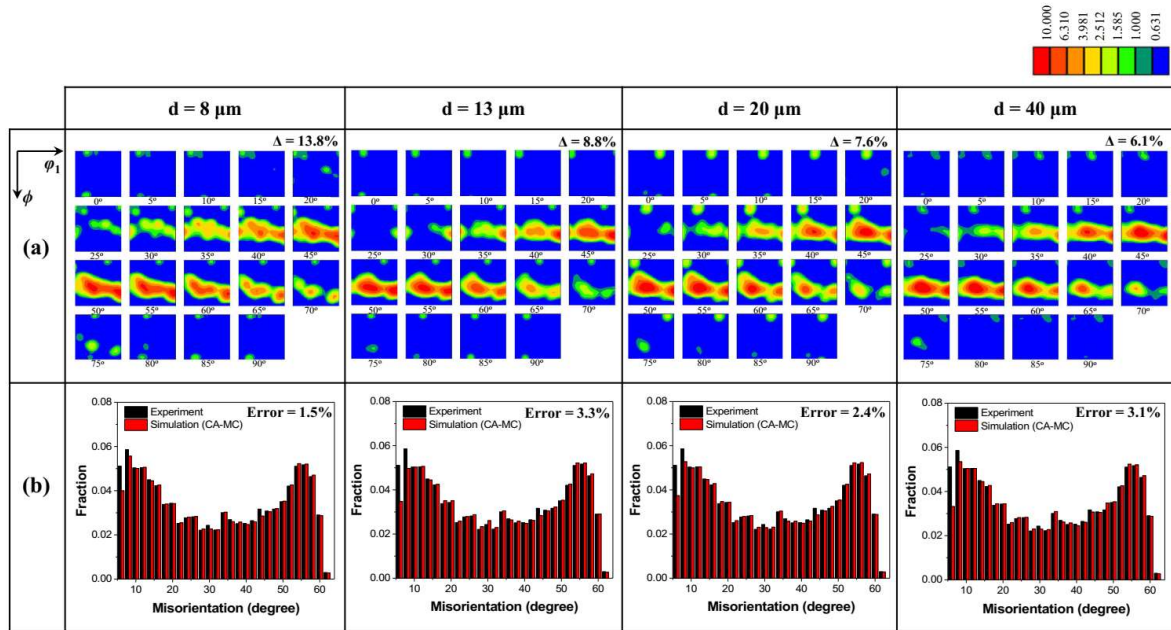


Fig. 4.6 The reconstructions of (a) orientation distribution function (ODF) (Δ represents normalized texture different) and (b) grain boundary misorientation distribution (GBMD) of the realistic RVEs with different average grain sizes.

4.2.1.3. Reconstructing the ODF and GBMD

In order to verify the RVE generation, not only orientation distribution function (ODF) but also grain boundary misorientation distribution (GBMD) were reconstructed from the EBSD data as shown in Fig. 4.6. Fig. 4.6(a) shows the reconstructed ODFs of the realistic RVEs with different average grain sizes. It is clearly seen that the overall texture intensity among the RVEs is relatively similar to that of experiment as shown in Chapter 2. To quantitatively assess the difference between the reconstructed and experimental ODFs, a normalized texture difference is calculated using the following equation as

$$\Delta = \frac{\int_{\text{eulerspace}} [f_{\text{exp}}(g) - f_{\text{sim}}(g)]^2 dg}{\int_{\text{eulerspace}} [f_{\text{exp}}(g)]^2 dg} \quad (4.4)$$

where $f_{\text{exp}}(g)$ and $f_{\text{sim}}(g)$ are the experimental and reconstructed ODFs, respectively, as a function of the Euler space coordinates g . The normalized texture difference amounts 13.8%, 8.8%, 7.6% and 6.1%, which gradually decreases with respect to the increase of average grain size (8~40 μm), respectively. This confirms that these RVEs are able to successfully match the crystallographic texture of the material with the normalized texture difference less than 14%.

Fig. 4.6(b) shows the reconstructed GBMDs of the realistic RVEs with different average grain sizes. Note that the same number of iteration of 500 is used for fitting GBMD of all RVEs. When the average grain size and number of cells are assumed to be constant, the number of grains N is calculated according to the following equation as

$$N = \frac{3}{4\pi} N_{\text{cell}} \left(\frac{2L_{\text{cell}}}{d} \right)^3 \quad (4.5)$$

where d is the average grain size, N_{cell} is the total number of cells and L_{cell} is the length of cell. Note that the fitting GBMD stops when there is no further swaps that decrease the residual of grain boundary misorientation distribution.

As shown in Fig. 4.6(b), both reconstructed and experimental GBMD reveal the similar distributions of misorientation characterized by three distinctive angles against low angles below 15° , high angles around 35° and high angles around 55° . Although there is a little discrepancy in a peak position, the realistic RVEs reasonably well capture the experimental GBMD. As indicated in Fig. 4.6(b), the calculated errors between reconstructed and experimental GBMDs are 1.5%,

3.3%, 2.4% and 3.1% with respect to the different average grain sizes, respectively. This indicates that these RVEs show a good reproduction fidelity of the reconstructed GBMDs with the exceptional error less than 4%. The results of reconstructed grain size distribution, ODF and GBMD in Figs. 4.5–4.6 confirm that the realistic RVEs are successfully generated by considering both the measured texture and GBMD.

4.2.2. Size effect on the formability

4.2.2.1. Size effect on the flow stress

The predicted stress-strain curves of four RVE models with different average grain sizes are shown firstly as depicted in Fig. 4.7(a). It reveals an apparent difference in macroscopic response between different average grain sizes. The result shows that the flow stress of the realistic RVE decreases with the increasing average grain size, indicating the grain size effect. Furthermore, the grain boundary density is estimated, $\rho_{GB} = (N_{\text{grain}} \times A_{\text{grain}})/V$, where N_{grain} is the number of grains, A_{grain} is the sphere area and V is the volume of RVE. As shown in Fig. 4.7(b), the estimated grain boundary density significantly decreases as the average grain size increases. This can indirectly affect the decreased flow stress with the t/d ratio as revealed in Fig. 4.7(a). Zhang et al. [62] also presented that the decreased share of grain boundaries due to the decrease of t/d resulted in the slant shear failure of the coarse grain specimen, consequently, weaken the flow stress. They also found that as the t/d decreased, the fracture mode transformed from a normal tensile failure to a pure shear failure.

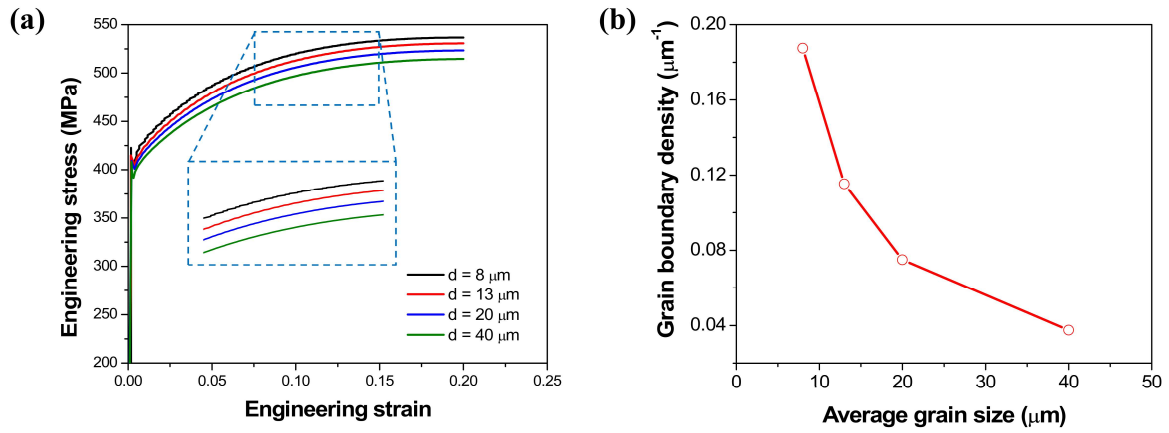


Fig. 4.7 (a) The CPFEM predicted stress-strain curves and (b) the estimated grain boundary density in the four RVE models with different average grain sizes.

4.2.2.2. Size effect on the FLD

Prior to investigating the size effect, the forming limit analysis was performed to verify the CPFEM–MK model by using the realistic RVE. It should be noted that the developed CPFEM–MK model in chapter 4 was used in this analysis. The generated RVE with the actual average grain size of $13 \mu\text{m}$ was used. Fig. 4.8 shows the predicted FLD by the CPFEM–MK model under three different initial imperfection factors f_0 . It reveals that the CPFEM–MK model using the realistic RVE with the f_0 of 0.95 is successfully verified in comparison with the experimental FLD. The performance of the combined CPFEM–MK approach is also confirmed by the reasonable measure of error as indicated in inserted table in Fig. 4.8. Then, the forming limit analyses were carried out using the realistic RVEs with the various thickness-to-grain size ratios ($t/d = 2\sim 10$), as shown in Fig. 4.4, in order to explore the size effect on the FLD.

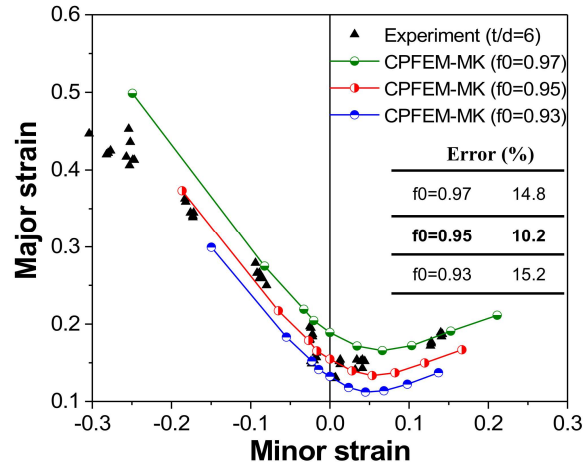


Fig. 4.8 FLD prediction using the realistic RVEs with imperfection factor to verify the CPFEM–MK model in comparison with experimental measurement.

Fig. 4.9 shows the predicted FLD of ultra-thin FSS sheet with different average grain sizes by using the coupled CPFEM–MK model with the realistic RVEs. Note that the periodic boundary condition in Z (ND) direction according to Eq. (4.3) was excluded in this analysis. The number of elements per grain ($E/G = 50$) and the thickness of $80 \mu\text{m}$ is the same for all RVEs. Fig. 4.9 shows that the size effect on the formability is apparently observed. The results show that the coarse-grained RVE with the low thickness-to-grain size ratio ($t/d = 2$) exhibits the lowest forming limit strains, indicating an early onset of fracture failure during the deformation. Zhang et al. [62] also reported that the plastic heterogeneity and fracture failure of metal foils were significantly affected by geometric size effects when the thickness-to-grain size ratio was small ($t/d \leq 3$), while it was less influence with a large $t/d (\geq 6)$. Fig. 4.9 reveals that the formability of ultra-thin steel sheet decreases with the increasing grain size (t/d reduces). This finding is similar to those reported in the literature [64,67,68,138].

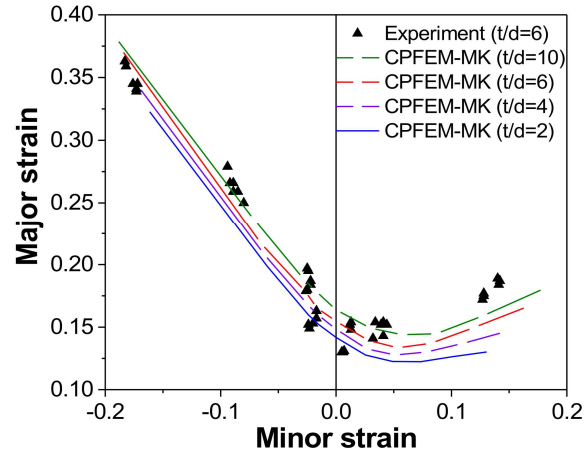


Fig. 4.9 Size effect on formability of ultra-thin FSS sheet using the realistic RVEs with various thickness-to-grain-size ratios (t/d).

4.2.2.3. Correlation of ductile criterion with failure behavior

Previous studies pointed out that the earlier strain localization due to an increasingly inhomogeneous material deformation with the increased grain size is responsible for the decrease of forming limits [67,68]. In the present study, the CPFEM results of accumulated slip, effective strain and effective stress are shown to describe the deformation and failure behaviors which lead to the lower forming limit observed in the coarse-grained RVE ($t/d = 2$). Furthermore, stress triaxiality is also used as one of the most important factors for predicting the material failure of ductile metals as

$$\eta = \int_0^{\bar{\varepsilon}_f} \frac{\sigma_m}{\bar{\sigma}} d\bar{\varepsilon} \quad (4.6)$$

where σ_m is the mean stress.

The ductile damaging indicators in the deformed RVE with fine grain structure ($t/d = 10$) were also calculated to address a comprehensive comparison with the results of the deformed RVE with coarse grain structure ($t/d = 2$). Note that the CPFEM results were obtained from the deformed RVE of the groove region near biaxial tension condition ($\rho = 0.6$) where the minimum major strain and the greatest difference of FLD between the fine and coarse-grained RVEs are observed as shown in Fig. 4.9. Fig. 4.10(a, b) shows the distributions of the accumulated slip and effective strain in both the deformed RVEs at an engineering strain of 0.26. In Fig. 4.10(a), the deformed microstructure of RVE with smaller average grain size ($t/d = 10$) shows more homogeneous distribution of both the accumulated slip and effective strain. In addition, the uniformly distributed strain localization and the shear bands as marked by the black dash lines in Fig. 4.10(a) are observable. In contrast, the deformed microstructure of the coarse-grained RVE ($t/d = 2$) apparently exhibits an inhomogeneous distribution of accumulated slip, as shown in Fig. 4.10(b). The RVE with low t/d reveals that the strain localization which accommodates a majority of plastic deformation, is found at about 45° with respect to the loading direction. The deformed microstructure of the coarse-grained RVE also reveals more significantly inhomogeneous distribution of effective strain. The larger average grain size can result in a noticeably intergranular and intragranular inhomogeneous distributions of the accumulated slip and effective strain.

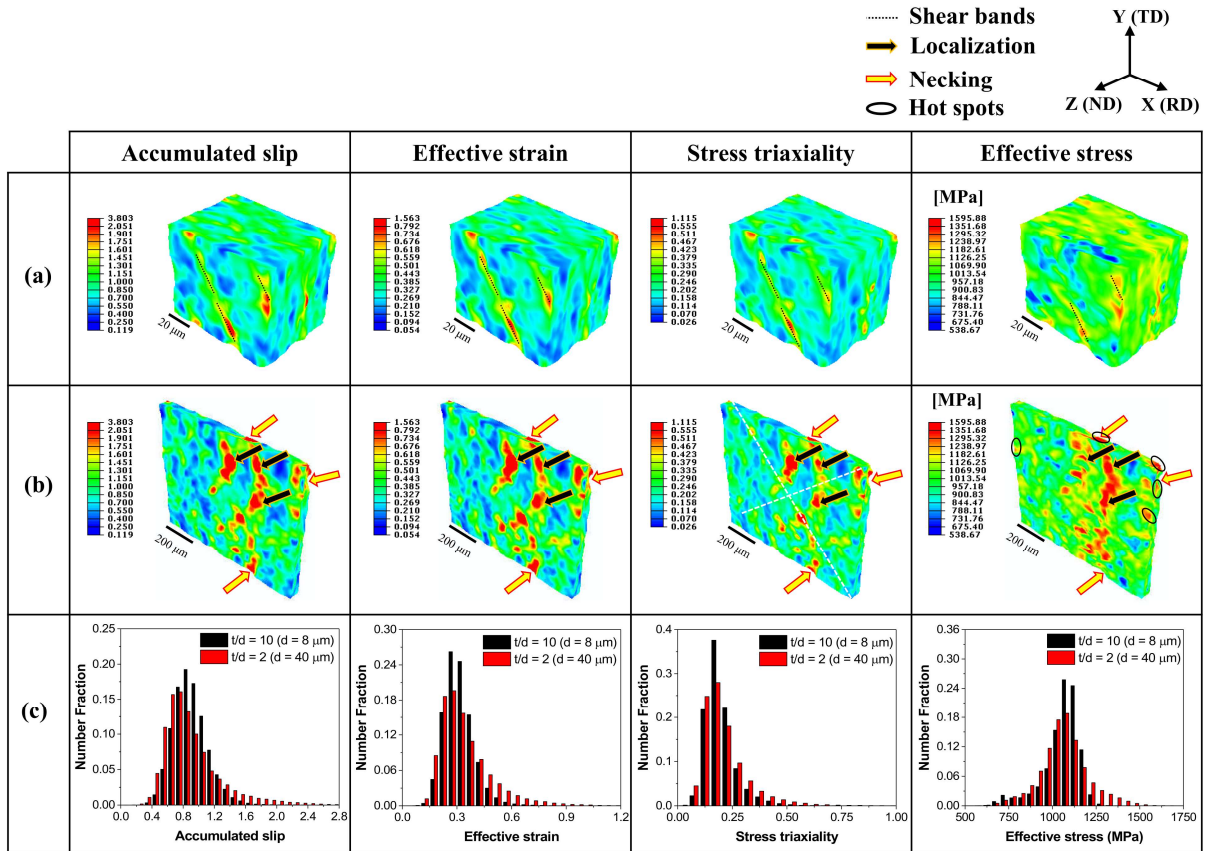


Fig. 4.10 The CPFEM results of the accumulated slip, effective strain, stress triaxiality and effective stress distributions in the deformed RVEs ($e = 0.26$) with the thickness-to-grain size ratios: (a) $t/d = 10$ ($d = 8 \mu\text{m}$) and (b) $t/d = 2$ ($d = 40 \mu\text{m}$), and (c) histograms of these damaging indicators. Note that the thickness of $80 \mu\text{m}$ is the same for both RVEs.

The distributions of stress triaxiality and effective stress in two deformed RVEs are also revealed in Fig. 4.10(a, b). It is found that the coarse-grained RVE with lower t/d clearly exhibits a non-uniform distribution of stress triaxiality as shown in Fig. 4.10(b). The deformed RVE with coarse grain structure ($t/d = 2$) also reveals more inhomogeneous distribution of effective stress than that of the deformed RVE with fine grain structure ($t/d = 10$). As indicated by black arrow in Fig. 4.10(b), the localized deformation is found in the deformed RVE with coarse grain structure ($t/d = 2$), which can coalesce to form shear bands in the microstructure. Furthermore, the deformed

RVE with a small number of grains through the thickness ($t/d = 2$) apparently exhibits an inhomogeneous deformation or necking, as indicated by yellow arrow in Fig. 4.10(b), owing to the mismatch of lattice orientation between the neighboring grains [61]. This necking can be stimulated with the increasing amount of deformation, leading to the earlier failure in the coarse-grained RVE with a small number of grains through the thickness. As shown in Fig. 4.4, there is only two grains distributed through the thickness in the RVE with the largest average grain size ($t/d = 2$). The literature suggested that the forming limits is significantly influenced by the different behaviors of individual grains as there is only one or two grains through the thickness [66]. In fact, with a large number of grains through the thickness with the different orientations, the inner grains are more constrained by the increased fraction of grain boundaries, which makes the deformation of the interior grains more difficult, thus the strengthening effect is induced. In contrast, the surface grains are free from outward normal and shear constraints, and dislocation can easily glide out from the surface as the number of grains through the thickness decreases. Thus, the overall deformation of the coarse-grained RVE is predominantly governed by the surface grains since these surface grains are less constrained and deformed more easily. This results in the more inhomogeneous distributions of accumulated slip, effective strain, stress triaxiality and effective stress as shown in Fig. 4.10(b). The CPFEM results reveal that the shear localizations as the hot spots (marked with black circles in Fig. 4.10(b)) of ductile failure can be easily initiated from the surface towards the interior of the materials. It is seen that the strain localizations and necking in the RVE with only two grains through the thickness ($t/d = 2$) are considered as an evidence of the plastic flow instability induced from the localized deformation of the surface grains. This is responsible for the reduction of forming limit strains in the coarse-grained RVE ($t/d = 2$) as shown

in Fig. 4.9. As a result, the CPFEM analysis with the realistic RVE is of great importance in understanding heterogeneously local strain response.

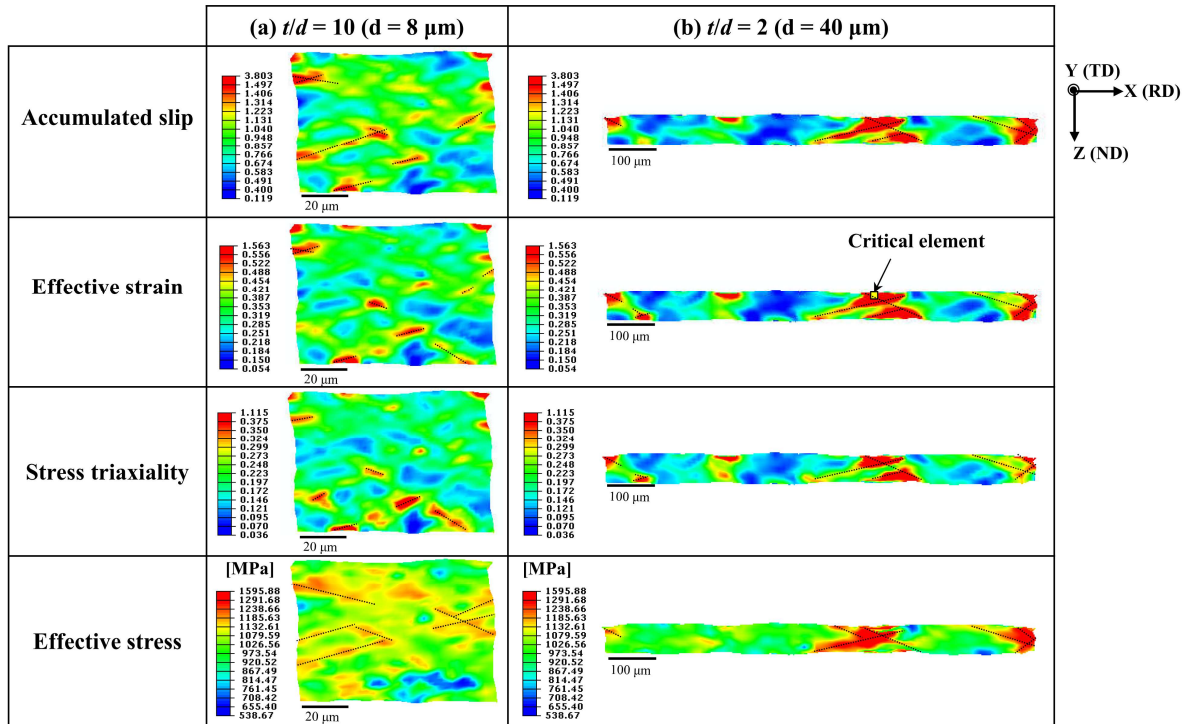


Fig. 4.11 The CPFEM results of the accumulated slip, effective strain, stress triaxiality and effective stress distributions in the RD plane of the deformed RVEs ($e = 0.26$) with the thickness-to-grain size ratios: (a) $t/d = 10$ ($d = 8 \mu\text{m}$) and (b) $t/d = 2$ ($d = 40 \mu\text{m}$). Note that the black dash lines indicate some but not all shear bands. Note that the thickness of $80 \mu\text{m}$ is the same for both RVEs.

Fig. 4.10(c) shows the histograms of the accumulated slip, effective strain, stress triaxiality and effective stress in the deformed RVEs. The range of accumulated slip in the deformed RVE with coarse grain structure ($t/d = 2$) is relatively broader than in the RVE with fine grain structure ($t/d = 10$). The range of effective strain in the deformed RVE with lower t/d is broader and covers the entire range of effective strain in the RVE with larger t/d . As shown in Fig. 4.10(c), the more fractions of high values of accumulated slip and effective strain distributions indicate the earlier

onset of non-uniform and localized strain in the coarse-grained RVE. The distribution of stress triaxiality is similar to that of accumulated slip. The range of effective stress in the coarse-grained RVE is much broader than in the fine-grained RVE. This result indicates that the coarse-grained RVE is subjected to a much higher stress than the fine-grained RVE during the deformation. The distribution of ductile fracture criteria in the ultra-thin steel sheet during the deformation can be significantly affected by the crystallographic orientation of grains.

Fig. 4.11 shows the CPFEM results of the accumulated slip, effective strain, stress triaxiality and effective stress distributions in the TD plane of deformed RVEs at an engineering strain of 0.26. In the fine-grained RVE, there are uniformly distributed strain localizations and some but not all local shear bands as revealed in the distributions of accumulated slip and effective strain in Fig. 4.11(a). Fig. 4.11(a) reveals that the local shear bands are more difficult to propagate for the materials with more than six grains through the thickness [62]. The distribution of stress triaxiality is similar to that of effective strain while the effective stress exhibits a heterogeneous distribution with a coalescence of localizations to form the shear bands as found in the deformed microstructure of RVE with larger t/d . Fig. 4.11(a) also shows that the fine-grained RVE reveals the distribution of strain hot spots in both the surfaces and the interior. For the coarse-grained RVE, however, the strain hot spots distribute mainly in the surfaces as depicted in Fig. 4.11(b). The surface strain hot spots can act as the geometrical imperfection where the stress will further concentrate after surface micro-cracks initiate, and consequently accelerating the failure. Furthermore, the RVE with $t/d = 2$ exhibits apparently the through-thickness shear bands, which play an important role in the material failure during the deformation. Indeed, the shear bands can easily propagate due to the less constraint of surface grains as the number of grains through the thickness decreases.

Fig. 4.12 shows the correlation between stress triaxiality with the accumulated slip, effective strain and normalized effective stress at a critical element as a hot spot of ductile failure in the deformed RVE with coarse grain structure ($t/d = 2$). Note that the effective stress was normalized by the yield strength of FSS sheet. It is found that the stress triaxiality shows a proportional relationship which increases with the increase of the accumulated slip, effective strain and normalized effective stress. The increase of stress triaxiality is attributed to the onset of inhomogeneous deformation or necking, which leads to the reduction of fracture limit strains. As the necking occurs, both the accumulated slip, effective strain and normalized effective stress likely become saturation, resulting in the decrease of stress triaxiality at the end of deformation process.

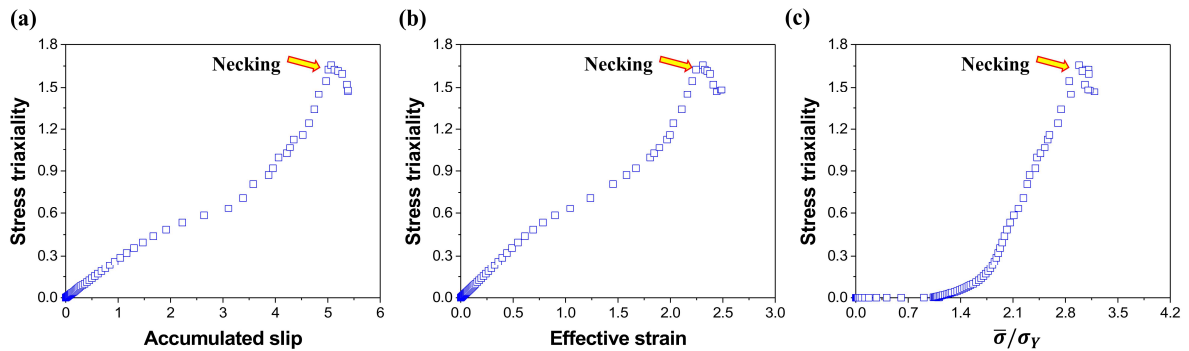


Fig. 4.12 Correlated stress triaxiality with (a) accumulated slip, (b) effective strain and (c) normalized effective stress ($\bar{\sigma}/\sigma_Y$) in the deformed RVE with coarse grain ($t/d = 2$). Note that the results were obtained at a critical element as indicated by a small yellow rectangular in Fig. 4.11(b).

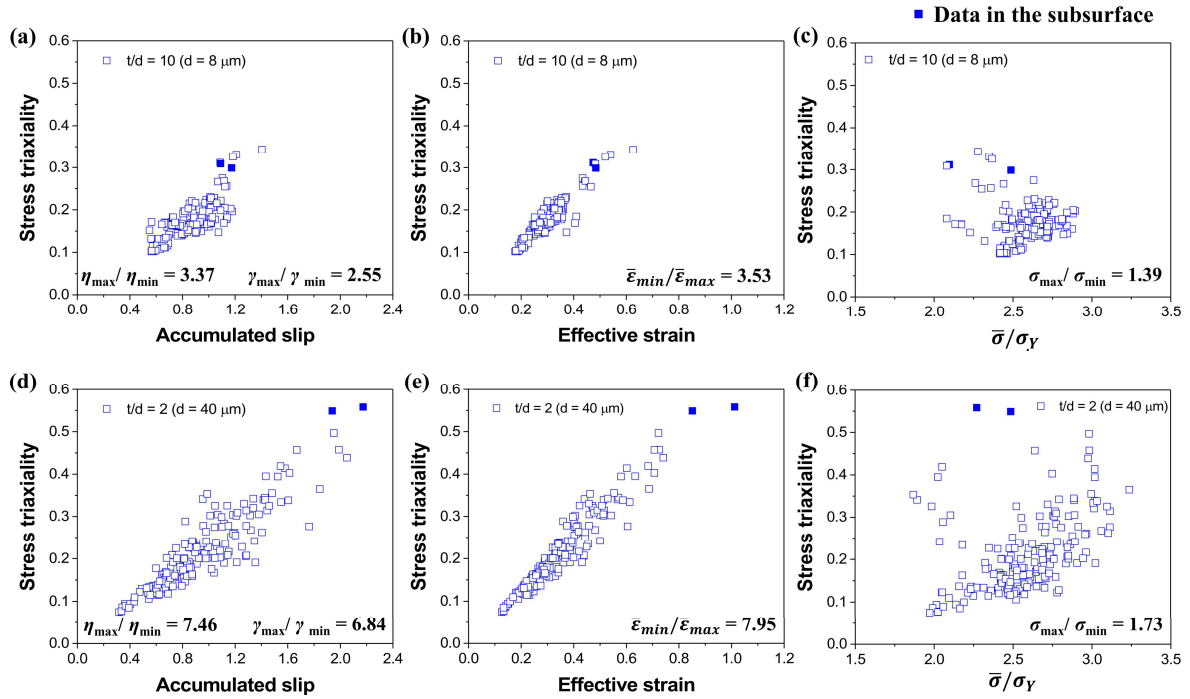


Fig. 4.13 Correlated stress triaxiality (η) with the accumulated slip (γ represent accumulated shear strain), effective strain and normalized effective stress ($\bar{\sigma}/\sigma_Y$) in the deformed RVEs ($e = 0.26$) with thickness-to-grain size ratios: (a–c) $t/d = 10$ ($d = 8 \mu\text{m}$) and (d–f) $t/d = 2$ ($d = 40 \mu\text{m}$). Note that the results were obtained along the two representative white dash lines as indicated in Fig. 4.10(b).

Furthermore, Fig. 4.13 shows the correlated stress triaxiality with the accumulated slip, effective strain and normalized effective stress along the two representative white dash lines as illustrated in Fig. 4.10(b). Fig. 4.13(a) shows a negligible difference in stress triaxiality distribution along the thickness direction in the fine-grained RVE ($t/d = 10$). It is seen that the stress triaxiality is independent on the accumulated slip, effective strain and normalized effective stress. In contrast, as shown in Fig. 4.13(b), the coarse-grained RVE ($t/d = 2$) exhibits a significant distribution of stress triaxiality with the highly relative difference between the maximum and minimum values of $\sim 87\%$. The RVE with $t/d = 2$ shows higher maximum-to-minimum ratios, more than two times for

both the stress triaxiality, accumulated slip and effective strain. It reveals a well explicit relationship between stress triaxiality with the other ductile damaging indicators. Accordingly, the stress triaxiality noticeably increases with the accumulated slip, effective strain and normalized effective stress.

As shown in Fig. 4.13(b), the stress triaxiality in the RVE with coarse grain structure shows a strong dependence on the accumulated slip, effective strain and normalized effective stress. It reveals that the coarse-grained RVE exhibits higher and broader range of stress triaxiality in addition to the accumulated slip, effective strain and normalized effective stress with more fractions of high values. Moreover, it is found that the highest stress triaxiality is observed in the surface grains where the localized deformation can easily take place, resulting in the earlier premature necking and failure. The high stress triaxiality facilitates the acceleration of void growth [139], consequently the fracture strain is decreased which is consistent with the significant reduction in forming limit strains in the RVE with low t/d .

4.3. Conclusions

This chapter investigated the size effect on the formability of ultra-thin ferritic stainless steel (FSS) bipolar plate for PEM fuel cell using crystal plasticity finite element method (CPFEM) in conjunction with Marciniak-Kuczynski (MK) model. The hybrid cellular automata–Monte Carlo (CA–MC) model was developed for generation of the realistic RVEs considering the measured texture and grain boundary misorientation distribution (GBMD). The forming limit analyses were performed using the RVEs with various thickness-to-grain size ratios ($t/d = 2\sim 10$). The following conclusions were drawn.

- (i) The realistic RVEs with various t/d (2~10) were successfully generated by considering the measured texture and GBMD using the hybrid CA–MC model. The reconstructions of ODF and GBMD showed a good reproduction fidelity of experimental measurements of ultra-thin FSS sheet.
- (ii) By comparing the stress-strain curves with the experimental result, the minimum number of elements per grain ($E/G = 50$) was determined, which could represent each grain with more realistic microstructure. In addition, the difference between effect of free and constrained surfaces in the normal direction on the predicted macroscopic behavior was negligible.
- (iii) The CPFEM simulations of uniaxial tensile test using the realistic RVEs with various t/d revealed an apparent difference in macroscopic response between different average grain sizes. The result showed that the flow stress of the realistic RVE decreased with the increasing average grain size, indicating the grain size effect. Furthermore, the estimated grain boundary density significantly decreased as the average grain size increased. This could indirectly affect the decreased flow stress with the t/d ratio.
- (iv) The predicted FLD by CPFEM model using the realistic RVEs was verified with the experimental FLD with the imperfection factors. It revealed that the predicted FLD with the imperfection factor of 0.95 was in good agreement with the experimental FLD of ultra-thin FSS sheet.
- (v) The CPFEM–MK analysis using the realistic RVEs revealed a significant size effect on the formability of ultra-thin FSS sheet. It revealed that the formability decreased with the increasing grain size (t/d reduced).

- (vi) It revealed that the combined effects of geometry feature (thickness) and grain size resulted in the size-dependent forming limit of ultra-thin FSS sheet. As the thickness-to-grain size ratio decreased, the overall deformation was predominantly governed by the surface grains since these surface grains were less constrained and deformed more easily. This played an important role in the size effect, leading to the increased stress and strain heterogeneities in the ultra-thin sheet material with a few grains through the thickness.
- (vii) The coarse-grained RVE with low t/d showed a primary distribution of strain hot spots in the surfaces that could act as the geometrical imperfection to accelerate the failure after surface micro-cracks initiated. In addition, the through-thickness shear bands due to the less constraint of surface grains were apparently observed in the coarse-grained RVE with low thickness-to-grain size ratio, which played an important role in the material failure during the deformation.
- (viii) Furthermore, the surface grains exhibited the high stress triaxiality as a consequence of the localized deformation and premature necking in the coarse-grained RVE. This attributed the decrease of forming limit strains to the early plastic flow instability in the RVE with low t/d .

CHAPTER 5

FREE SURFACE ROUGHENING EFFECT ON THE FORMABILITY OF ULTRA-THIN STEEL SHEET

This chapter investigated the effect of free surface roughening on the micromechanical deformation and failure behavior of ultra-thin ferritic stainless steel (FSS) sheet using in-situ electron backscatter diffraction (EBSD) and crystal plasticity finite element method (CPFEM). The microstructural evolution during uniaxial tension was monitored by the in-situ EBSD technique. Then the initial microstructure was directly mapped onto the finite element mesh in the CPFEM simulations. The CPFEM predictions of stress/strain heterogeneity and the local hot spots of the ductile fracture initiation were compared with the in-situ EBSD measurements. Furthermore, the effect of free surface on the inhomogeneous deformation and necking behavior of ultra-thin FSS sheet was discussed in terms of surface roughness and thickness uniformity parameter.

5.1. Methodology

5.1.1. In-situ tensile test with a miniaturized specimen

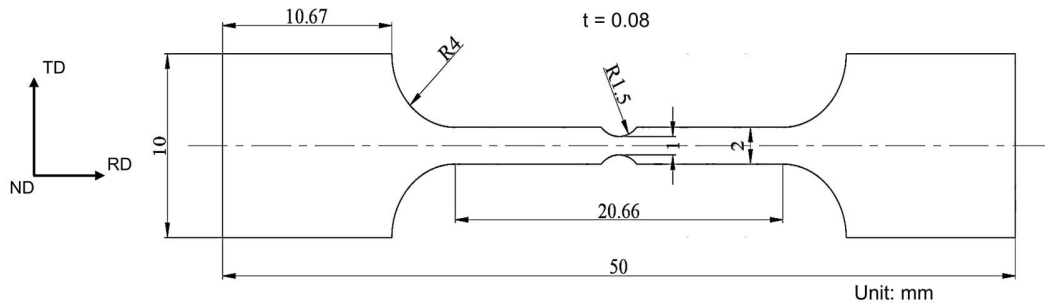


Fig. 5.1 Schematic of miniaturized tensile specimen with the notched gauge for in-situ tensile test.

The miniaturized tensile specimen with the groove in the gauge region was prepared for the in-situ tensile test. Fig. 5.1 shows the detailed dimensions of the miniaturized tensile specimen. The FSS sheet with the thickness of 0.08 mm was used to fabricate the miniaturized tensile specimen using the electric discharge machine. Then the specimen was polished by colloidal silica suspension to improve the surface quality of the specimen for in-situ EBSD measurement.

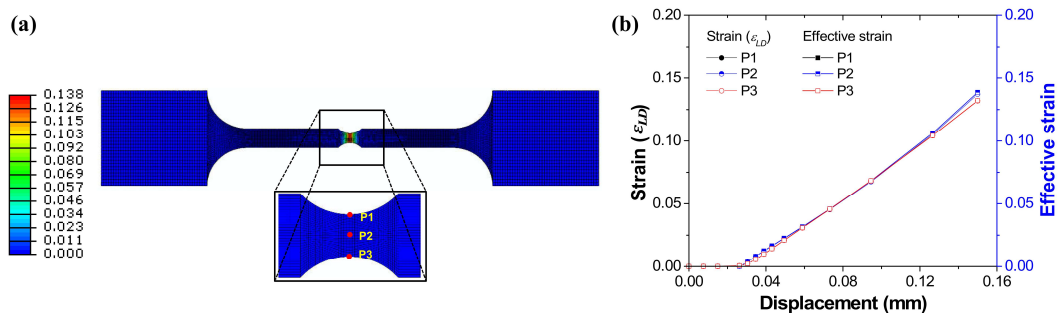


Fig. 5.2 (a) Contour plot of maximum principal strain distribution in the miniaturized tensile specimen and (b) correlation between strains and applied displacement determined from the isotropic elasto-plastic finite element analysis.

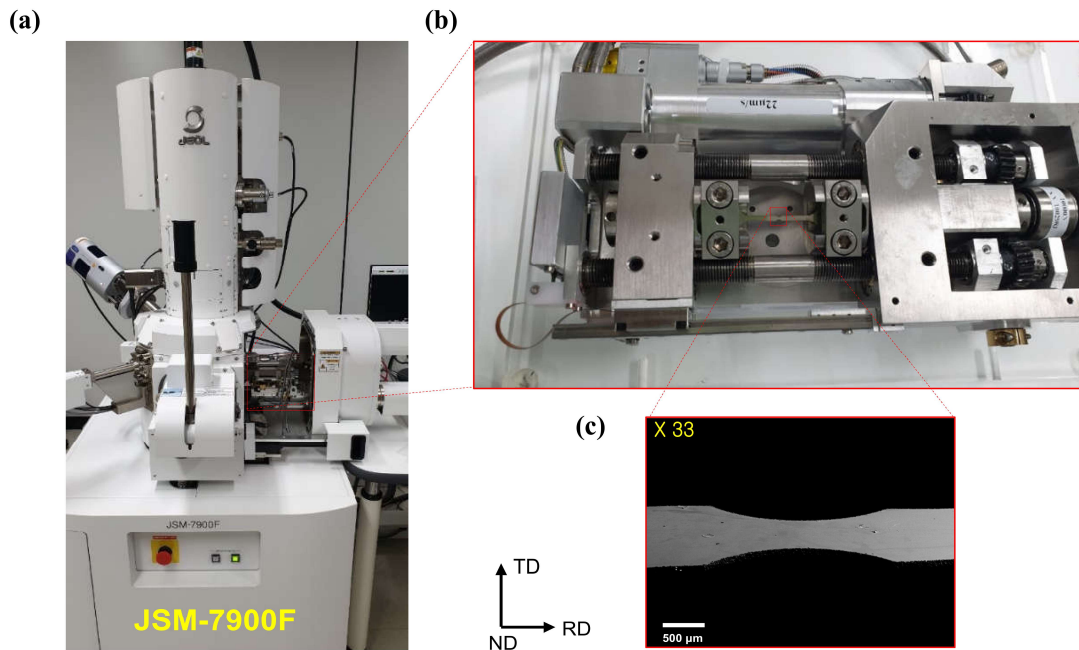


Fig. 5.3 Illustrations of (a) JSM-7900F instrument, (b) in-situ EBSD device and (c) enlarged figure of grooved gauge part in the miniaturized tensile specimen.

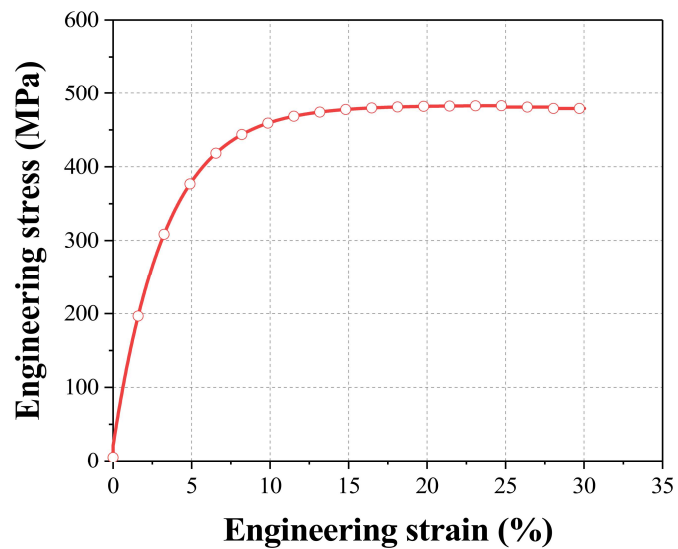


Fig. 5.4 Stress-strain curve during in-situ tensile test.

Prior to conducting the in-situ tensile test, the isotropic elasto-plastic finite element analysis were performed to observe the strain distribution in the miniaturized tensile specimen. As shown

in Fig. 5.2(a), the maximum principal strain was mainly distributed in the grooved gauge region in the miniaturized specimen. The maximum principal and von Mises effective strains at three given points (P1, P2, P3) were observed as shown in Fig. 5.2(b). It revealed the change of strains as a function of the applied displacement. When the effective strain was accumulated to the critical value of approximately 0.15, it was assumed that the ductile fracture occurred in the grooved gauge region of the miniaturized tensile specimen.

The in-situ tensile test was performed using the high-performance field emission scanning electron microscope (FE-SEM, JSM-7900F as shown in Fig. 5.3. The microstructural evolutions during the deformation were monitored and examined in the groove gauge region of the miniaturized tensile specimen. The in-situ EBSD observation were conducted under an accelerating voltage of 20 V, acquisition speed of 31.86 Hz and a specimen tilt of 70°. The scanned area was approximately 80 μm x 60 μm with the step size of 0.8 μm . The engineering stress-strain curve during in-situ tensile test was measured until the engineering strain of 30% as shown in Fig. 5.4.

5.1.2. Microstructural characterization

The surface morphology and boundary densities of the ultra-thin steel sheet during uniaxial tension was characterized by the scanning electron microscope (SEM) and boundary maps, respectively. The inverse pole figure (IPF) map was used to characterize the crystallographic orientation and grain size of the material. The average KAM, a measure of orientation spread, is the misorientation between the average orientation and the neighboring orientations in the kernel neighborhood, which includes the third nearest orientations. Note that only misorientation angles

lower than 5° were considered in the calculation. In addition, the geometrically necessary dislocation (GND) density map was compiled to characterize the evolution of dislocation densities during uniaxial tension. The microstructural features were characterized at the engineering strains of 2%, 5%, 10% and 30%.

5.1.3. Micromechanical simulation

Micromechanical behaviors of ultra-thin FSS sheet during uniaxial tensile test were simulated using the CPFEM. A more detailed description of CPFEM model can be found in Chapter 2.

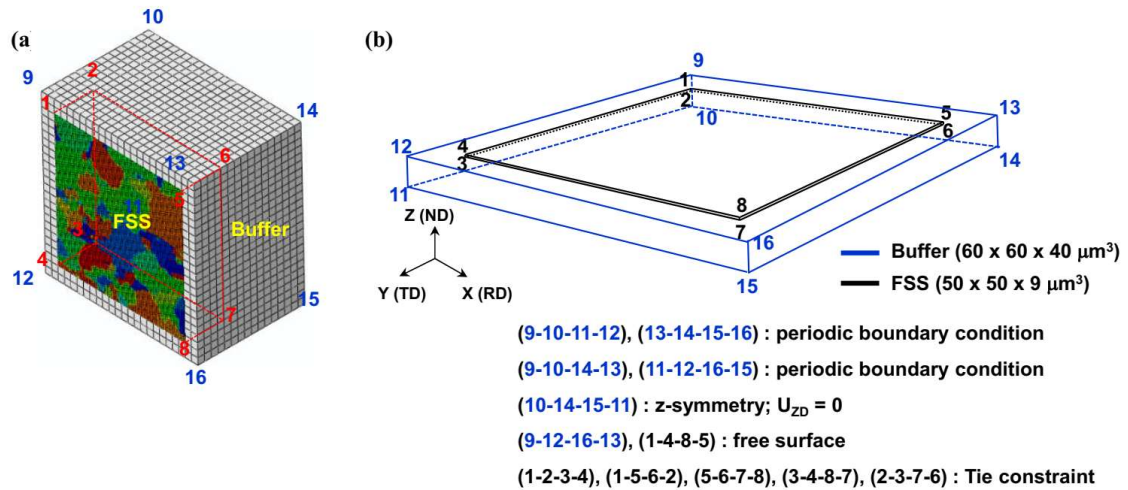


Fig. 5.5 (a) RVE model consisting of the buffer and FSS with microstructure mapping and (b) prescribed boundary conditions.

Fig. 5.5(a) shows the microstructure-based RVE for investigating the effect of microstructural features on the micromechanical deformation and failure behaviors of ultra-thin FSS sheet during uniaxial tension. The RVE consists of the ferritic stainless steel (FSS) and buffer regions. The dimensions of buffer are $60 \times 60 \times 40 \mu\text{m}^3$. For the sake of computational cost, the buffer was

meshed with 7,616 elements (C3D8R, 8-node solid element with reduced integration). The FSS with dimensions of $50 \times 50 \times 9 \mu\text{m}^3$ composed of 108,900 elements. The initial microstructure of the ultra-thin steel sheet obtained from the in-situ EBSD measurement was directly mapped onto the finite element mesh as shown in Fig. 5.5(a). The periodic boundary conditions (PBCs) for a uniaxial tension of $e = 30$ was applied to the four planes of the buffer while the tie constraints were applied to the five plane of the FSS, as shown in Fig. 5.5(b). For the plane in the Z (ND) direction, the symmetric condition was applied to the bottom plane of the buffer while both the top ones of the buffer and FSS were free from outward normal and shear constraints. The von Mises plasticity properties were assigned to the buffer while the FSS was simulated with the rate-dependent constitutive crystal plasticity equations employed in the commercial finite element program Abaqus Standard via a user material subroutine, UMAT.

5.3. Results and discussion

5.3.1. In-situ EBSD microstructure

Fig. 5.6 shows the microstructural observation of ultra-thin steel sheet during in-situ tensile test. The microstructural changes at different stages of deformation were characterized by the SEM, boundary, IPF, KAM and GND density maps. Fig. 5.6(a) shows the initial microstructure observed prior to the in-situ EBSD measurement without strain. The initial surface roughness of the specimen can be observed in the SEM map, while the grain boundary map reveals the low angle grain boundaries (LAGBs) with misorientations less than 5° were surrounded by the high angle grain boundaries (HAGBs) with misorientation greater than 15° in the microstructure of the specimen. As revealed in the IPF map, the ultra-thin steel sheet shows primarily equiaxed grain

structure with the average grain size of 8.76 μm . It obviously shows the homogeneous KAM distribution with a negligible intragranular orientation spread. In addition, the GND density map reveals the similar distribution with a low dislocation density near the grain boundaries.

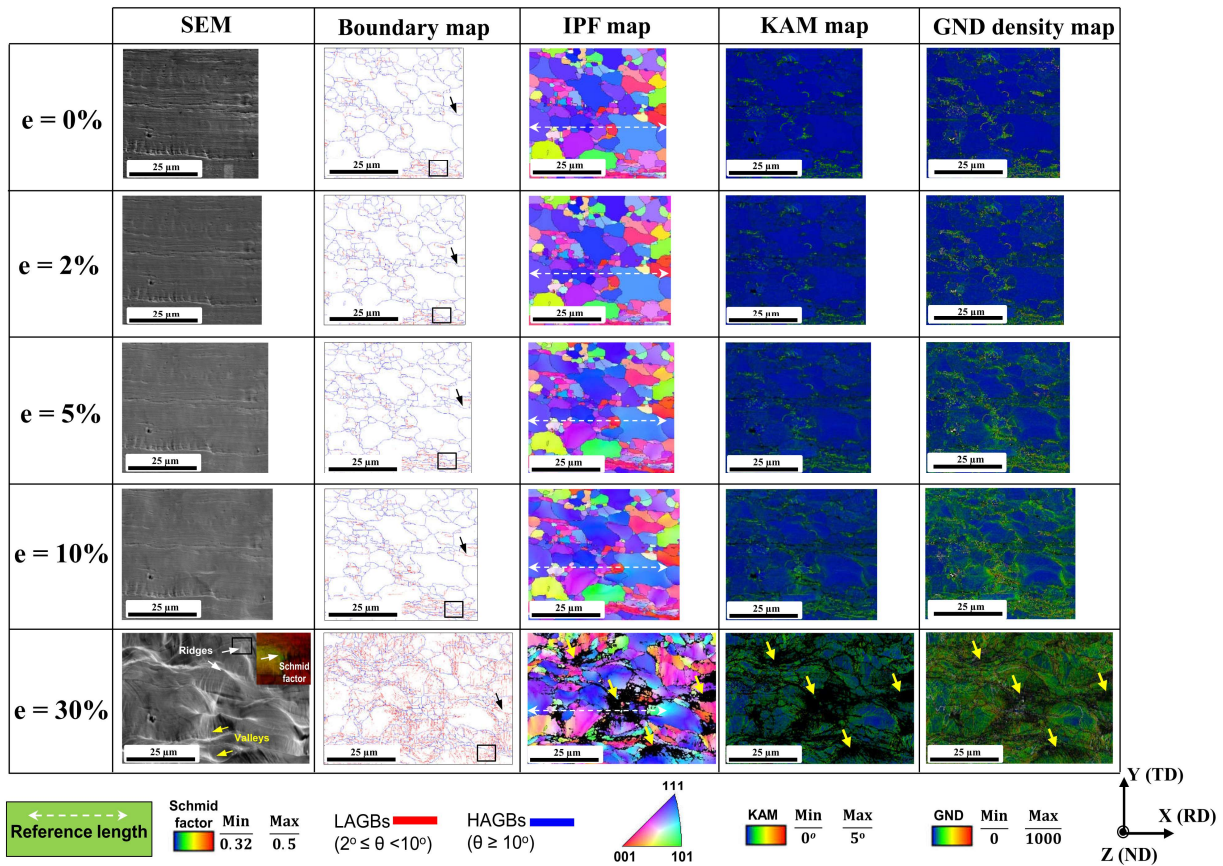


Fig. 5.6 SEM, boundary, IPF, KAM and GND density maps of undeformed and deformed microstructures of in-situ tensile specimen at different engineering strain levels: (a) $e = 0$, (b) $e = 2\%$, (c) $e = 5\%$, (d) $e = 10\%$ and (e) $e = 30\%$.

Figs. 5.6(b-d) show the deformed microstructure of the specimen evolution with strain levels of 0.02, 0.05 and 0.1. It reveals a change in the surface morphology of specimen after deformation as shown in the SEM maps. The black square as inserted in the boundary maps indicates the deformation process of the grain boundary with strain. As the deformation proceeded, these grain

boundaries partly transformed from HAGB to LAGB. It can be obviously seen by the grain indicated by the back arrow. As the strain increased to 0.1, this grain shows a partial transformation from HAGB to LAGB. The IPF maps show that the grains were apparently elongated along the tensile axis as indicated by the reference length. The evolution of dislocation density of the ultra-thin steel sheet under the deformation was quantitatively characterized by the KAM and GND maps [140–142]. Figs. 5.6(b-d) show the KAM and corresponding GND maps at different strains. The color index represents the magnitude of KAM in degree with the lowest value ($0-1^\circ$) in blue and the highest value ($4-5^\circ$) in red. The different dislocation densities are represented by the different colors in the GND maps. The KAM maps reveals the gradually increase in the KAM values with the increasing strains as indicated by the continuous increase in the green and yellow areas. This is also observed in the GND maps, implying the moderate increase in the dislocation density.

Fig. 5.6(e) shows the deformed microstructure of the specimen at high strain level of 0.3. An apparent surface topography is observed in the SEM map. It reveals the considerably inhomogeneous distributions with the ridges and valleys due to the roughness of the sample surface, leading to the localization. The ridges on the sample surface correspond with the grains which hardly deforms. This can be well explained by the low Schmid factor as indicated by the inserted image in the SEM map. In contrast, the grains with high Schmid factor can be deformed easily, resulting in the valleys on the sample surface. The literature reported that the surface roughness can be accompanied due to the difference in the Schmid factor of neighboring grains [143,144]. The boundary map shows an extensive LAGBs formed in the microstructure of the specimen at high strain. It can be seen that the HAGBs in the grains indicated by the black square completely transformed to the LAGBs. These transformations contribute to the increase in fractions of LAGBs

as the deformation increased. The results show that deformation twinning is unobservable, indicating that the deformation is predominantly attributed to the dislocation slip only. The KAM and GND maps show a considerable increase in the KAM value and dislocation densities. It reveals that the increased in the local misorientation and dislocations are inhomogeneous distributions which primarily distribute near grain and sub-grain boundaries. This indicates that the plastic deformation will take place at these grain and sub-grain boundaries, leading to the localized deformation. In addition, the formation process of LAGBs can be attributed to the evolution of KAM value and GNDs [140].

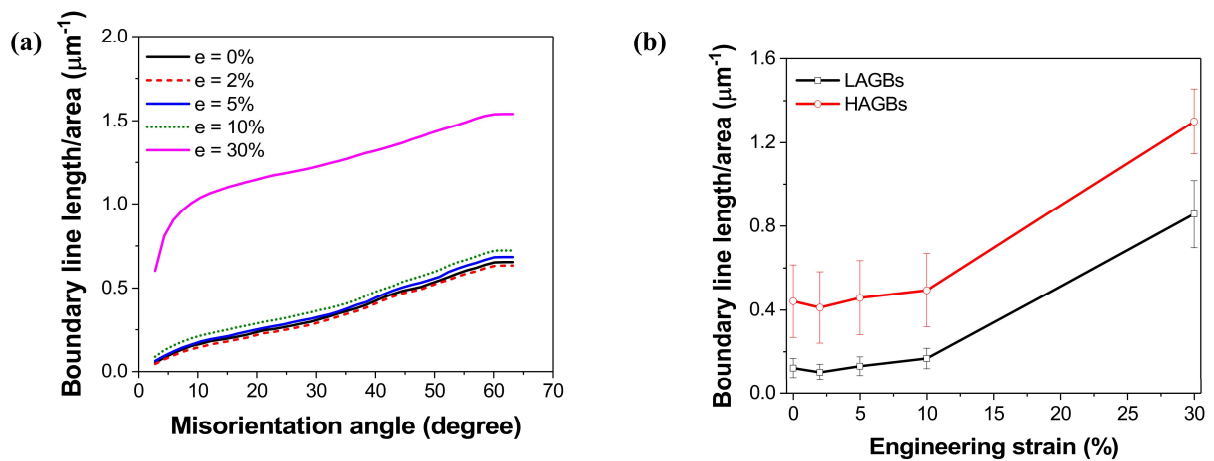


Fig. 5.7 (a) Evolutions of boundary density with misorientation angle and (b) boundary density for LAGBs and HAGBs with the strains.

Fig. 5.7(a) shows the evolution of the boundary density with misorientation angle under different strains. Note that the boundary density is estimated as the ratio of boundary line length to the indexed area. For the strains between 0.1 and 0.02, the boundary density linearly increases with the misorientation angle. As the strain increases to 0.3, however, the boundary density non-linearly increases with the strong increase for the misorientation in range $2\text{--}10^\circ$ followed by the linear increase for the misorientation greater than 10° . Compared the strains between 0.1 and 0.02,

there is negligible difference in the boundary density, which is consistent with the results obtained by the boundary map in Figs. 5.6(b-d). With the increasing strain to 0.3, however, the boundary density significantly increases due to the formation of deformation-induced boundaries. Fig. 6.7(b) shows the evolution of boundary density for LAGBs and HAGBs with the strains. The HAGBs shows higher boundary density than that in the LAGBs. The results show that the boundary density follows an almost linear increase for both LAGBs and HAGBs as the strain increases. A noticeable increase in the boundary density is observed at the high strain of 0.3. Fig. 5.7 shows that changes in the microstructure of specimen under the deformation are quantitatively characterized by using the boundary density.

5.3.2. CPFEM simulation of micromechanical deformation

The CPFEM simulation was performed using the microstructure-based RVE with the EBSD directly mapping (Fig. 6.5(a)) to study the micromechanical deformation and failure behavior of ultra-thin steel sheet during uniaxial tension. Note that the calibrated hardening parameters in Chapter 2 were also used in this Chapter. In order to evaluate the material failure, the damaging indicators of the accumulated slip, effective strain and effective stress was used. Furthermore, the stress triaxiality (Eq. 4.6) was also used to predict the failure behavior of the material.

Fig. 5.8(a) shows the CPFEM results of the accumulated slip, effective strain, effective stress and stress triaxiality distributions in the deformed RVE without buffer at an engineering strain of 0.3. The deformed RVE exhibits an inhomogeneous distributions of accumulated slip and effective strain. It is seen that the strain localization is found at about 45° with respect to the loading direction. This strain localization can accommodate a majority of plastic deformation. It reveals that both the

accumulated slip and effective strain results show a similar localized deformation as the hot spots of the ductile fracture at high strain level of 0.3, as indicated by the red rectangular. It is found that the localized deformation primary distributes in the surface grains which are free from any outward normal and shear constraints. Thus, the deformation take places easily, leading to the increased strain heterogeneity.

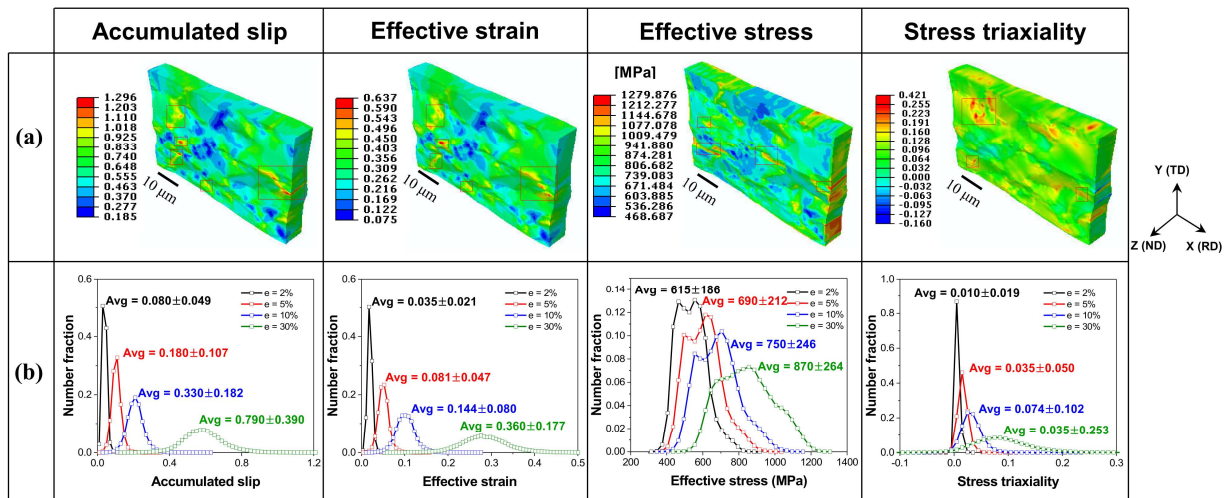


Fig. 5.8 (a) The CPFEM results of the accumulated slip, effective strain, effective stress and stress triaxiality distributions in the deformed RVEs ($e = 30\%$) and (b) histograms of these damaging indicators.

The distributions of effective stress and stress triaxiality in the deformed RVE are also depicted in Fig. 5.8(a). The deformed RVE reveals the inhomogeneous distributions of effective stress and stress triaxiality. It reveals that the localized deformation is also found in the deformed microstructure, which can coalesce to form shear bands during the deformation. It is found that the localized deformation distributes through the thickness, which plays an important role in the material failure of the specimen. It should be noted that the thickness of RVE is $9\ \mu\text{m}$ which is similar to the average grain size of $8.76\ \mu\text{m}$. This indicates that there is only one grain through the

thickness characterized by the thickness-to-grain size ratio. The previous study reported that the surface grains are responsible for the increased stress and strain heterogeneities, leading to the decreased fracture strains, consequently the failure in the material with only few grains through the thickness [145]. Thus, the overall deformation in the RVE is also predominantly governed by the surface grains which are less constrained and deformed more easily.

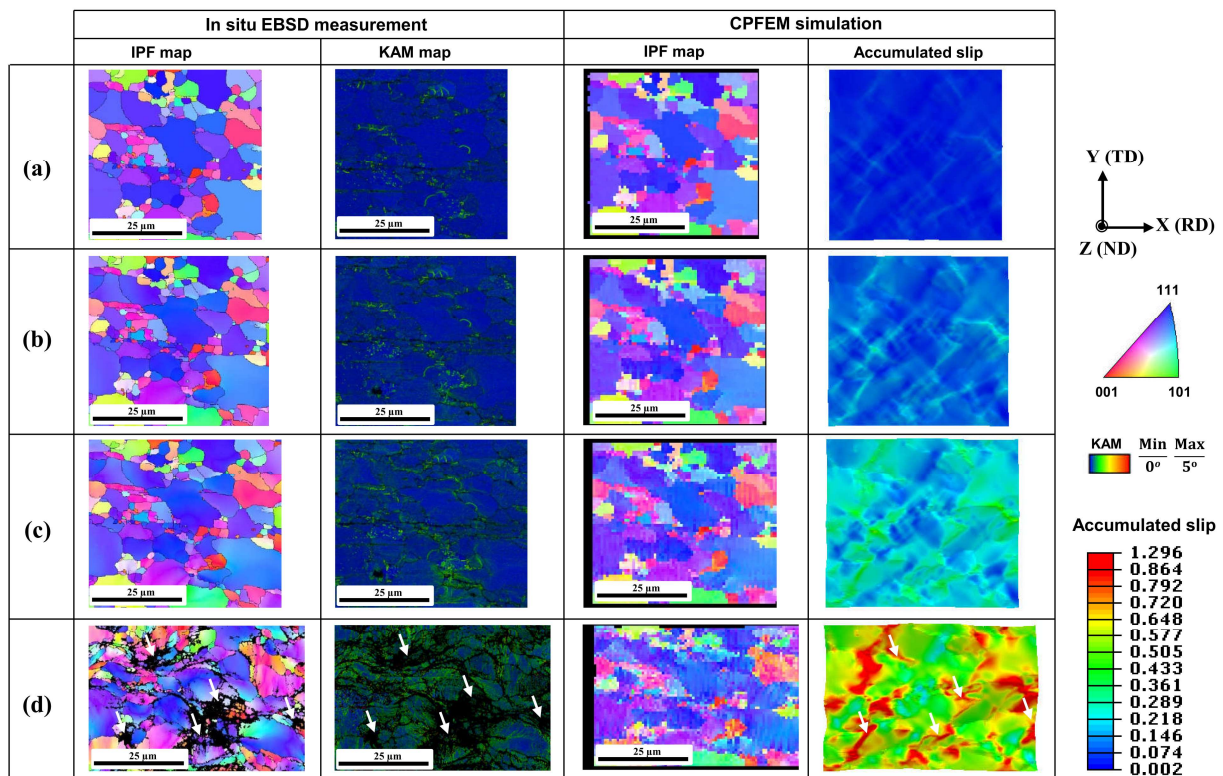


Fig. 5.9 The CPFEM results of IPF maps and accumulated slip in the deformed RVEs in comparison with the in-situ EBSD measurements at different engineering strain levels: (a) $e = 2$, (b) $e = 5\%$, (c) $e = 10\%$ and (d) $e = 30\%$.

Fig. 5.8(b) shows the histograms of the accumulated slip, effective strain, effective stress and stress triaxiality in the deformed RVE under different strains. The range of accumulate slip at small strain is narrow, however, it becomes much broader and shifts to the high values as the strain

increases. The distribution of the effective strain is similar to that of accumulated slip. As shown in Fig. 5.8(b), the more fractions of high values of accumulated slip and effective strain distributions at higher strain indicate the earlier onset of non-uniform and localized deformation in the microstructure of specimen. While the distributions of accumulated slip and effective strain are well bell-shaped, the effective stress result shows an irregular and no longer bell-shaped distributions. This indicates that the portion of material points is subjected to a relatively large deformation. The distribution of stress triaxiality shows a broader range with more fractions of high value with the increasing strain. The high stress triaxiality is attributed to the localized deformation which results in the earlier premature necking and failure of the material.

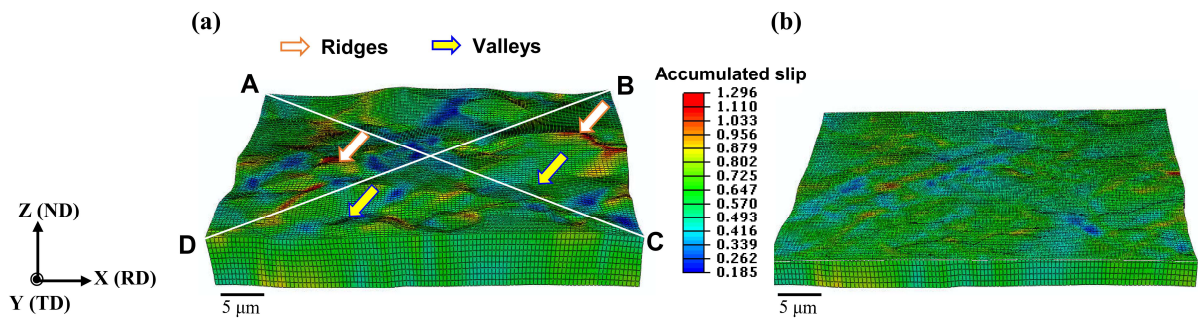


Fig. 5.10 The CPFEM results of surface morphology in the (a) free surface and (b) quarter layer in the deformed RVE ($\epsilon = 30\%$).

Fig. 5.9 shows the CPFEM results of IPF maps and accumulated slip in the deformed RVE in comparison with the in-situ EBSD measurements at different engineering strains. The IPF maps of the CPFEM simulation results were reconstructed as shown in Fig. 5.9. It reveals that the RVE shows a good reproduction fidelities of the crystallographic texture and grain structure. This confirms that the EBSD microstructure is successfully mapped onto the FE mesh in the RVE model, thus the microstructural changes during the deformation can be simulated and reproduced by the CPFEM. It is obvious that the orientation gradient gradually change as the deformation proceeds,

indicating the change in the crystallographic orientation of grains. Furthermore, the KAM map is included in order to compare with the accumulated slip obtained by the CPFEM simulation. It reveals that the localized deformation in the accumulated slip well matches with the local misorientation in the KAM. As the deformation proceeds, the strain localization is apparently found near the grain or sub-grain boundaries where the local misorientation is also observed in the KAM. At high strain of 0.3, the CPFEM result shows more inhomogeneous distribution of the accumulated slip. As indicated by the white arrow between the KAM and CPFEM results, the inhomogeneous strain localization and local hot spots of ductile fracture initiation in the accumulated slip well consistent with the experimental result. Although there are more localization observed in the accumulated slip, the CPFEM simulation can well reproduce the micromechanical deformation and failure behavior of the ultra-thin steel sheet during uniaxial tension.

5.3.3. Free surface effect on the failure behavior

As discussed in Sections 5.3.1 and 5.3.2, the surface of the specimen shows a considerable roughness appearance, together with the effect of surface grains on the increased stress and strain heterogeneities in the microstructure of the material. In this section, the effect of free surface on the failure behavior of the ultra-thin steel sheet will be discussed more detailed based on the CPFEM results.

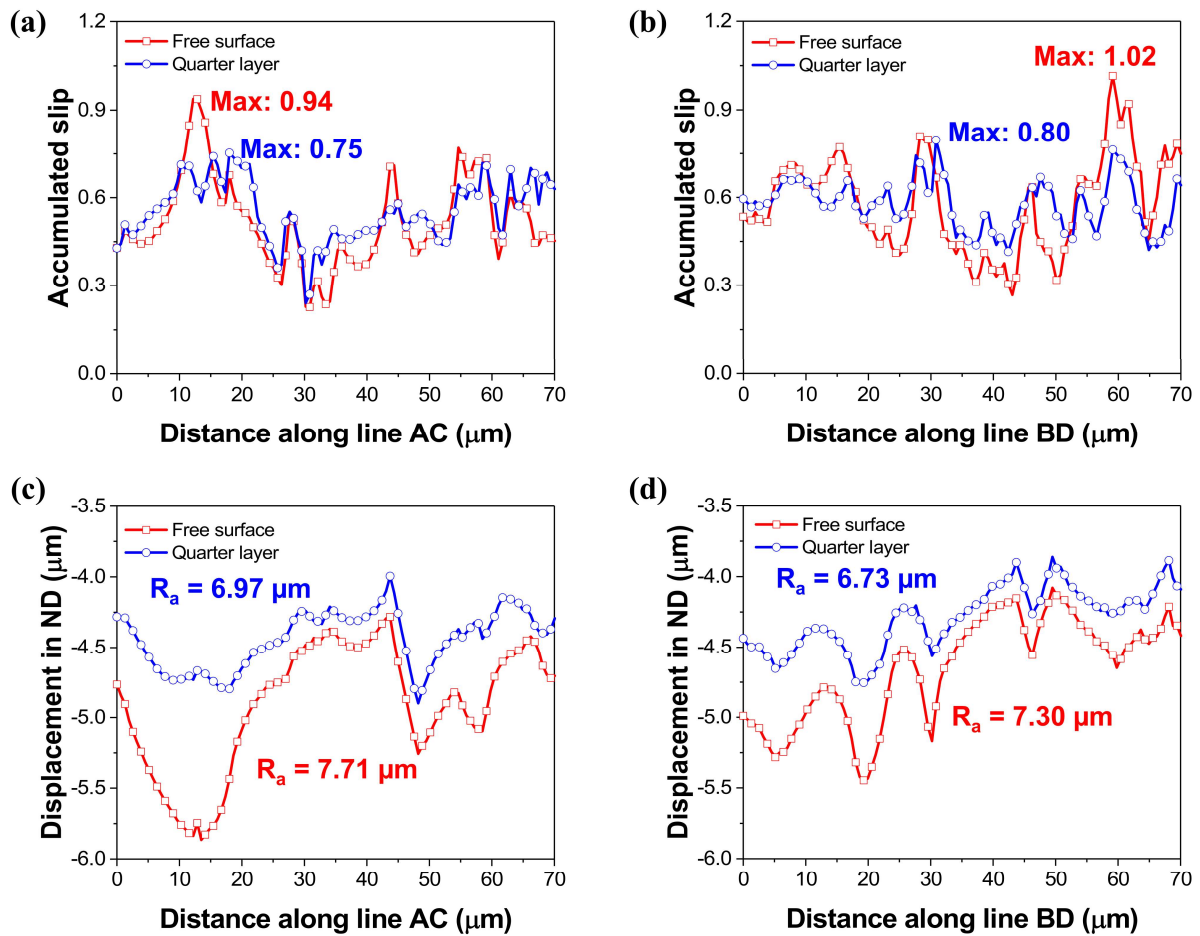


Fig. 5.11 The CPFEM results of accumulated slip and displacement in ND distributions in the free surface and quarter layer in the deformed RVE ($\epsilon = 30\%$) along the two representative white solid lines as indicated in Fig. 5.9: (a,c) AC and (b,d) BD.

Fig. 5.10 shows the CPFEM results of surface morphology in the free surface and quarter layer in the deformed RVE at the engineering strain of 0.3. Fig. 5.10 shows that the free surface exhibits a noticeable roughness with the ribbed appearance, which is consistent with the result of SEM map. An apparent distribution of ridges and valleys can be observed in the free surface as depicted in Fig. 5.10(a). This is due to the less constraint and easier deformation of the soft grains on the free surface. In contrast, the quarter layer is mainly dominated by the hard grains which are more

constrained making the deformation of these grains more difficult. Consequently, the quarter layer surface displays more homogeneous distribution as shown in Fig. 5.10(b). The CPFEM results show that the heterogeneous topography in the free surface is as the results of the early onset of localization deformation and premature necking. This indicates that the free surface with the roughening phenomenon significantly affects the formability and failure behavior of the material.

In order to quantitatively evaluate the surface roughening, two criteria are used in the present study. The first indicator is the mean surface roughness as follows

$$R_a = \frac{1}{L} \int_0^L |Z(x)| dx \quad (5.1)$$

where Z is the displacement in the thickness direction (ND). The second indicator is the thickness uniform parameter which is defined as follows

$$\xi = 1 - \frac{2R_t}{t_0 \exp(-\Gamma/2)} \quad (5.2)$$

where t_0 is the initial thickness, R_t is the maximum roughness height and Γ is the accumulated slip. Note that the Z_i , R_t and Γ are obtained from the CPFEM simulation. The R_a and ξ are calculated along the two representative lines (AC and BD) as indicated in Fig. 5.10(a).

Fig. 5.11 shows the CPFEM results of accumulated slip and displacement in ND distributions in the free surface and quarter layer in the deformed RVE at engineering strain of 0.3. Fig. 5.11(a) shows that the distribution of accumulated slip along the line AC in the free surface is more inhomogeneous than that in the quarter layer. Fig. 5.11(b) also shows a more non-uniform distribution with the higher portion of the material with high value of accumulated slip in the free surface along the line BD. As indicated in Figs. 5.11(a,b), the free surface shows higher maximum accumulated slip along both the AC and BD lines. It reveals the increase in the portion of the

material points in the free surface with higher accumulated slip, indicating the increase in the local strain deformation. This occurs in the region containing many soft grains which deform more easily, leading to the surface roughness. This can be apparently observed in Figs. 5.11(c,d). In Fig. 5.11(c), the displacement in ND along the AC line in the free surface shows a large variation while it is more uniform in the quarter layer. Consequently, the free surface shows a considerable roughness with higher value of R_a compared to the quarter layer. The displacement in ND along the BC line shows a similar distribution, however, the free surface exhibits a larger variation with the higher value of R_a . The results reveal that the high roughness in the free surface can facilitate the strain localization that promotes necking and premature failure of the material.

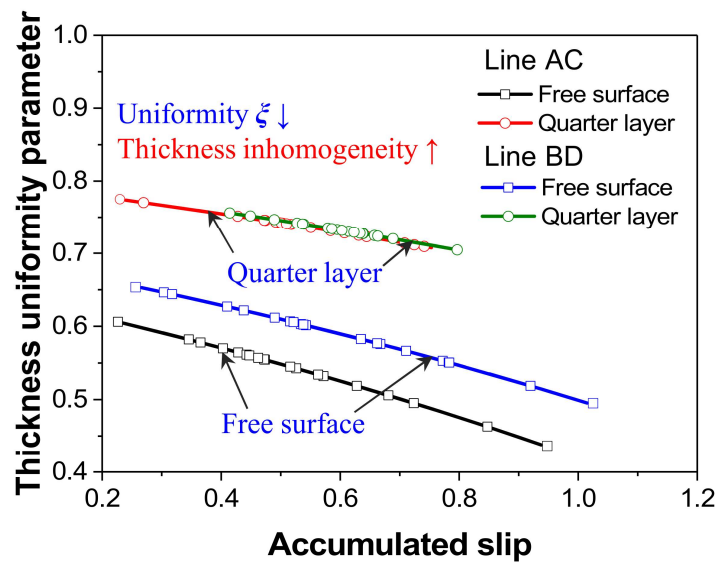


Fig. 5.12 Correlated thickness uniformity parameter and accumulated slip in the free surface and quarter layer in the deformed RVE ($e = 30\%$) along the two representative white solid lines (AC and BD) as indicated in Fig. 5.9.

Furthermore, Fig. 5.12 shows correlated thickness uniformity parameter and accumulated slip in the free surface and quarter layer in the deformed RVE. It is found that the thickness uniformity parameters for both the free surface and quarter layer show a proportional relationship which

linearly decreases with the accumulated slip. For the free surface, it reveals an apparent difference in the thickness uniformity parameter between AC and BD lines, while the difference is very negligible for the quarter layer. This indicates a more uniform distribution of thickness in the quarter layer. It is obvious that the thickness uniform parameters in the free surface is significantly lower than that in the quarter layer. The smaller thickness uniform parameter is, the larger thickness inhomogeneity will be. Thus, the increase in the thickness inhomogeneity results in the onset of localized deformation. The high roughening rate during the plastic deformation can be responsible for the noticeable thickness inhomogeneity [143]. In addition, the roughness phenomenon in the free surface can reduce the tensile ability, leading to the premature necking and failure of the material.

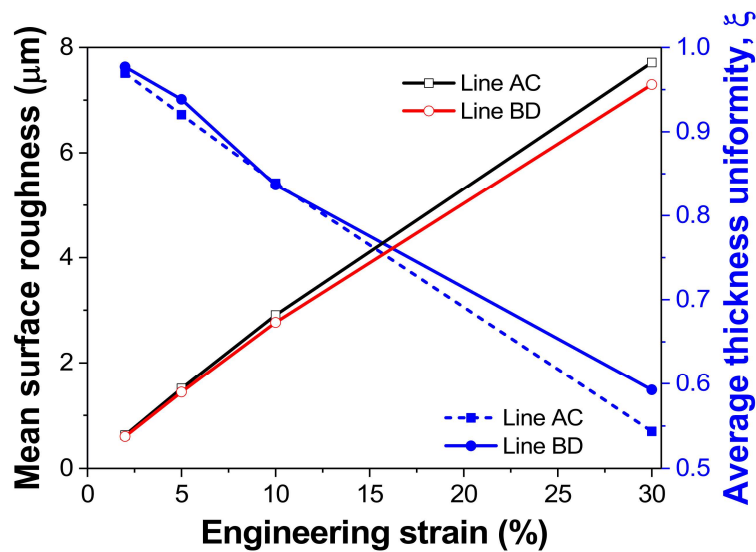


Fig. 5.13 Evolutions of mean surface roughness and average thickness uniformity parameter with the strains in the free surface in the deformed RVEs along the two representative white solid lines (AC and BD) as indicated in Fig. 5.9.

Fig. 5.13 shows evolution of mean surface roughness and average thickness uniformity parameter with the strains in the free surface in the deformed RVEs. The results show that the

mean surface roughness monotonically increases while the average thickness uniformity monotonically decreases with the increasing strain. It reveals that the noticeable increase in mean surface roughness results in the increased thickness inhomogeneity. In addition, the roughness phenomenon in the free surface can reduce the tensile ability, leading to the premature necking and failure of the material. Indeed, with the increase in thickness inhomogeneity, the localized deformation can take place at the thinnest zone in the thickness direction. Thus, the CPFEM results shows a strong correlation between thickness inhomogeneity induced by the roughness in the free surface and failure behavior in the ultra-thin steel sheet during the deformation.

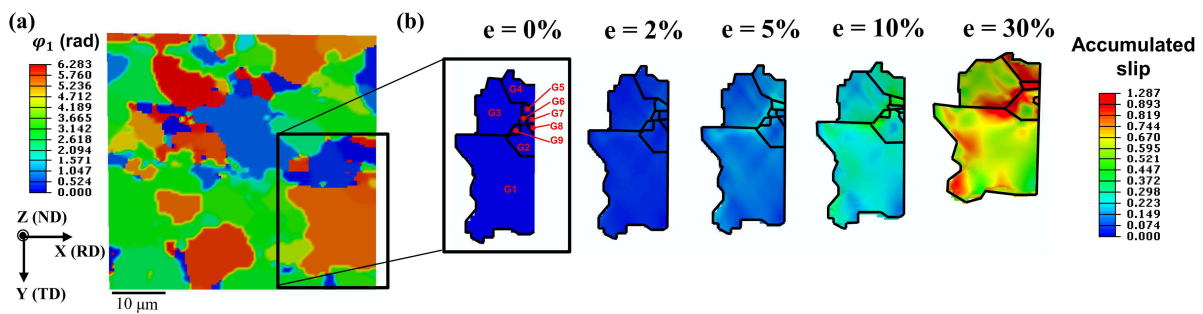


Fig. 5.14 (a) Microstructure of RVE in term of the first Euler angle φ_1 and (b) deformation behavior of the critical grains with the strains.

The difference in the grain deformation can significantly affect the failure of the material. Fig. 5.14 shows the microstructure of RVE in term of the first Euler angle φ_1 and deformation behavior of the critical grains with the strains. In Fig. 6.14(b), nine critical grains denoted G1–G9 are investigated to trace the change of individual grain with the strains. It is seen that the change of individual grain varies with different degree which depends on the location of individual grain. It reveals that the morphologies of these grains are noticeably changed after deformation, implying that these grains undergo apparently heterogeneous plastic deformation. At high strain of 0.3, a small sub-grains of G6–G9 are not easy to distinguish due to the severe deformation. In addition,

the localized deformation is found to be initiated from these grains and then propagated along the grain boundaries, which is consistent with the high local misorientation and dislocation density in the KAM and GND maps.

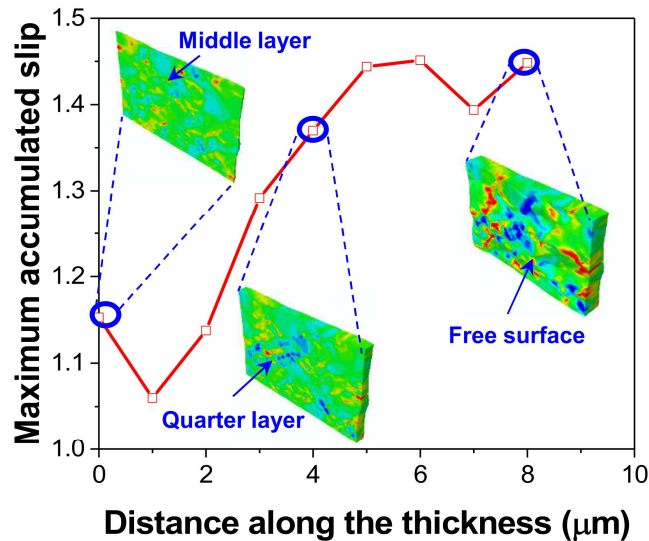


Fig. 5.15 The CPFEM results of accumulated slip distribution along the thickness direction.

Furthermore, Fig. 6.15 shows the CPFEM results of accumulated slip distribution along the thickness direction. It reveals a non-uniform distribution of the accumulated slip along the thickness direction. It is found that the free surface exhibits a higher accumulated slip, indicating that the early onset of localization can be initiated at the free surface due to the less constraint of the surface grains. In addition, the contour plots of surface morphology in the middle layer, quarter layer and free surface are shown in Fig. 5.15. It is apparent that the roughness in the free surface is more considerable compared to the others. This plays important role in the ductile fracture initiation during the deformation.

5.4. Conclusions

The effect of free surface roughening on the micromechanical deformation and failure behavior of ultra-thin ferritic stainless steel (FSS) sheet for bipolar plate in PEM fuel cell were comprehensively investigated by the in-situ electron backscatter diffraction (EBSD) technique and crystal plasticity finite element method (CPFEM). The in-situ EBSD measurement were performed to monitor the microstructural evolution during uniaxial tension. Then the initial microstructure was directly mapped onto the finite element mesh in the CPFE simulations. The following conclusions were drawn.

- (i) The evolutions of microstructure under the applied strains were apparently observed. At high strain of 0.3, the SEM map showed considerable surface roughness where the ridges and valleys were clearly observed, consequently facilitating the localization. While the boundary map showed an extensive LAGBs and deformation twinning was unobservable, implying that the deformation was predominantly attributed to the dislocation slip only.
- (ii) It revealed a significantly heterogeneous KAM distribution with the intragranular spread in addition to the high density of GND at the grain and sub-grain boundaries which can accommodate the plastic deformation. It was found that the formation of deformation-induced boundaries was responsible for the significant increase in the boundary density, leading to the dislocation piling-up that affected the deformation behavior of ultra-thin FSS sheet.
- (iii) The CPFEM predictions of stress/strain heterogeneity and the local hot spots of the ductile fracture initiation well matched with the experimental results. It was found that the localized deformation primarily distributed in the surface grains which were less constrained and deformed easily, leading to the increased stress and strain heterogeneities.

It revealed that the damaging indicators increased with more fractions of high value as the strain increased, resulting in the onset of localized deformation.

- (iv) Furthermore, the free surface exhibited a considerable roughness due to the heterogeneous plastic deformation of grains under the applied strains. The high surface roughness was responsible for the increased thickness inhomogeneity which facilitated the strain localization, consequently the premature necking and fracture in the ultra-thin FSS sheet.

CHAPTER 6

DESIGN OF MULTI-STAGE FORMING PROCESS OF ULTRA-THIN BIPOLAR PLATE FOR FORMABILITY IMPROVEMENT

Based on the previous findings in Chapters 4 and 5, a special remedy of new multi-stage die design approach for the forming of BPPs in PEM fuel cell was proposed and its effect on the formability of the micro-channel and macro-scale BPPs was investigated. The process design parameters of the proposed die were optimized by the developed artificial neural network (ANN) model integrated with the genetic algorithm (GA). The multi-scales finite element (FE) modelling with two-dimensional (2D) analysis of micro-channel BPP and three-dimensional (3D) analysis of macro-scale BPP in the two-step forming process were reliably established and performed to verify the proposed die design. The formability improvement of BPP was discussed in terms of stress/strain distribution and geometrical features (thickness reduction and shape error). With the proposed die design, the reduced twist angle and more uniform thickness distribution were induced, thus the distortion and local thinning were minimized to prevent the springback and fracture in the BPP channels.

6.1. Multi-stage forming process

Among the fabrication technologies of BPP, stamping process has been received much attention due to the high efficiency and low manufacturing cost [13]. For fabricating micro channel BPP with ultra-thin metallic sheets, however, the rupture as the major defect commonly occurs due to the severe thinning [146,147]. In addition, a high aspect ratio of the micro-channel BPP cannot be achieved by the traditional stamping process [148].

Recently, multi-stage forming process with several stages to form the sheet metal parts has been demonstrated as a promising method to overcome the drawback caused by a single-stage stamping process [51,52,149–151]. Xu et al. [51] reported that the aspect ratio and the base angle of the multi-stage formed micro-channel BPP were effectively improved. Zhang et al. [52] showed that the forming depth and more uniform thickness distribution of micro channel BPP in addition to the improved power density and voltage distribution uniformity of PEM fuel cell were achieved by employing multi-stages forming process.

In this research, therefore, multi-stage forming process was adopted to improve the formability of ultra-thin FSS sheet for fuel cell BPP. The whole forming process was divided into two stages and in the pre-forming stage, a novel die design approach was proposed. It is time-consuming and expensive to fabricate the proposed die approach to explore its effect. Therefore, the finite element (FE) simulation was adopted as complementary numerical tool to direct the experiment. The FE simulations of multi-stage forming of both micro-channel and macro-scale BPP were conducted to confirm the effect of proposed die approach on the formability of ultra-thin BPP. In addition, the multi-stage forming simulation using the conventional pre-forming die design was also conducted for the comparison.

6.2. Process design of multi-stage forming

6.2.1. Propose of pe-forming die design

It is seen that the thinning is concentrated intensively at the material point, such as the channel corner of BPP as indicated in Fig. 6.1, where a severe deformation take places during the forming process. Fig. 6.2. shows the schematic of forming process using the conventional die design with various geometrical parameters such as the tool width (w), tool fillet radius (r), tool gap (c) and channel height (h). In order to avoid severe deformation at the local region and meet the forming accuracy, existing researches have made an attempt to change different processing parameters design [150], apply heat treatment [152] or even increase the number of stages [51] in multi-stage forming process. Furthermore, it requires an excessive experiments or numerical simulations to be conducted for optimization of the various processing parameters design in multi-stage forming. Motivated by these challenges, a new pre-forming die design approach was suggested to induce the uniform thickness distribution, consequently preventing the rupture.

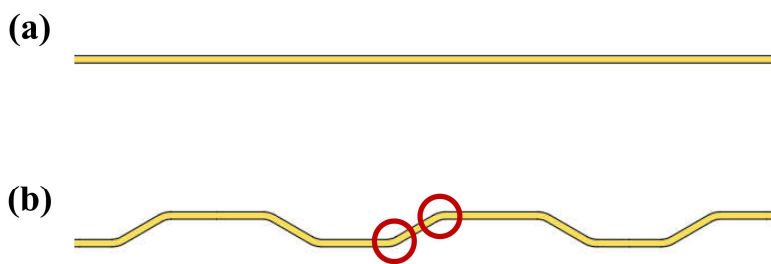


Fig. 6.1 Schematic of the bipolar plate (a) before and after forming.

Fig. 6.3 shows the illustration of deformation aspect in the micro-channel BPP with the conventional and proposed approaches. For the conventional design approach in Fig. 6.3(a), when the sheet material is formed into the die cavity, the local region of micro-channel corners usually undergo a severe deformation to make uniform stretching in the rib region at the bottom of micro

channel due to the existing design of die. This phenomenon leads to the reduction in the thickness at the micro-channel, accordingly the local thinning. In order to overcome this drawback, a new propose is to make the premier deformation on the rib region and the neighboring area around the corners of micro-channel BPP as indicated in Fig. 6.3(b). The final shape of micro-channel BPP is then formed in the second stage forming. With the proposed approach, the stretching-dominated deformation is well controlled throughout the micro-channel BPP by employing a two-stage forming process, thus uniform thickness distribution is induced to prevent the local thinning, consequently the fracture in the ultra-thin BPP.

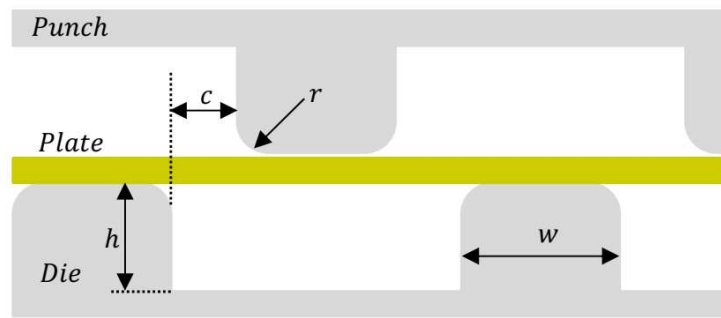


Fig. 6.2 Illustration of process design parameter in the conventional die forming process.

For this purpose, a new die design of pre-forming stage is proposed as shown in Fig. 6.4. The process design parameters of proposed die are shown in Fig. 6.4(a) and their definition is given in Table 6.1. The key characteristics of the proposed die tool are the projection and fillet radius which affect the stretching-dominated deformation of entire micro-channel BPP as depicted in Fig. 6.4(b). In order to meet the forming quality and accuracy, the process design parameters of proposed die are also properly determined by the FE simulation and artificial intelligence-based approach.

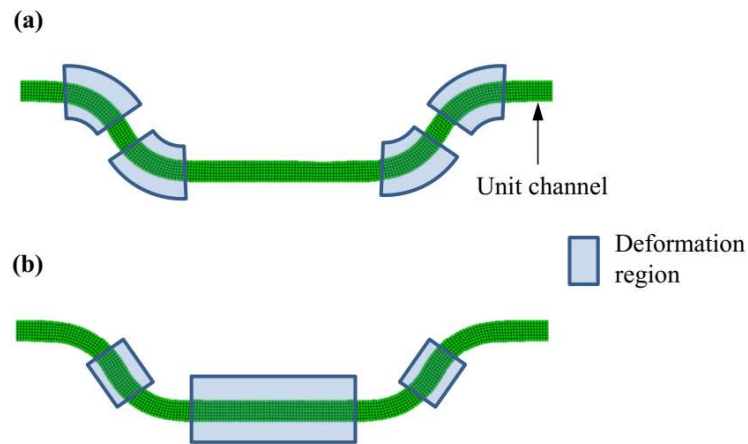


Fig. 6.3 Schematic of the microchannel deformation aspect of the (a) conventional and (b) proposed approaches.

6.2.2. Micro-channel BPP simulation

The effect of proposed die design on the formability of micro-channel BPP was firstly verified by the numerical analysis. For the efficient analysis, the 2D FE simulations were conducted on the cross-section perpendicular to the channel length direction, as shown in Fig. 6.5(a). In addition, symmetrical boundary conditions are imposed on the BPP thickness direction due to the symmetrical geometry for the sake of saving computational cost. The FE simulations were conducted in the commercial software Abaqus/standard. As shown in Fig. 6.5(b), the 2D model was established for a two-step multi-stage forming simulations. After the first-stage deformation with the proposed die design, the deformed BPP channel is subjected to the second-stage forming simulation by using the predefined-filed function in Abaqus. For each stage, the forming process consists of loading and unloading steps. In the loading step, the explicit analysis is conducted while the unloading step is implicitly simulated for the analysis of springback. The different solver is because the implicit analysis shows higher accuracy in addition to the saving computational time.

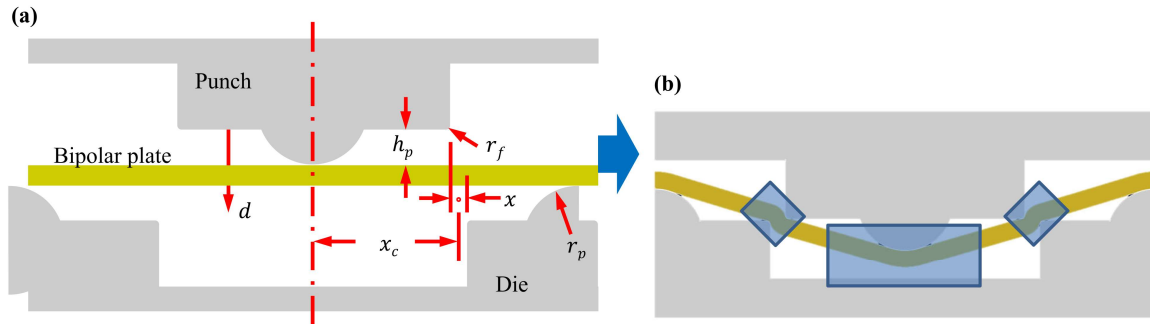


Fig. 6.4 Illustration of proposed pre-forming die approach with (a) the process design parameters and (b) its effect on the deformation aspect.

Table 6.1. Definition of process design parameters of the proposed die approach with their initial values (mm).

r_p	Projection radius	0.5 ± 0.1	d	Punch displacement	0.375 ± 0.025
h_p	Projection Height	0.11 ± 0.025	x_c	Gap Center position	0.6 ± 0.025
r_f	Fillet radius (Die and Punch)	0.11 ± 0.025	x	Gap	0.08 ± 0.01

As shown Fig. 6.5(b), the punch and die are modelled with the rigid bodies whose material properties do not need to be defined. The die is fixed in all directions, while the punch can move in the vertical direction. The deformation body is applied in the FSS sheet consisting of 6.5 channels with the thickness of 0.08 mm. The FSS bipolar plate sheet is simulated with the von Mises plasticity properties using the Voce hardening model as, $\sigma = 743 - 333 \exp(-8.25 \cdot \varepsilon^p)$ (MPa). For the springback analysis, the isotropic hardening model, available in the library of commercial software Abaqus, is considered. The BPP sheet material is initially meshed using a four-node plane strain elements (CPE4R) with the reduced integration. The total number elements

of 11,242 is used and there are seven elements along the thickness direction. A penalty contact is applied between the tool and BPP sheet by the surface-to-surface model. The friction coefficient of 0.1 is adopted [153]. Then, the FE simulations were conducted using the proposed die design with various geometrical parameters as shown in Fig. 6.4(a). In order to evaluate the effect of the proposed approach, however, the geometrical parameters were properly optimized. In addition, the FE simulations of multi-stage forming using the conventional pre-forming die design were carried out with the same FE analysis conditions.

6.2.3. Optimization of process design parameters with ANN

In this research, artificial neural networks (ANN) integrated with genetic algorithm (GA) was developed to optimize the process design parameters of the proposed die approach. The ANN-GA model has been demonstrated as an efficient and powerful method to optimize the processing parameters [154]. Firstly, the ANN model was developed as shown in Fig. 6.6. The ANN model consisted of three layers of input, hidden and output. As shown in Fig. 6.6, six geometrical parameters of proposed die design and one parameter of punch displacement were defined as the input layer while the output layer are the minimum thickness and standard deviation of thickness. The transfer functions in the hidden and output layers were in the form of the hyperbolic tangent sigmoid (tansig) and linear (purelin).

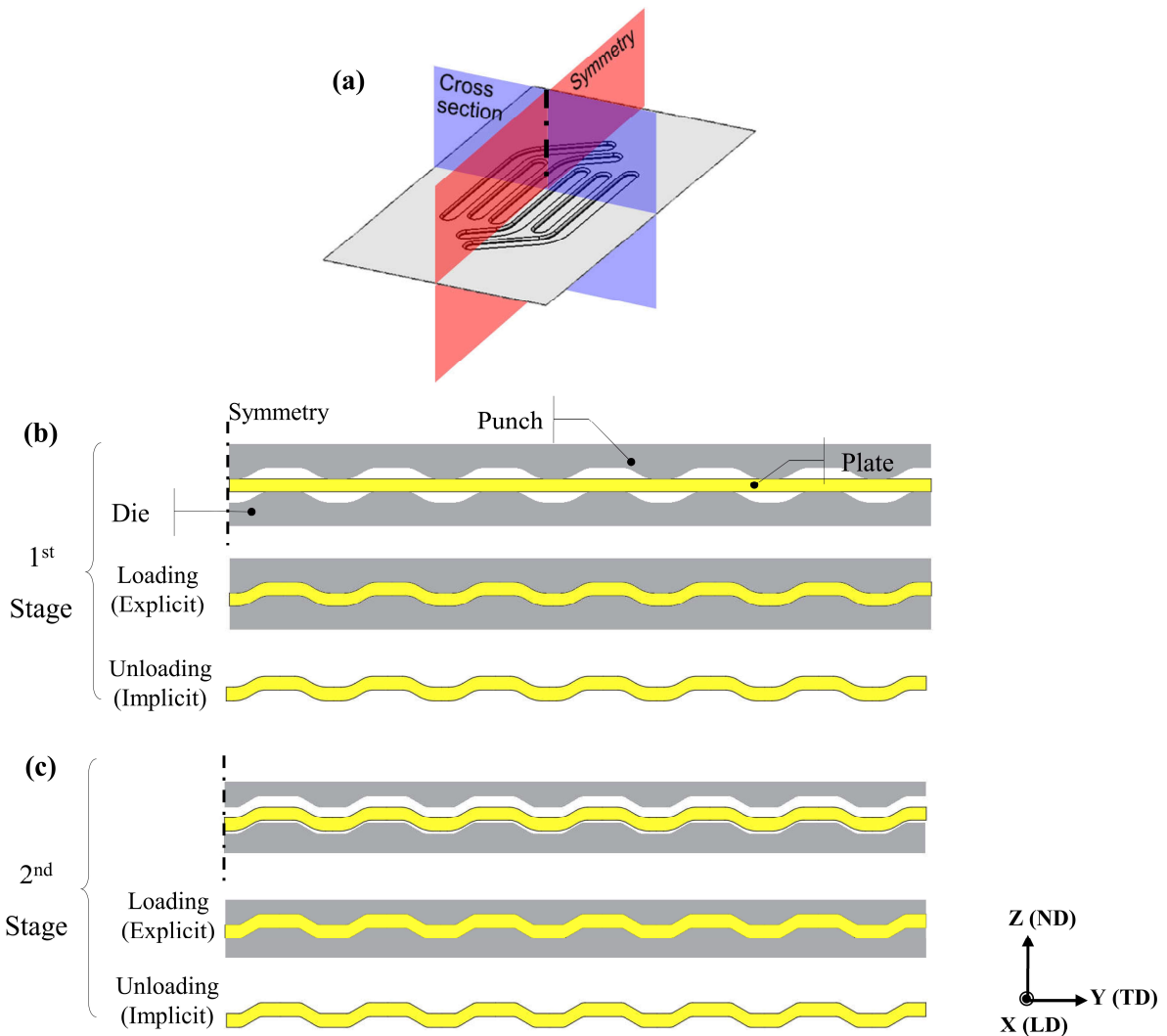


Fig. 6.5 (a) Illustration of cross-sectional and symmetrical plane and 2D finite element mode for (a) first and (b) second stages forming.

For the sake of saving costs, FE simulations of multi-stage forming were carried out to generate the dataset for developing ANN model. The initial value with the standard deviation of six geometrical parameters (the same fillet radius for the die and punch tools) and one parameter of punch displacement is given in Table 6.1. Three levels of each parameter were assumed and a full factorial design was applied to generate the number of data samples. Accordingly, a series of 2,187

FE simulation of multi-stage forming were conducted to obtain the minimum thickness and standard deviation of thickness. Then, the dataset of input and output were used in the development of ANN model.

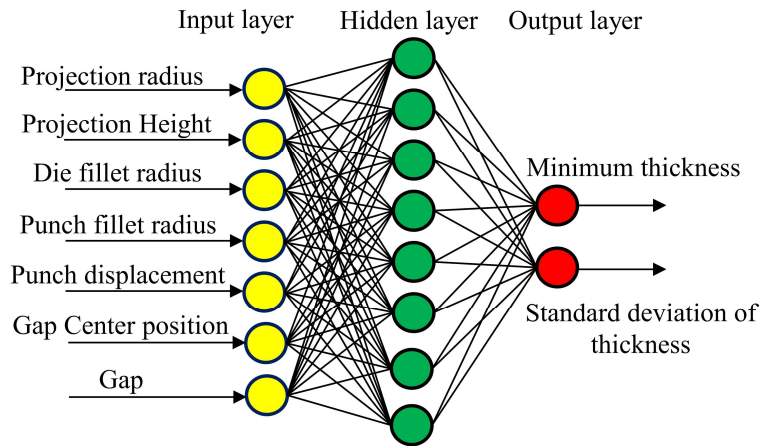


Fig. 6.6 Architecture of artificial neural network (ANN) for prediction of minimum thickness and standard deviation of thickness.

The three-layer ANN model was conducted using a feedforward back propagation neural network in the MATLAB environment. Prior to training, the input and output data were normalized in the range of 0 and 1 to increase accuracy and speed of the network. Then, the ANN model was trained and validated by 70% and 30% data samples of input and output, respectively. Fig. 6.6 shows the developed ANN with one hidden layer and eight hidden neurons. The performance of the ANN model was evaluated by mean square error (MSE) and coefficient of determination (R^2) as follows

$$MSE = \frac{1}{n} \sum_{i=1}^n (y_i - \hat{y}_i)^2 \quad (6.1)$$

$$R^2 = 1 - \frac{\sum_{i=1}^n (y_i - \hat{y}_i)^2}{\sum_{i=1}^n (y_i - \bar{y})^2} \quad (6.2)$$

where y , \hat{y} and \bar{y} are the target, predicted and average target values of output parameters respectively, n is the number of data samples used in the ANN model.

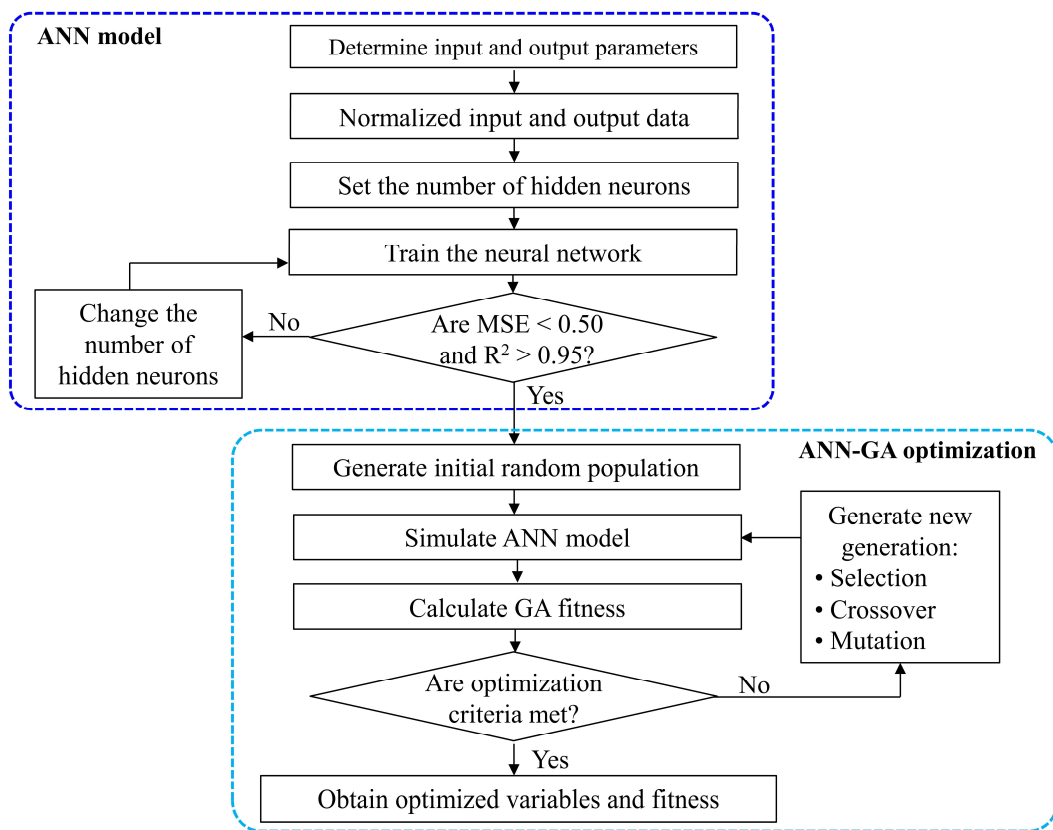


Fig. 6.7 Artificial neural network (ANN) integrated with genetic algorithm (GA) for optimization of process design parameters.

Then, the developed ANN model was coupled with the GA as shown in Fig. 6.7. The uniqueness of the integrated ANN-GA model is capable of finding the optimized variables without giving the explicitly mathematical function of the objective, since the trained ANN model is used

as an objective function in GA to calculate the fitness value. As shown in Fig. 6.7, the best ANN model with the highest performance in terms of MSE and R^2 is then imposed into the GA optimization. The GA is performed by randomly generating the initial population. Based on the best trained ANN model, the fitness is calculated for all initial individuals. As the criteria optimization is not satisfied, the new generation is reproduced by using three operators of selection, crossover, and mutation. The process is repeated until the maximum population size or generation size is reached. In this model, the population and generation sizes were given as 100 and 200, respectively. The probability of crossover rate and mutation were set as 0.85 and 0.01, respectively, to establish the ANN-GA model for optimization of process design parameters of proposed die approach.

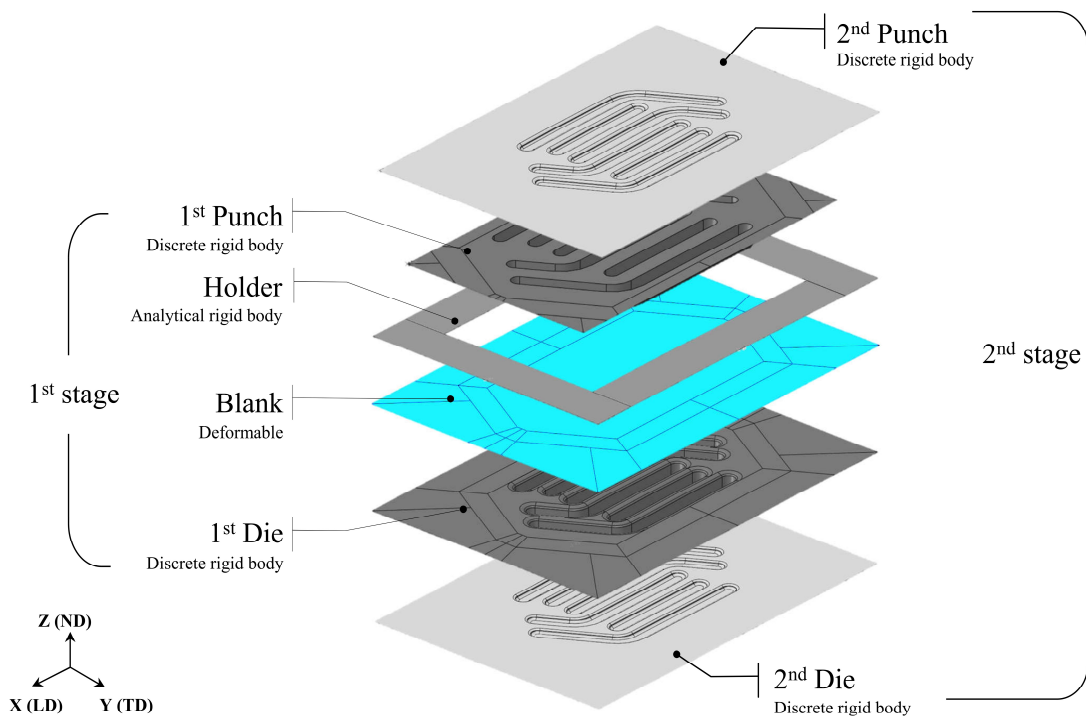


Fig. 6.8 3D finite element model for multi-stage forming simulation of macro-scale BPP channel.

6.2.4. Macro-scale BPP simulation

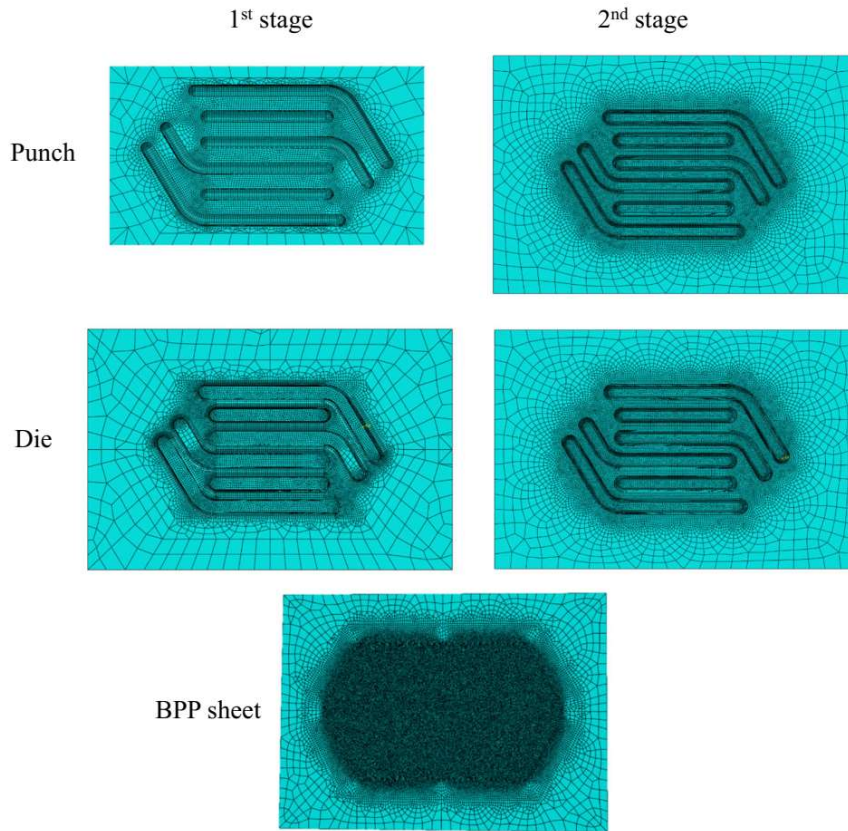


Fig. 6.9 Finite element meshes of die and punch tools and BPP sheet for the multi-stage forming simulation.

Furthermore, the 3D FE simulation of macro-scale BPP was conducted to analyze the effect of proposed die design on the formability of full channels, particularly the springback which cannot be revealed in the micro-channel simulation. Fig. 6.8 shows the macro-scale model for a two-step multi-stage forming of full BPP channel with the 3D geometries of tools and BPP sheet. The same FE conditions with the 2D analysis were applied in the 3D simulation. Fig. 6.9 shows the FE mesh of 3D model. The BPP sheet is meshed with 95,244 elements in total using most of four-node shell element (S4R) with the reduced integration and partial of three-node shell element (S3). Then, the 3D FE simulation of multi-stage forming of macro-scale BPP channel was conducted using the

optimal process design parameters of the proposed die approach. For the comparison, the 3D FE simulation using the conventional die design was also conducted.

6.3. Results and discussion

6.3.1. ANN-GA optimization

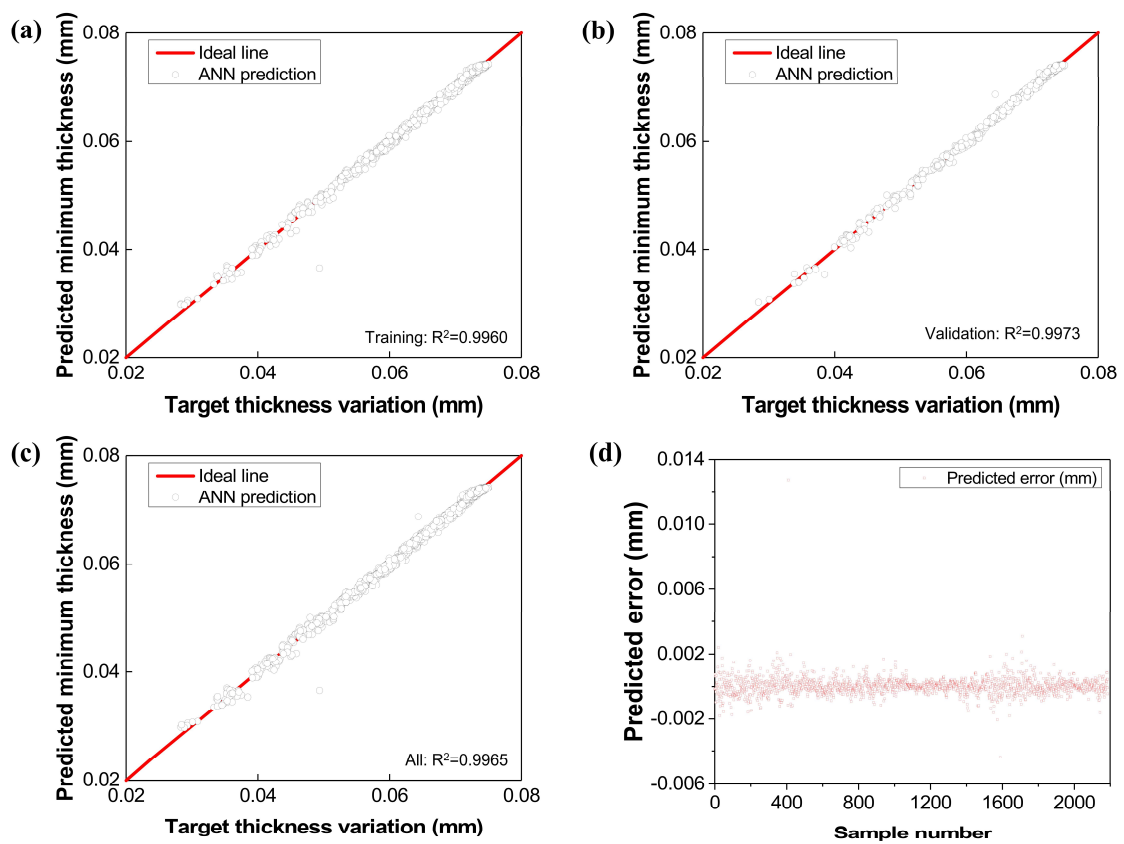


Fig. 6.10 ANN model prediction with coefficient of determinations for (a) training, (b) validation, (c) all, and (d) compared results between the target and predicted minimum thickness.

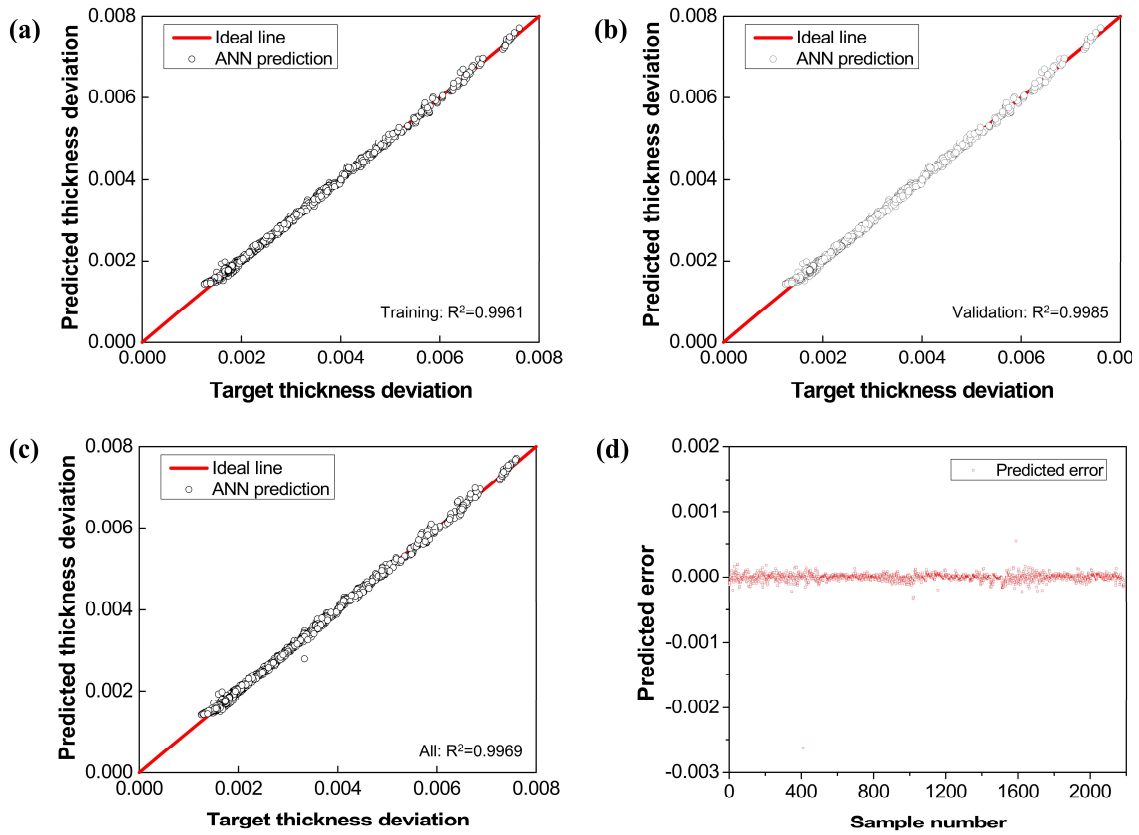


Fig. 6.11 ANN model prediction with coefficient of determinations for (a) training, (b) validation, (c) all, and (d) compared results between the target and predicted thickness standard deviation.

Table 6.2. Optimized process design parameters obtained by ANN-GA model (mm).

Projection height	Projection radius	Fillet radius		Punch displacement	Gap center position	Gap
		Die	Punch			
0.1338	0.593	0.1228	0.1308	0.3982	0.621493	0.0887

Figs. 6.10 and 6.11 show the ANN model predictions of minimum thickness and standard deviation of thickness in comparison between the predicted and target values. It is obvious that

both trained, validated and all predictions are in good agreement with the FE results. It reveals that the ANN model accurately reproduced the minimum thickness and standard deviation of thickness with the same best overall R^2 of 0.997 in addition to the relatively small error. This implies that the developed ANN model is reasonable and able to be used as the fitness function in GA for the optimization. Accordingly, the optimized process design parameters of the proposed die approach were determined by the integrated ANN-GA model, as summarized in Table 6.2, and employed in the multi-scale FE simulations of micro-channel and macro-scale BPPs in order to evaluate the effect of new die design on the formability.

6.3.2. Evaluation of formability in the micro-channel BPP

6.3.2.1. Influence on the stress/strain distribution

Fig. 6.12 shows the 2D FE simulation results of ultra-thin BPP channel by employing multi-stage forming using the proposed die approach. For the comparison, the simulation results of micro-channel by using the conventional design is also revealed in Fig. 6.12. Note that the optimized process design parameters of the conventional die design were adopted from the literature [150] and employed in the FE simulation.

Fig. 6.12(a) shows the final shape of BPP channel cross-sectional formed by the multi-stage forming simulation. The results of von Mises stress and effective plastic strain distributions in the single micro-channel near the symmetric axis (as marked by the red square) are shown in Figs. 6.12(b,d). Fig. 6.12(b) shows that the multi-stage forming can reduce the stress concentration at the corners of the micro-channel, thus inducing uniform stress distribution through the micro-channel. Although the proposed die approach shows a little higher maximum stress as indicated

by the red circle, the stress distributions compared between the conventional and proposed die approaches are relatively similar. In Fig. 6.12(c), the proposed die approach exhibits slightly higher maximum strain but more uniform distribution of effective plastic strain compared to the conventional one. Fig. 6.12(d) shows the histogram of maximum von Mises stress and effective plastic strain in the single micro-channel. It reveals a negligible difference between the conventional and proposed die approaches.

It is found that the boundary conditions can affect the simulation results. Therefore, the further FE simulations were conducted with the clamping by fixing the end of micro-channel in the TD direction as indicated in Fig. 6.13(a). Figs. 6.13(b,c) shows the von Mises stress and effective plastic strain distributions in the single micro-channel with the clamping. Fig 6.13(b) shows that both the die approaches reveal a more uniform stress distribution. As indicated in Fig. 6.13(b), the conventional die design shows relatively higher local maximum stress than that in the proposed one. The higher maximum stress can result in the severe thickness reduction and the rupture [52,147]. With the proposed die approach, however, the maximum stress concentration can be reduced, leading to the reduction in the local thinning, consequently improving the formability. Furthermore, compared to the conventional design, a more uniform distribution of effective plastic strain with the reduced maximum strain is found in the single micro-channel with the proposed approach. This can result in the reduction of strain localization, accordingly the local thinning.

Fig. 6.13(d) shows the histogram of maximum von Mises stress and effective plastic strain in the single micro-channel BPP. It reveals that the proposed die approach shows a significant decrease in von Mises stress and effective plastic strain by 13.9% and 8.3%, respectively. This

leads to the reduction of local thinning and fracture, consequently improving the formability in the multi-stage forming of micro-channel BPP.

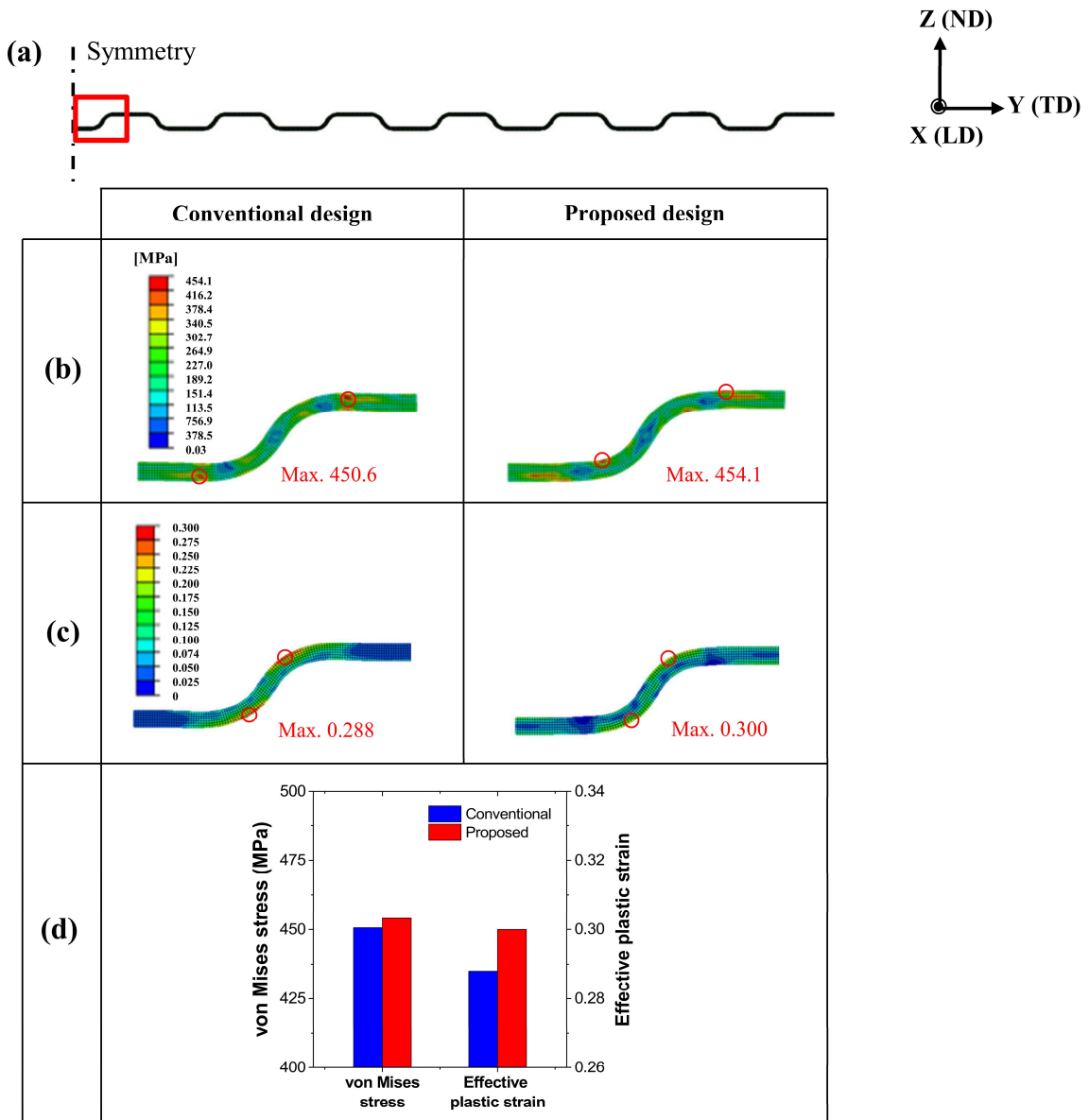


Fig. 6.12 (a) Final formed shape of BPP channel without clamping and corresponding (b) von Mises effective stress and (c) effective plastic strain distributions in the single BPP channel, and (d) histogram of maximum value of these variables compared between the conventional and proposed die design approaches.

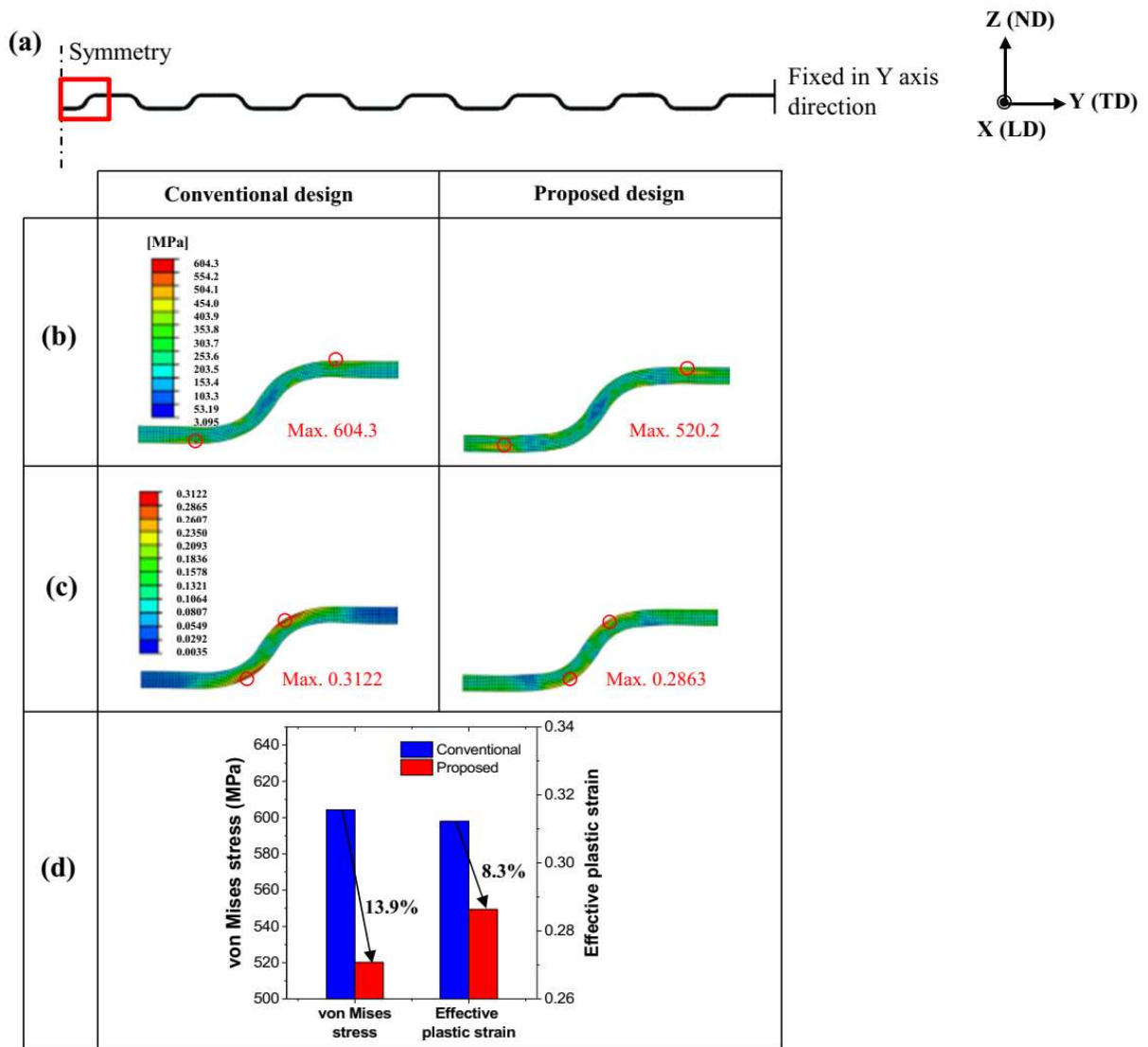


Fig. 6.13 (a) Final formed shape of BPP channel with clamping and corresponding (b) von Mises effective stress and (c) effective plastic strain distributions in the single BPP channel, and (d) histogram of maximum value of these variables compared between the conventional and proposed die design approaches.

6.3.2.2. Influence on the thickness distribution

Fig. 6.14 shows FE simulation results of the thickness distribution in the micro-channel BPP after multi-stage forming without the clamping. Fig. 6.14(a) shows that the conventional design reveals a non-uniform distribution of thickness throughout the micro-channel. It is seen that the thickness significantly reduced at the upper and lower channel corners. This leads to the excessive thinning in the micro-channel, consequently facilitating the fracture. With the proposed die approach, however, a more uniform thickness distribution is apparently revealed. It is found that the reduction in the thickness of micro-channel is noticeably improved, particularly at the channel corners, compared to the conventional one. Thus, the local thinning is obviously reduced and the rupture is prevented. This can be attributed to the more uniform distribution of effective plastic strain in the micro-channel BPP with the proposed die design aforementioned. Although the proposed approach shows negligible effect on the stress distribution, a significant influence on the improved thickness distribution in the micro-channel BPP is found.

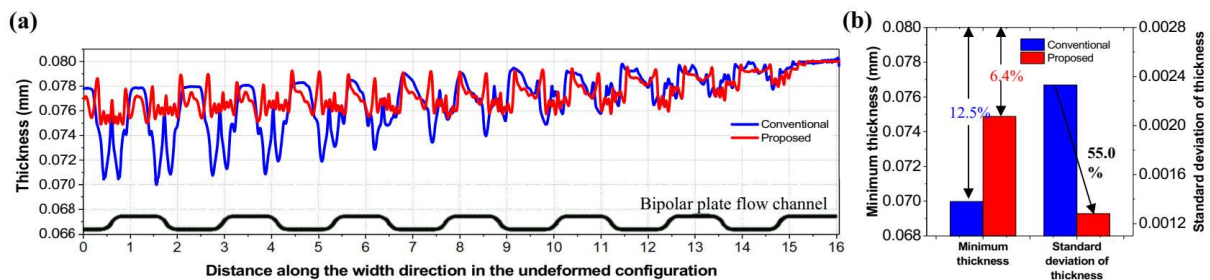


Fig. 6.14 (a) 2D finite element results of thickness distributions in the micro-channel BPP without clamping and (b) histogram of minimum thickness and standard deviation of thickness compared between the conventional and proposed die design approaches.

For a quantitative comparison, Fig 6.14(b) shows the histogram of minimum thickness and standard deviation of thickness in the micro channel BPPs compared between the conventional

and proposed die approaches. It reveals that the minimum thickness reduction at the upper and lower channel corners with the conventional approach is 12.5%, which is greater than that value of 6.4% with the proposed approach. This indicates that the proposed approach noticeably improves the thickness reduction. In addition, compared to the conventional approach, the thickness standard deviation with the proposed approach is significantly reduced by 55%, indicating the more uniform thickness distribution throughout the micro-channel BPP. The results confirm that the proposed die design approach significantly reduces the local thinning and the rupture, thus improving the formability in the multi-stage forming of ultra-thin BPP for PEM fuel cell.

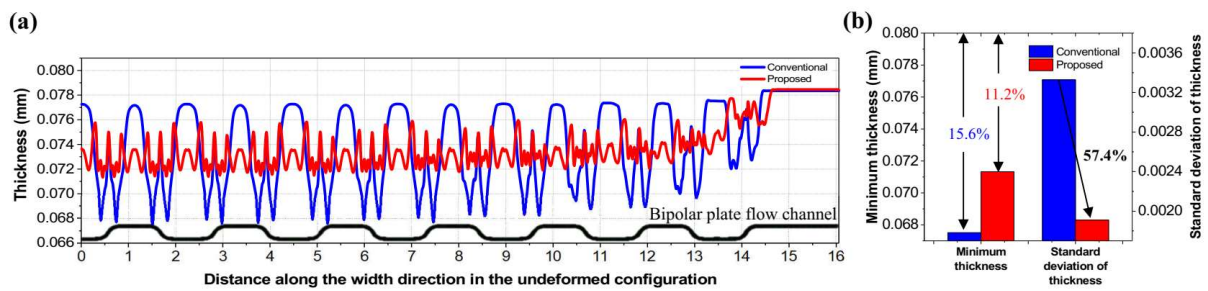


Fig. 6.15 (a) 2D finite element results of thickness distributions in the micro-channel BPP with clamping and (b) histogram of minimum thickness and standard deviation of thickness compared between the conventional and proposed die design approaches.

Furthermore, Fig. 6.15 shows the FE simulation results of the thickness distribution in the micro-channel BPP after multi-stage forming with the clamping. Fig. 6.15(a) shows that the conventional design exhibits a significantly heterogeneous distribution of thickness throughout the micro-channel BPP. It is found that the severe thinning is mainly concentrated at the upper and lower channel corners due to the significant thickness reduction. Such excessive severity of thinning results in the rupture, consequently the fracture in the ultra-thin BPP. This is caused by

the high stress concentration aforementioned. Zhang et al. [49] also reported that obvious thinning in the internal fillet radius of micro-scale flow channel is attributed to the stress concentration and large radial tensile stresses. In Fig. 6.15(a), however, the proposed design reveals a more uniform thickness distribution throughout the micro-channel. It reveals that the thickness at the channel corners is significantly greater than that in the conventional approach. This indicates that thinning is noticeably improved to prevent the rupture. A significant improvement in the thickness reduction can be attributed to the considerable decrease in the stress/strain concentration as revealed in previous Section.

Fig. 6.15(b) shows the histogram of minimum thickness and standard deviation of thickness in the micro channel BPPs compared between the conventional and proposed die approaches. It reveals that the minimum thickness reduction which primarily occurs at channel corners with the proposed approach is 11.2%, which is less than that value of 15.6% with the conventional design. This implies that the thickness reduction is noticeably enhanced with the proposed approach. In addition, the proposed approach reveals a significant reduction in the thickness standard deviation by 57.5%, compared to the conventional one. Such reduction of thickness standard deviation is due to the more uniform thickness distribution throughout the micro-channel BPP. The results demonstrate that the multi-stage forming of ultra-thin BPP with the proposed die design approach reveals a significant improvement on the formability by inducing the more uniform thickness distribution with the increase in the minimum thickness in order to prevent the excessively localized thinning and fracture.

6.3.2. Evaluation of formability in the macro-scale BPP

6.3.3.1. Influence on the thickness distribution

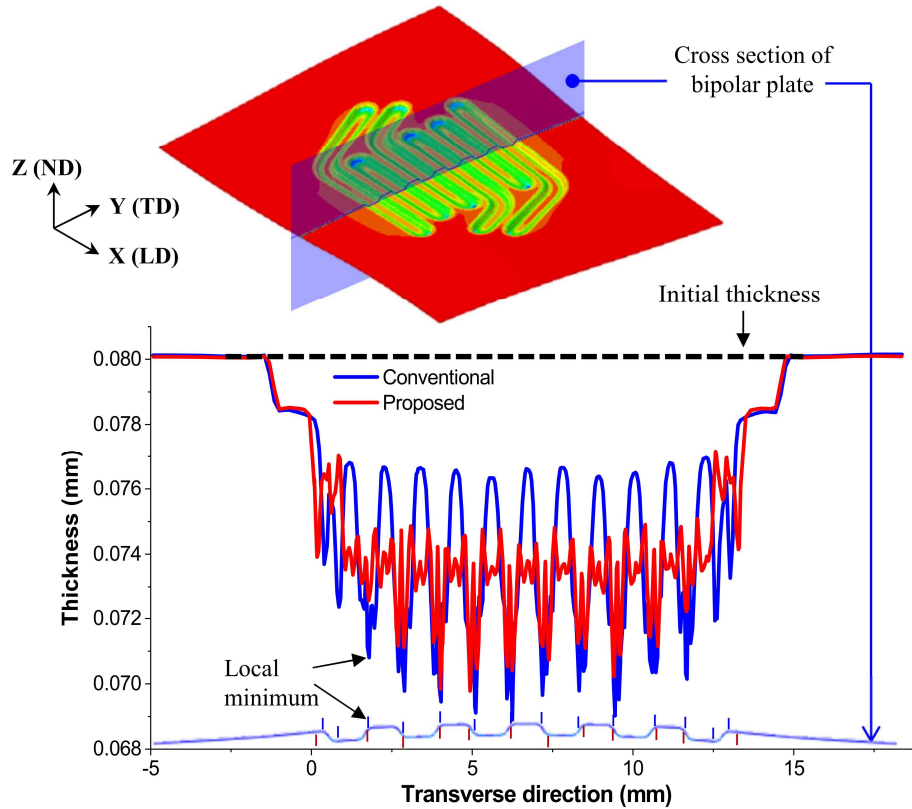


Fig. 6.16 3D finite element results of thickness distributions in the macro-scale BPP channel compared between the conventional and proposed die design approaches.

Fig. 6.16 shows the 3D FE simulation results of thickness distribution in the macro-scale BPP channel formed by the multi-stage forming. The thickness is measured at the cross-section center along the transverse direction. It reveals that the conventional design shows the excessive local thinning which mainly concentrated at the channel corners, resulting in a non-uniform distribution of thickness throughout the BPP channel. In contrast, a more uniform thickness distribution is apparently found in the BPP channel with the proposed approach. This is attributed to the

significant improvement in the thickness reduction which leads to the local thinning after the forming process.

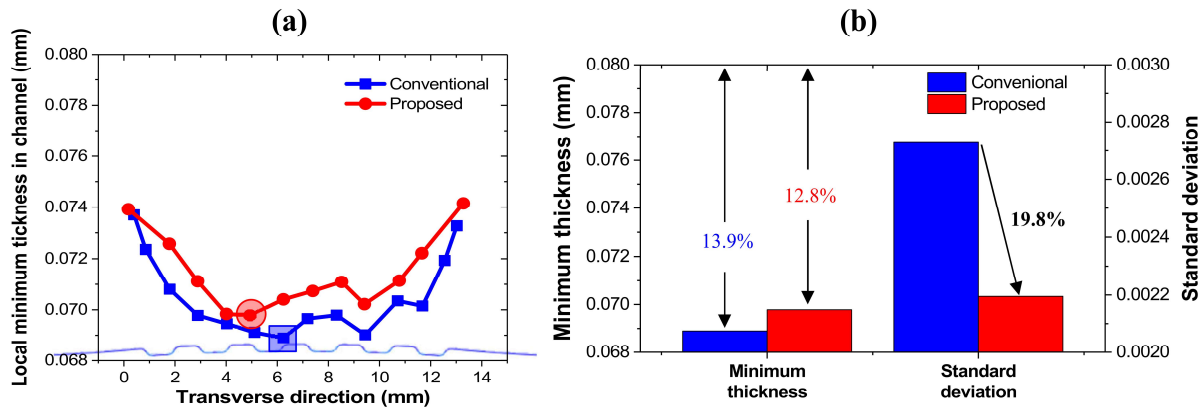


Fig. 6.17 3D finite element results of (a) local minimum thickness distributions in the macro-scale BPP channel and (b) histogram of minimum thickness and standard deviation compared between the conventional and proposed die design approaches.

Fig. 6.17(a) shows the local minimum thickness distribution along the transverse direction in the macro-scale BPP channel. The results show that the proposed approach shows greater local minimum thickness than that in the conventional one, indicating the improvement in the thickness reduction. For example, the minimum thickness at the fifth channel with the proposed design is higher than that at the seventh channel with the conventional one, as indicated in Fig. 6.17(b). This is quantitatively compared in Fig. 6.17(b). Compared to the initial thickness, the conventional approach shows a thickness reduction by 13.9%, which is greater than the value of 12.8% with the proposed one. In addition, the thickness standard deviation is significantly reduced by 19.8% when the proposed die design is applied in the multi-stage forming. The macro-scale simulation of full BPP channel demonstrated that the proposed die design approach reveals a noticeable enhancement in the formability of ultra-thin BPP by improving the thickness reduction and standard deviation.

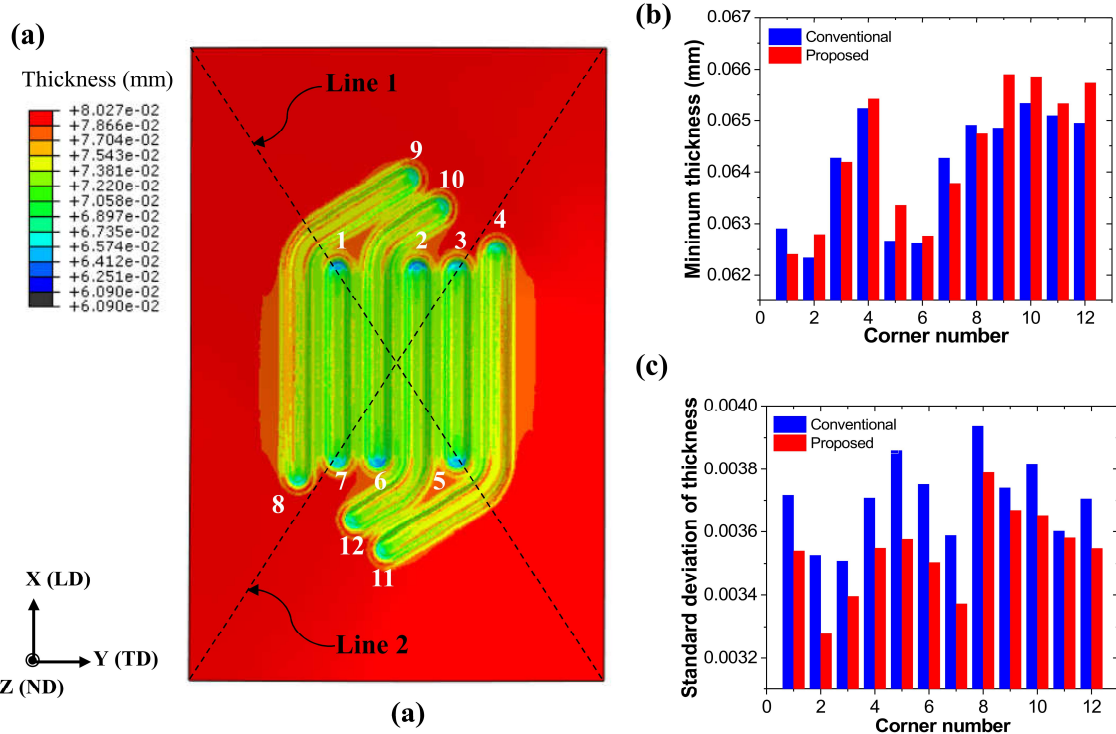


Fig. 6.18 3D finite element results of (a) contour plot of thickness distribution in the macro-scale BPP channel with the proposed die design approach and histogram of (b) minimum thickness and (c) standard deviation at twelve channel corners as indicated in Fig. 6.18(a).

Furthermore, Fig. 6.18 shows the contour plot of thickness distribution and histogram of minimum thickness and standard deviation at twelve corners of full channel BPP. In Fig. 6.18(a), the contour plot shows a uniform thickness distribution throughout the full channel BPP after multi-stage forming simulation using the proposed die approach. The results is consistent with the thickness distribution as revealed in Fig. 6.16. Figs. 6.18(b,c) show the minimum thickness and standard deviation at the twelve corners (Fig 6.18(a)) of full channel BPP compared between the conventional and proposed approaches. It reveals the overall improvement in the minimum thickness and standard deviation with the proposed die design approach. Such results further

confirm the efficiency of the novel die approach on the formability enhancement in the multi-stage forming of ultra-thin BBP for PEM fuel cell.

6.3.3.2. Influence on the springback behavior

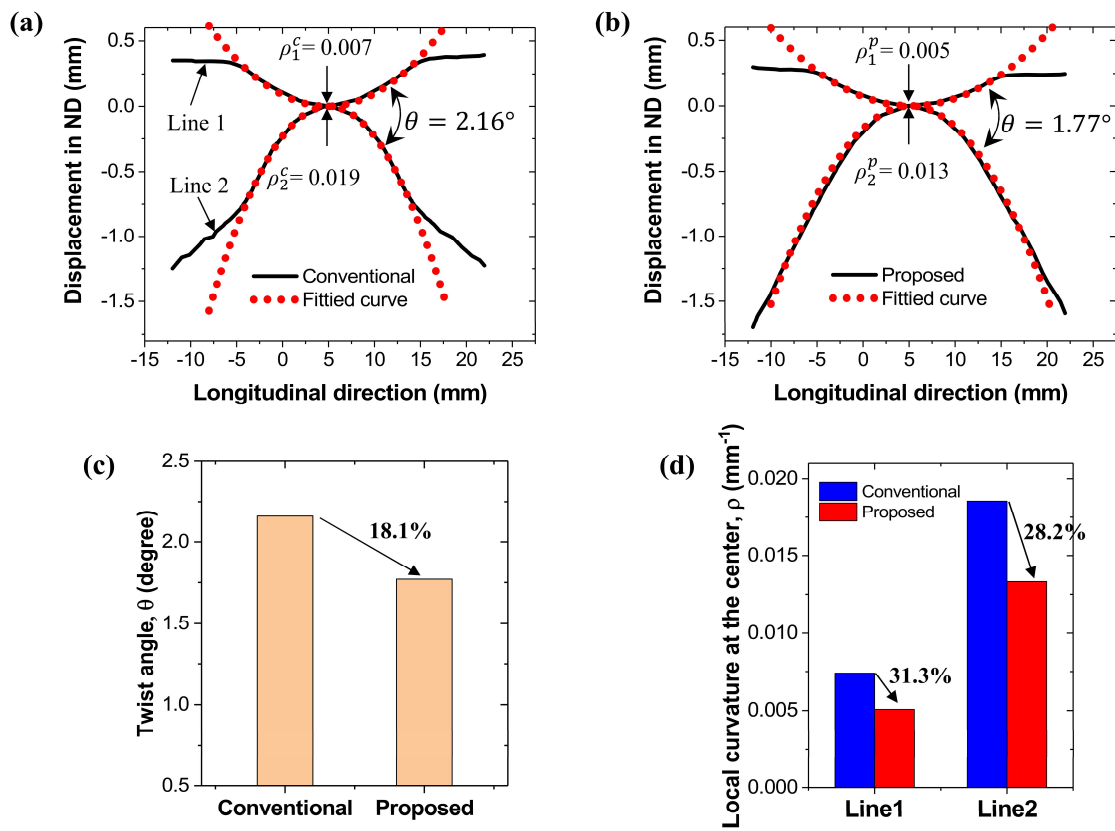


Fig. 6.19 3D finite element results of displacement in ND for the (a) conventional and (b) proposed die design approaches, and histograms of (c) twist angle and (d) local curvature at the center. Note that the results were measured along two representative lines as indicated in Fig. 6.18(a).

In the PEM system, springback behavior needs to be overcome since it affects the contact pressure between the membrane and interconnectors which is very important [155]. In addition,

leakage issues can be happened due to this geometric deviation. Particularly in the ultra-thin metallic BPP, its flexibility and springback commonly cause the shape error [156]. In the 3D FE analysis, therefore, the springback behavior was simulated by removing the die and punch tools in the unloading step. Then, the behavior of the material as twist springback and distortions can be investigated in a quantitative manner. Fig. 6.19 shows the twist angle and local curvature in the full channel BPP from the 3D simulations of multi-stage forming. Note that the results are measured along the two representative lines as indicated in Fig. 6.18(a).

Figs. 6.19(a,b) show the displacement in ND of both two representative lines along the longitudinal direction. Accordingly, the twist angle (θ , degree) and local curvature at the center position (ρ , mm^{-1}) can be obtained. Note that the local curvature is calculated using this equation, $\rho = 1/r_c$, where r_c is the radius of curvature. It reveals that the conventional design shows a twist angle of 2.16° , which is reduced to 1.77° for the proposed approach. In addition, the local curvatures for the line 1 and line 2 of 0.007 mm^{-1} and 0.019 mm^{-1} , respectively, for the conventional design are significantly reduced to 0.005 mm^{-1} and 0.013 mm^{-1} , respectively, for the proposed approach. Figs. 6.19(c,d) summarize the twist angle and local curvatures compared between the conventional and proposed die design approaches. It is apparent that the proposed approach shows a noticeable decrease in the twist angle by 18.1% and in the local curvature by 31.3% and 28.2% for the line 1 and line 2, respectively. The reduction in the twist angle and local curvature can reduce the effect of shape error (springback and distortions) on the contact pressure distribution, consequently improving the performance of PEM fuel cell.

6.3.3.3. Influence on the stress distribution

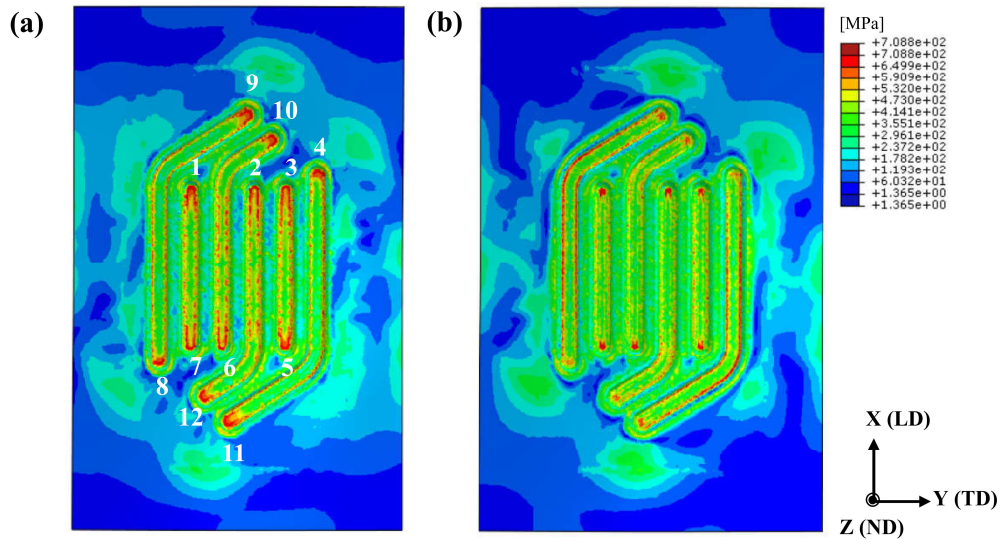


Fig. 6.20 3D finite element results of von Mises effective stress distributions in the macro-scale BPP channel compared between the (a) conventional and (b) proposed die design approaches.

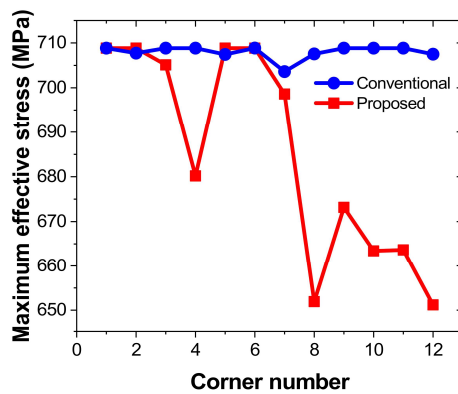


Fig. 6.21 Distribution of maximum effective stress at the twelve channel corners as indicated in Fig. 6.19 (a) compared between the conventional and proposed die design approaches.

Fig. 6.20 shows the von Mises stress distribution in the full channel BPP obtained from the 3D FE simulations of multi-stage forming. Fig. 6.20(a) shows that the full channel BPP using the conventional design exhibits the heterogenous stress distribution, particularly at the channel

corners. This can be responsible for the non-uniform thickness distribution and the significant thickness reduction, leading to the excessively localized thinning. In Fig. 6.20(b), however, the proposed approach reveals the decrease in stress heterogeneity, indicating more uniform stress distribution. This contributes to the uniform thickness distribution in addition to the improved thickness reduction, thus the local thinning is minimized to prevent the rupture.

Moreover, the maximum effective stresses at the twelve channel corners (Fig.6.20(a)) compared between the conventional and proposed die design approach are shown in Fig. 6.21. It is apparent found that the proposed die design approach results in a significant reduction in maximum stress concentration at the channel corners, leading to the reduction of serve thinning and the fracture.

6.4. Conclusions

This chapter investigated a two-step multi-stage forming process for the formability improvement of ultra-thin metallic BPP for proton exchange membrane (PEM) fuel cell. In order to induce the uniform thickness distribution, a novel die design approach was proposed for the preforming step in the multi-stage forming. The process design parameters of the proposed die approach were optimized by the developed artificial neural network (ANN) model integrated with the genetic algorithm (GA). Then, the multi-scale modelling of 2D finite element analysis (FEA) of micro-channel and 3D FEA of macro-scale channel were conducted to evaluate the effect of proposed die approach on the formability improvement in the ultra-thin metallic BPP. The following conclusions were drawn.

- (i) The ANN-GA model was successfully developed for accurate prediction and optimization of process design parameters in the proposed die design approach for multi-stage forming simulations.
- (ii) It revealed that the conventional approach resulted in the noticeable stress/strain heterogeneity while it was significantly reduced by using the proposed die design. This could reduce the onset of thinning concentration in the micro-channel BPP during the multi-stage forming process.
- (iii) Both the micro-channel and macro-scale BPP simulation results showed that the proposed die design approach showed the more uniform thickness distribution in addition to the improvement in the thickness reduction and standard deviation compared to the conventional one. Such results were responsible for the reduction of excessively localized thinning, consequently preventing the rupture due to the significant decrease in the stress concentration at the channel corners.
- (iv) The springback simulation with the proposed die design approach revealed a noticeable decrease in the twist angle (~18%) and the local curvature (~30%). Such a significant reduction could reduce the effect of shape error (springback and distortions) on the contact pressure distribution which was an important requirement in PEM fuel cell system.
- (v) It has been demonstrated that the proposed die design approach was feasible and effective for the formability improvement in the multi-stage forming of ultra-thin BPP for PEM fuel cell. In addition, this research suggested the beneficial method in the fabrication technologies of ultra-thin metallic BPP.

CHAPTER 7

SUMMARY AND CONCLUSIONS

The plastic deformation, material formability and failure behavior of metal polycrystals are significantly changes when the part size is scaled down to the micro scale. Such changes are yet challenging for both experiments and numerical simulations. This dissertation has presented the virtual material testing using crystal plasticity finite element method (CPFEM) as a robust and potential tool for remedying experimental approaches. The virtual material testing using CPFEM has applied to predict the formability and deformation behavior of ultra-thin ferritic stainless steel (FSS) sheet for bipolar plate in proton exchange membrane (PEM) fuel cell. The focuses have been on the investigations on the (1) mechanical behavior and yield loci, (2) forming limit diagram (FLD), (3) size effect on the formability, (4) free surface roughening effect on the formability, and (5) design of multi-stage forming process. The following conclusions are summarized from the main chapters, i.e., Chapter 2 ~ Chapter 6.

In Chapter 2, overview of kinematics and constitutive laws in the crystal plasticity finite element method (CPFEM) were briefly introduced. Then, the CPFEM was applied for predictions of mechanical behavior and yield loci of the ultra-thin FSS sheet for bipolar plate in PEM fuel cell. Uniaxial tensile tests and EBSD measurement were performed to characterize the macroscopic properties and the crystallographic texture of the material. By fitting the stress-strain curves through the CPFEM simulations of uniaxial tensile tests using representative volume element (RVE) considering the measured texture, the CPFEM hardening parameters were successfully identified. It revealed that the CPFEM model well reproduces the experimental stress-strain curves

along the RD, DD TD. Furthermore, the CPFEM prediction of yield loci was in good agreement with the experimental results and consistent with the results of Hill' 1948 and Yld2000-2d yield functions. In addition, the crystallographic texture significantly affected the yield loci of the material. Compared to the random texture, the measured texture resulted in the shaper yield loci which indicated the lower forming limit strains in the material.

In Chapter 3, the Nakazima test was performed to obtain the experimental FLD. The coupled CPFEM–MK model was developed to predict the FLD of ultra-thin FSS sheet under various loading paths ($-0.5 \leq \rho \leq 1$). The voxel-typed RVE considering the measured texture was used in this analysis. The effects of imperfection factor and initial material texture on the formability were investigated. In addition, the evaluation of FLD by the Hill's, Swift's and Hora's necking instability criterion (NIC) models without consideration of geometrical imperfection were also studied to assess the role of geometrical imperfection in the FLD prediction. The results showed that the CPFEM–MK model using the voxel-typed RVE well reproduced the experimental FLD. It revealed that the initial imperfection factor significantly affected the formability of ultra-thin FSS sheet in which the formability decreased with the imperfection factor. In addition, the formability of ultra-thin FSS sheet was strongly influence by the initial material texture. The results showed that predicted FLD using the measured texture was in good agreement with the experimental measurement compared to the random texture. It implied that for accurately reproducing the experimental FLD, the measured texture should be considered in the forming limit analysis of sheet metals. Furthermore, the capacity of MK model was comprehensively compared with the different NIC models for the FLD prediction. By consideration of geometrical constraint condition, the MK model well captured the entire of FLD curve while the NIC models could not.

It suggested that the geometrical imperfection in the sheet material can be considered as a fracture criterion in the ductile fracture model for simulating the material failure.

In Chapter 4, the realistic RVEs with various thickness-to-grain size ratio ($t/d = 2\sim 10$) were generated using a hybrid cellular automata–Monte Carlo (CA–MC) model by considering the measured texture and grain boundary misorientation distribution (GBMD) with a high fidelity. The CPFEM simulations of uniaxial tensile test using the realistic RVEs with various t/d revealed an apparent difference in macroscopic response between different average grain sizes. The result showed that the flow stress of the realistic RVE decreased with the increasing average grain size, indicating the grain size effect. In addition, the estimated grain boundary density significantly decreased as the average grain size increased, which could indirectly affect the decreased flow stress with the t/d ratio. The CPFEM–MK analysis of forming limit using the realistic RVEs revealed a significant size effect on the formability of ultra-thin FSS sheet. It revealed that the formability decreased with the increasing grain size (t/d reduced). The combined effects of geometry feature (thickness) and grain size could result in the size-dependent forming limit of ultra-thin FSS sheet. As the thickness-to-grain size ratio decreased, the overall deformation was predominantly governed by the surface grains since these surface grains were less constrained and deformed more easily. This played an important role in the size effect, leading to the increased stress and strain heterogeneities in the ultra-thin sheet material with a few grains through the thickness. For the coarse-grained RVE with low t/d , a primary distribution of strain hot spots in the surfaces was found, which could act as the geometrical imperfection to accelerate the failure after surface micro-cracks initiated. In addition, the through-thickness shear bands due to the less constraint of surface grains were apparently observed in the coarse-grained RVE with low thickness-to-grain size ratio, which played an important role in the material failure during the

deformation. Furthermore, the surface grains exhibited the high stress triaxiality as a consequence of the localized deformation and premature necking in the coarse-grained RVE. This attributed the decrease of forming limit strains to the early plastic flow instability in the RVE with low t/d .

In Chapter 5, the microstructural evolution during uniaxial tension was monitored by the in-situ EBSD technique. As the strain increased, the heterogeneous surface morphology was more significant due to the roughness, while the fractions of low angle grain boundaries (LAGBs) noticeable increased. The results showed that deformation twinning was unobservable, implying that the deformation was predominantly attributed to the dislocation slip only. With the increasing strain, the microstructure exhibited the increased KAM value and density of GND at the grain and sub-grain boundaries which could accommodate the plastic deformation. It was found that the formation of deformation-induced boundaries was responsible for the significant increase in the boundary density, leading to the dislocation piling-up that affected the deformation behavior of ultra-thin FSS sheet. The initial microstructure was then directly mapped onto the finite element mesh in the CPFEM simulation. The CPFEM predictions of stress and strain heterogeneities and the local hot spots of the ductile fracture initiation well matched with the experimental results. It was found that the localized deformation primarily distributed in the free surface grains which were less constrained and deformed easily, leading to the increased stress and strain heterogeneities. The results revealed that the damaging indicators increased with more fractions of high value as the strain increased, resulting in the onset of localized deformation. Furthermore, the free surface exhibited a considerable roughness due to the heterogeneous plastic deformation of grains under the applied strains. The high surface roughness was responsible for the increased thickness inhomogeneity which facilitated the strain localization, consequently the premature necking and fracture in the ultra-thin FSS sheet.

In Chapter 6, a two-step multi-stage forming simulation of ultra-thin metallic BPP for proton exchange membrane (PEM) fuel cell was investigated. In order to improve formability, a new die design approach was proposed for the preforming step in the multi-stage forming. Then, the artificial neural network (ANN) model integrated with the genetic algorithm (GA) were successfully developed for effectively optimizing the process design parameters of the proposed die approach. The 2D finite element (FE) simulation of micro-channel BPP revealed the noticeable stress/strain heterogeneity with the proposed die design, leading to the reduction in the onset of thinning concentration in the micro-channel BPP. In addition, the proposed die design approach showed the more uniform thickness distribution in addition to the improvement in the thickness reduction and standard deviation compared to the conventional one, as revealed from the 2D and 3D FE simulation results. This resulted in the reduction of excessively localized thinning, consequently preventing the rupture. Furthermore, a noticeable decrease in the twist angle ($\sim 18\%$) and the local curvature ($\sim 30\%$) were found in the full BPP channel with the proposed die design approach, thus reducing the effect of shape error (springback and distortions) on the contact pressure distribution which was an important requirement in PEM fuel cell system. It has been demonstrated that the proposed die design approach was feasible and effective for the formability improvement in the multi-stage forming of ultra-thin BPP for PEM fuel cell. In addition, this research suggested the beneficial method in the fabrication technologies of ultra-thin metallic BPP for PEM fuel cell.

REFERENCES

- [1] K. Xiong, W. Wu, S. Wang, L. Zhang, Modeling, design, materials and fabrication of bipolar plates for proton exchange membrane fuel cell: A review, *Appl. Energy*. 301 (2021) 117443.
- [2] A. Hermann, T. Chaudhuri, P. Spagnol, Bipolar plates for PEM fuel cells: A review, *Int. J. Hydrogen Energy*. 30 (2005) 1297–1302.
- [3] X. Yan, M. Hou, H. Zhang, F. Jing, P. Ming, B. Yi, Performance of PEMFC stack using expanded graphite bipolar plates, *J. Power Sources*. 160 (2006) 252–257.
- [4] C.A. Ramírez-Herrera, M.M. Tellez-Cruz, J. Pérez-González, O. Solorza-Feria, A. Flores-Vela, J.G. Cabañas-Moreno, Enhanced mechanical properties and corrosion behavior of polypropylene/multi-walled carbon nanotubes/carbon nanofibers nanocomposites for application in bipolar plates of proton exchange membrane fuel cells, *Int. J. Hydrogen Energy*. 46 (2021) 26110–26125.
- [5] Y. Leng, P. Ming, D. Yang, C. Zhang, Stainless steel bipolar plates for proton exchange membrane fuel cells: Materials, flow channel design and forming processes, *J. Power Sources*. 451 (2020) 227783.
- [6] S.-H. Wang, J. Peng, W.-B. Lui, Surface modification and development of titanium bipolar plates for PEM fuel cells, *J. Power Sources*. 160 (2006) 485–489.
- [7] H. Wang, M.A. Sweikart, J.A. Turner, Stainless steel as bipolar plate material for polymer electrolyte membrane fuel cells, *J. Power Sources*. 115 (2003) 243–251.

- [8] S. Joseph, J.C. McClure, P.J. Sebastian, J. Moreira, E. Valenzuela, Polyaniline and polypyrrole coatings on aluminum for PEM fuel cell bipolar plates, *J. Power Sources*. 177 (2008) 161–166.
- [9] C.-Y. Bai, T.-M. Wen, K.-H. Hou, M.-D. Ger, The bipolar plate of AISI 1045 steel with chromized coatings prepared by low-temperature pack cementation for proton exchange membrane fuel cell, *J. Power Sources*. 195 (2010) 779–786.
- [10] C.-H. Lin, S.-Y. Tsai, An investigation of coated aluminium bipolar plates for PEMFC, *Appl. Energy*. 100 (2012) 87–92.
- [11] R.F. Silva, D. Franchi, A. Leone, L. Pilloni, A. Masci, A. Pozio, Surface conductivity and stability of metallic bipolar plate materials for polymer electrolyte fuel cells, *Electrochim. Acta*. 51 (2006) 3592–3598.
- [12] V. V Nikam, R.G. Reddy, Corrosion studies of a copper–beryllium alloy in a simulated polymer electrolyte membrane fuel cell environment, *J. Power Sources*. 152 (2005) 146–155.
- [13] Y. Song, C. Zhang, C.-Y. Ling, M. Han, R.-Y. Yong, D. Sun, J. Chen, Review on current research of materials, fabrication and application for bipolar plate in proton exchange membrane fuel cell, *Int. J. Hydrogen Energy*. 45 (2020) 29832–29847.
- [14] S. Mahabunphachai, M. Koç, Fabrication of micro-channel arrays on thin metallic sheet using internal fluid pressure: Investigations on size effects and development of design guidelines, *J. Power Sources*. 175 (2008) 363–371.
- [15] J.-C. Hung, C.-C. Lin, Fabrication of micro-flow channels for metallic bipolar plates by a

- high-pressure hydroforming apparatus, *J. Power Sources*. 206 (2012) 179–184.
- [16] Y. Liu, L. Hua, Fabrication of metallic bipolar plate for proton exchange membrane fuel cells by rubber pad forming, *J. Power Sources*. 195 (2010) 3529–3535.
- [17] L. Peng, D. Liu, P. Hu, X. Lai, J. Ni, Fabrication of metallic bipolar plates for proton exchange membrane fuel cell by flexible forming process-numerical simulations and experiments, *J. Fuel Cell Sci. Technol.* 7 (2010) 0310091–0310099.
- [18] H.J. Bong, F. Barlat, M.-G. Lee, Probing formability improvement of ultra-thin ferritic stainless steel bipolar plate of PEMFC in non-conventional forming process, *Metall. Mater. Trans. A Phys. Metall. Mater. Sci.* 47 (2016) 4160–4174.
- [19] D. Qiu, L. Peng, P. Yi, X. Lai, W. Lehnert, Flow channel design for metallic bipolar plates in proton exchange membrane fuel cells: Experiments, *Energy Convers. Manag.* 174 (2018) 814–823.
- [20] S. Mahabunphachai, Ö.N. Cora, M. Koç, Effect of manufacturing processes on formability and surface topography of proton exchange membrane fuel cell metallic bipolar plates, *J. Power Sources*. 195 (2010) 5269–5277.
- [21] S.P. Keeler, Plastic instability and fracture in sheets, *ASM Trans.* 56 (1961) 25–48.
- [22] G.M. Goodwin, Application of strain analysis to sheet metal forming problems in the press shop, *SAE Tech. Pap.* 77 (1968) 380–387.
- [23] A. Gupta, M.B. Bettaieb, F. Abed-Meraim, S.R. Kalidindi, Computationally efficient predictions of crystal plasticity based forming limit diagrams using a spectral database, *Int. J. Plast.* 103 (2018) 168–187.

- [24] L. Mu, Z. Jia, Z. Ma, F. Shen, Y. Sun, Y. Zang, A theoretical prediction framework for the construction of a fracture forming limit curve accounting for fracture pattern transition, *Int. J. Plast.* 129 (2020) 102706.
- [25] J. Li, J.E. Carsley, T.B. Stoughton, L.G. Hector, S.J. Hu, Forming limit analysis for two-stage forming of 5182-O aluminum sheet with intermediate annealing, *Int. J. Plast.* 45 (2013) 21–43.
- [26] T.B. S-37. Stoughton, Elimination of the dependence of forming limits for AHSS on testing process conditions, Presented at 2017 Great Designs in Steel. Sponsored by American Iron and Steel Institute, n.d.
- [27] K. Nakazima, T. Kikuma, K. Hasuka, Study on the formability of steel sheets, *Yawata Tech Rep Sept.* (1968) 264 8517-8530 1968.
- [28] Z. Marciniak, K. Kuczyński, Limit strains in the processes of stretch-forming sheet metal, *Int. J. Mech. Sci.* 9 (1967) 609–620.
- [29] ISO12004-2, Metallic materials-Sheet and strip-Determination of forming limit curves Part 2: Determination of forming limit curves in laboratory, *Int. Organ. Stand.* (2008) 1–32.
- [30] H.J. Bong, F. Barlat, M.-G. Lee, D.C. Ahn, The forming limit diagram of ferritic stainless steel sheets: Experiments and modeling, *Int. J. Mech. Sci.* 64 (2012) 1–10.
- [31] J. Min, T.B. Stoughton, J.E. Carsley, J. Lin, Compensation for process-dependent effects in the determination of localized necking limits, *Int. J. Mech. Sci.* 117 (2016) 115–134.
- [32] Z. Chen, G. Fang, Determination of forming limit for aluminium alloy sheet eliminating the interferences of through-thickness stress and non-linear strain path, *IOP Conf. Ser. Mater.*

- Sci. Eng. 418 (2018).
- [33] H. Abdolvand, A.J. Wilkinson, On the effects of reorientation and shear transfer during twin formation: Comparison between high resolution electron backscatter diffraction experiments and a crystal plasticity finite element model, *Int. J. Plast.* 84 (2016) 160–182.
- [34] H. Abdolvand, M. Majkut, J. Oddershede, S. Schmidt, U. Lienert, B.J. Diak, P.J. Withers, M.R. Daymond, On the deformation twinning of Mg AZ31B: A three-dimensional synchrotron X-ray diffraction experiment and crystal plasticity finite element model, *Int. J. Plast.* 70 (2015) 77–97.
- [35] H.J. Bong, J. Lee, X. Hu, X. Sun, M.-G. Lee, Predicting forming limit diagrams for magnesium alloys using crystal plasticity finite elements, *Int. J. Plast.* 126 (2020) 102630.
- [36] A. Guery, F. Hild, F. Latourte, S. Roux, Slip activities in polycrystals determined by coupling DIC measurements with crystal plasticity calculations, *Int. J. Plast.* 81 (2016) 249–266.
- [37] D.-K. Kim, E.-Y. Kim, J. Han, W. Woo, S.-H. Choi, Effect of microstructural factors on void formation by ferrite/martensite interface decohesion in DP980 steel under uniaxial tension, *Int. J. Plast.* 94 (2017) 3–23.
- [38] C.Y. Sun, N. Guo, M.W. Fu, S.W. Wang, Modeling of slip, twinning and transformation induced plastic deformation for TWIP steel based on crystal plasticity, *Int. J. Plast.* 76 (2016) 186–212.
- [39] K. Sedighiani, V. Shah, K. Traka, M. Diehl, F. Roters, J. Sietsma, D. Raabe, Large-deformation crystal plasticity simulation of microstructure and microtexture evolution

- through adaptive remeshing, *Int. J. Plast.* 146 (2021) 103078.
- [40] P. Hu, Y. Liu, Y. Zhu, L. Ying, Crystal plasticity extended models based on thermal mechanism and damage functions: Application to multiscale modeling of aluminum alloy tensile behavior, *Int. J. Plast.* 86 (2016) 1–25.
- [41] B.H. Frodal, S. Thomesen, T. Børvik, O.S. Hopperstad, On the coupling of damage and single crystal plasticity for ductile polycrystalline materials, *Int. J. Plast.* 142 (2021).
- [42] J. Park, K. Lee, J.-H. Kang, J.-Y. Kang, S.H. Hong, S.W. Kwon, M.-G. Lee, Hierarchical microstructure based crystal plasticity-continuum damage mechanics approach: Model development and validation of rolling contact fatigue behavior, *Int. J. Plast.* 143 (2021) 103025.
- [43] C. Liu, P. Shanthraj, M. Diehl, F. Roters, S. Dong, J. Dong, W. Ding, D. Raabe, An integrated crystal plasticity-phase field model for spatially resolved twin nucleation, propagation, and growth in hexagonal materials, *Int. J. Plast.* 106 (2018) 203–227.
- [44] K.M. Min, W. Jeong, S.H. Hong, C.A. Lee, P.R. Cha, H.N. Han, M.-G. Lee, Integrated crystal plasticity and phase field model for prediction of recrystallization texture and anisotropic mechanical properties of cold-rolled ultra-low carbon steels, *Int. J. Plast.* 127 (2020) 102644.
- [45] J. Li, I. Romero, J. Segurado, Development of a thermo-mechanically coupled crystal plasticity modeling framework: Application to polycrystalline homogenization, *Int. J. Plast.* 119 (2019) 313–330.
- [46] D.S. Connolly, C.P. Kohar, W. Muhammad, L.G. Hector, R.K. Mishra, K. Inal, A coupled

- thermomechanical crystal plasticity model applied to Quenched and Partitioned steel, *Int. J. Plast.* 133 (2020) 102757.
- [47] F. Roters, P. Eisenlohr, L. Hantcherli, D.D. Tjahjanto, T.R. Bieler, D. Raabe, Overview of constitutive laws, kinematics, homogenization and multiscale methods in crystal plasticity finite-element modeling: Theory, experiments, applications, *Acta Mater.* 58 (2010) 1152–1211.
- [48] M. Kraska, M. Doig, D. Tikhomirov, D. Raabe, F. Roters, Virtual material testing for stamping simulations based on polycrystal plasticity, *Comput. Mater. Sci.* 46 (2009) 383–392.
- [49] C. Zhang, J. Ma, X. Liang, F. Luo, R. Cheng, F. Gong, Fabrication of metallic bipolar plate for proton exchange membrane fuel cells by using polymer powder medium based flexible forming, *J. Mater. Process. Technol.* 262 (2018) 32–40.
- [50] C. Wang, S. Xue, G. Chen, L. Cui, P. Zhang, Investigation on formability of bipolar plates during flexible micro forming of Cu/Ni clad foils, *J. Manuf. Process.* 53 (2020) 293–303.
- [51] Z. Xu, Z. Li, R. Zhang, T. Jiang, L. Peng, Fabrication of micro channels for titanium PEMFC bipolar plates by multistage forming process, *Int. J. Hydrogen Energy.* 46 (2021) 11092–11103.
- [52] R. Zhang, S. Lan, Z. Xu, D. Qiu, L. Peng, Investigation and optimization of the ultra-thin metallic bipolar plate multi-stage forming for proton exchange membrane fuel cell, *J. Power Sources.* 484 (2021) 229298.
- [53] M. Yang, X. Dong, R. Zhou, J. Cao, Crystal plasticity-based forming limit prediction for

- FCC materials under non-proportional strain-path, *Mater. Sci. Eng. A.* 527 (2010) 6607–6613.
- [54] J.H. Kim, M.-G. Lee, J.-H. Kang, C.-S. Oh, F. Barlat, Crystal plasticity finite element analysis of ferritic stainless steel for sheet formability prediction, *Int. J. Plast.* 93 (2017) 26–45.
- [55] B. Mohammed, T. Park, H. Kim, F. Pourboghrat, R. Esmailpour, The forming limit curve for multiphase advanced high strength steels based on crystal plasticity finite element modeling, *Mater. Sci. Eng. A.* 725 (2018) 250–266.
- [56] T. Park, L.G. Hector, X. Hu, F. Abu-Farha, M.R. Fellingner, H. Kim, R. Esmailpour, F. Pourboghrat, Crystal plasticity modeling of 3rd generation multi-phase AHSS with martensitic transformation, *Int. J. Plast.* 120 (2019) 1–46.
- [57] S. Isavand, M. Kardan-Halvaei, A. Assempour, Crystal plasticity modeling and experimental characterization of strain localization and forming limits in ferrite-pearlite steels, *Int. J. Solids Struct.* 233 (2021) 111205.
- [58] P. Zhang, C.P. Kohar, A.P. Brahme, S.H. Choi, R.K. Mishra, K. Inal, A Crystal Plasticity Formulation for Simulating the Formability of a Transformation Induced Plasticity Steel, *J. Mater. Process. Technol.* 287 (2021) 116493.
- [59] H.J. Bong, J. Lee, Crystal plasticity finite element–Marciniak-Kuczynski approach with surface roughening effect in predicting formability of ultra-thin ferritic stainless steel sheets, *Int. J. Mech. Sci.* 191 (2021) 106066.
- [60] W.L. Chan, M.W. Fu, J. Lu, J.G. Liu, Modeling of grain size effect on micro deformation

- behavior in micro-forming of pure copper, *Mater. Sci. Eng. A.* 527 (2010) 6638–6648.
- [61] S. Chen, X. Liu, L. Liu, Effects of grain size and heterogeneity on the mechanical behavior of foil rolling, *Int. J. Mech. Sci.* 100 (2015) 226–236.
- [62] H. Zhang, J. Liu, D. Sui, Z. Cui, M.W. Fu, Study of microstructural grain and geometric size effects on plastic heterogeneities at grain-level by using crystal plasticity modeling with high-fidelity representative microstructures, *Int. J. Plast.* 100 (2018) 69–89.
- [63] X. Shang, H. Zhang, Z. Cui, M.W. Fu, J. Shao, A multiscale investigation into the effect of grain size on void evolution and ductile fracture: Experiments and crystal plasticity modeling, *Int. J. Plast.* 125 (2020) 133–149.
- [64] M. Shakeri, A. Sadough, B.M. Dariani, Effect of pre-straining and grain size on the limit strains in sheet metal forming, *Proc. Inst. Mech. Eng. Part B J. Eng. Manuf.* 214 (2000) 821–827.
- [65] A. Assempour, R. Hashemi, K. Abrinia, M. Ganjiani, E. Masoumi, A methodology for prediction of forming limit stress diagrams considering the strain path effect, *Comput. Mater. Sci.* 45 (2009) 195–204.
- [66] Z.T. Xu, L.F. Peng, X.M. Lai, M.W. Fu, Geometry and grain size effects on the forming limit of sheet metals in micro-scaled plastic deformation, *Mater. Sci. Eng. A.* 611 (2014) 345–353.
- [67] Z.T. Xu, L.F. Peng, M.W. Fu, X.M. Lai, Size effect affected formability of sheet metals in micro/meso scale plastic deformation: Experiment and modeling, *Int. J. Plast.* 68 (2015) 34–54.

- [68] M. Weiss, P. Zhang, M.P. Pereira, B.F. Rolfe, D.E. Wilkosz, P.D. Hodgson, Understanding size effects and forming limits in the micro-stamping of industrial stainless steel foils, *Metals (Basel)*. 11 (2021) 1–21.
- [69] P. Chen, S.C. Mao, Y. Liu, F. Wang, Y.F. Zhang, Z. Zhang, X.D. Han, In-situ EBSD study of the active slip systems and lattice rotation behavior of surface grains in aluminum alloy during tensile deformation, *Mater. Sci. Eng. A*. 580 (2013) 114–124.
- [70] S. Sinha, J.A. Szpunar, N.A.P. Kiran Kumar, N.P. Gurao, Tensile deformation of 316L austenitic stainless steel using in-situ electron backscatter diffraction and crystal plasticity simulations, *Mater. Sci. Eng. A*. 637 (2015) 48–55.
- [71] W. Wang, T. Liu, X. Cao, Y. Lu, T. Shoji, In-situ observation on twin boundary evolution and crack initiation behavior during tensile test on 316L austenitic stainless steel, *Mater. Charact.* 132 (2017) 169–174.
- [72] K. Yvell, T.M. Grehk, P. Hedström, A. Borgenstam, G. Engberg, Microstructure development in a high-nickel austenitic stainless steel using EBSD during in situ tensile deformation, *Mater. Charact.* 135 (2018) 228–237.
- [73] S. Li, C. Guo, L. Hao, Y. Kang, Y. An, In-situ EBSD study of deformation behaviour of 600 MPa grade dual phase steel during uniaxial tensile tests, *Mater. Sci. Eng. A*. 759 (2019) 624–632.
- [74] X. Wu, H. Suo, Y. Ji, J. Li, L. Ma, M. Liu, Z. Zhang, Q. Wang, Systematical analysis on the grain orientation evolution of pure nickel under plastic deformation by using in-situ EBSD, *Mater. Sci. Eng. A*. 792 (2020) 139722.

- [75] S. Basak, S.K. Panda, Failure strains of anisotropic thin sheet metals: Experimental evaluation and theoretical prediction, *Int. J. Mech. Sci.* 151 (2019) 356–374.
- [76] L. Xu, F. Barlat, D.C. Ahn, J.D. Bressan, Forming limit and fracture mechanism of ferritic stainless steel sheets, *Mater. Sci. Eng. A.* 528 (2011) 3113–3121.
- [77] P. Zhang, M.P. Pereira, B. Abeyrathna, B.F. Rolfe, D.E. Wilkosz, P. Hodgson, M. Weiss, Plastic instability and fracture of ultra-thin stainless-steel sheet, *Int. J. Solids Struct.* 202 (2020) 699–716.
- [78] C. Sudarsan, K.S. Prasad, S. Hazra, S.K. Panda, Forming of serpentine micro-channels on SS304 and AA1050 ultra-thin metallic sheets using stamping technology, *J. Manuf. Process.* 56 (2020) 1099–1113.
- [79] Y. Wang, C. Zhang, Y. Yang, S. Fan, G. Wang, G. Zhao, L. Chen, The integration of through-thickness normal stress and friction stress in the M-K model to improve the accuracy of predicted FLCs, *Int. J. Plast.* 120 (2019) 147–163.
- [80] K. Chung, H. Kim, C. Lee, Forming limit criterion for ductile anisotropic sheets as a material property and its deformation path insensitivity. Part I: Deformation path insensitive formula based on theoretical models, *Int. J. Plast.* 58 (2014) 3–34.
- [81] K. Chung, C. Lee, H. Kim, Forming limit criterion for ductile anisotropic sheets as a material property and its deformation path insensitivity, Part II: Boundary value problems, *Int. J. Plast.* 58 (2014) 35–65.
- [82] C. Schwindt, F. Schlosser, M.A. Bertinetti, M. Stout, J.W. Signorelli, Experimental and Visco-Plastic Self-Consistent evaluation of forming limit diagrams for anisotropic sheet

- metals: An efficient and robust implementation of the M-K model, *Int. J. Plast.* 73 (2015) 62–99.
- [83] Z. Li, G. Zhou, D. Li, M.K. Jain, Y. Peng, P. Wu, Forming limits of magnesium alloy AZ31B sheet at elevated temperatures, *Int. J. Plast.* 135 (2020) 102822.
- [84] D. Kim, H. Kim, J.H. Kim, M.-G. Lee, K.J. Kim, F. Barlat, Y. Lee, K. Chung, Modeling of forming limit for multilayer sheets based on strain-rate potentials, *Int. J. Plast.* 75 (2015) 63–99.
- [85] A.S. Khan, M. Baig, Anisotropic responses, constitutive modeling and the effects of strain-rate and temperature on the formability of an aluminum alloy, *Int. J. Plast.* 27 (2011) 522–538.
- [86] D. Banabic, A. Kami, D.-S. Comsa, P. Eyckens, Developments of the Marciniak-Kuczynski model for sheet metal formability: A review, *J. Mater. Process. Technol.* 287 (2021) 116446.
- [87] H. Yao, J. Cao, Prediction of forming limit curves using an anisotropic yield function with prestrain induced backstress, *Int. J. Plast.* 18 (2002) 1013–1038.
- [88] P. Eyckens, A.V. Bael, P.V. Houtte, Marciniak-Kuczynski type modelling of the effect of Through-Thickness Shear on the forming limits of sheet metal, *Int. J. Plast.* 25 (2009) 2249–2268.
- [89] J. Cao, H. Yao, A. Karafillis, M.C. Boyce, Prediction of localized thinning in sheet metal using a general anisotropic yield criterion, *Int. J. Plast.* 16 (2000) 1105–1129.
- [90] K. Bandyopadhyay, M.-G. Lee, S.K. Panda, P. Saha, J. Lee, Formability assessment and failure prediction of laser welded dual phase steel blanks using anisotropic plastic properties,

- Int. J. Mech. Sci. 126 (2017) 203–221.
- [91] J. Lian, F. Shen, X. Jia, D.-C. Ahn, D.-C. Chae, S. Münstermann, W. Bleck, An evolving non-associated Hill48 plasticity model accounting for anisotropic hardening and r-value evolution and its application to forming limit prediction, *Int. J. Solids Struct.* 151 (2018) 20–44.
- [92] B.L. Ma, M. Wan, Z.Y. Cai, W.N. Yuan, C. Li, X.D. Wu, W. Liu, Investigation on the forming limits of 5754-O aluminum alloy sheet with the numerical Marciniak–Kuczynski approach, *Int. J. Mech. Sci.* 142–143 (2018) 420–431.
- [93] A.S. Khan, A. Pandey, T. Gnäupel-Herold, R.K. Mishra, Mechanical response and texture evolution of AZ31 alloy at large strains for different strain rates and temperatures, *Int. J. Plast.* 27 (2011) 688–706.
- [94] B. Klusemann, B. Svendsen, H. Vehoff, Modeling and simulation of deformation behavior, orientation gradient development and heterogeneous hardening in thin sheets with coarse texture, *Int. J. Plast.* 50 (2013) 109–126.
- [95] K. Yoshida, T. Ishizaka, M. Kuroda, S. Ikawa, The effects of texture on formability of aluminum alloy sheets, *Acta Mater.* 55 (2007) 4499–4506.
- [96] P.D. Wu, S.R. MacEwen, D.J. Lloyd, K.W. Neale, Effect of cube texture on sheet metal formability, *Mater. Sci. Eng. A.* 364 (2004) 182–187.
- [97] K. Inal, K.W. Neale, A. Aboutajeddine, Forming limit comparisons for FCC and BCC sheets, *Int. J. Plast.* 21 (2005) 1255–1266.
- [98] T.O. Erinosh, A.C.F. Cocks, F.P.E. Dunne, Coupled effects of texture, hardening and non-

- proportionality of strain on ductility in ferritic steel, *Comput. Mater. Sci.* 80 (2013) 113–122.
- [99] J.-T. Gau, C. Principe, J. Wang, An experimental study on size effects on flow stress and formability of aluminum and brass for microforming, *J. Mater. Process. Technol.* 184 (2007) 42–46.
- [100] O. Amelirad, A. Assempour, Experimental and crystal plasticity evaluation of grain size effect on formability of austenitic stainless steel sheets, *J. Manuf. Process.* 47 (2019) 310–323.
- [101] H. Hoffmann, S. Hong, Tensile test of very thin sheet metal and determination of flow stress considering the scaling effect, *CIRP Ann. - Manuf. Technol.* 55 (2006) 263–266.
- [102] E. Schmid, Neuere untersuchungen an metallkristallen, in: *Proc. Int. Congr. Appl. Mech.*, 1924: pp. 342–353.
- [103] T.G. I., Plastic strain in metals, *J. Inst. Met.* 62 (1938) 307–324.
- [104] A.S. Argon, Strengthening Mechanisms in Crystal Plasticity, in: 2007.
- [105] J.R. Rice, Inelastic constitutive relations for solids: an internal-variable theory and its application to metal plasticity, *J. Mech. Phys. Solids.* 19 (1971) 433–455.
- [106] R.J. Asaro, Geometrical effects in the inhomogeneous deformation of ductile single crystals, *Acta Metall.* 27 (1979) 445–453.
- [107] D. Peirce, R.J. Asaro, A. Needleman, Material rate dependence and localized deformation in crystalline solids, *Acta Metall.* 31 (1983) 1951–1976.

- [108] S.B. Brown, K.H. Kim, L. Anand, An internal variable constitutive model for hot working of metals, *Int. J. Plast.* 5 (1989) 95–130.
- [109] Y. Huang, A User-Material Subroutine Incorporating Single Crystal Plasticity in the ABAQUS Finite Element Program, in: 1991.
- [110] J. Kim, K. Jo, Y. Kim, J. Lee, Y. Lee, J. Kim, J. Seok, Stainless steel for polymer fuel cell separator and method for preparing same, 2016.
- [111] D. Raabe, K. Luecke, Influence of particles on recrystallization textures of ferritic stainless steels, *Steel Res.* 63 (1992) 457–464.
- [112] K.-M. Lee, M.-Y. Huh, S. Park, O. Engler, Effect of texture components on the lankford parameters in ferritic stainless steel sheets, *ISIJ Int.* 52 (2012) 522–529.
- [113] J.P. Hirth, J. Lothe, *Theory of dislocations*, McGraw-Hill, New York. (1969).
- [114] C. Zhang, L.-W. Zhang, W.-F. Shen, Y.-N. Xia, Y.-T. Yan, 3D crystal plasticity finite element modeling of the tensile deformation of polycrystalline ferritic stainless steel, *Acta Metall. Sin. (English Lett.* 30 (2017) 79–88.
- [115] R. Hill, A theory of the yielding and plastic flow of anisotropic metals, *Proc. R. Soc. London A Math. Phys. Eng. Sci. R. Soc.* (1948) 281–297.
- [116] F. Barlat, J.C. Brem, J.W. Yoon, K. Chung, R.E. Dick, D.J. Lege, F. Pourboghrat, S.H. Choi, E. Chu, Plane stress yield function for aluminum alloy sheets - Part 1: Theory, *Int. J. Plast.* 19 (2003) 1297–1319.
- [117] S. Xu, K.J. Weinmann, Prediction of forming limit curves of sheet metals using Hill's 1993

- user-friendly yield criterion of anisotropic materials, *Int. J. Mech. Sci.* 40 (1998) 913–925.
- [118] F. Barlat, Crystallographic texture, anisotropic yield surfaces and forming limits of sheet metals, *Mater. Sci. Eng.* 91 (1987) 55–72.
- [119] A. Parmar, P.B. Mellor, Predictions of limit strains in sheet metal using a more general yield criterion, *Int. J. Mech. Sci.* 20 (1978) 385–391.
- [120] W.F. Hosford, On yield loci of anisotropic cubic metals, *Proc. 7th North Am. Met. Work. Res. Conf. Soc. Manuf. Eng. Dearborn, Michigan.* (1979) 191–196.
- [121] R.W. Logan, W.F. Hosford, Upper-bound anisotropic yield locus calculations assuming $\langle 111 \rangle$ -pencil glide, *Int. J. Mech. Sci.* 22 (1980) 419–430.
- [122] R. Hill, On discontinuous plastic states, with special reference to localized necking in thin sheets, *J. Mech. Phys. Solids.* 1 (1952) 19–30.
- [123] H.W. Swift, Plastic instability under plane stress, *J. Mech. Phys. Solids.* 1 (1952) 1–18.
- [124] P. Hora, L. Tong, J. Reissner, A prediction method for ductile sheet metal failure in Fe-simulation, *Proc. Numisheet.* 11 (1996) 252–256.
- [125] K.W. Neale, E. Chater, Limit strain predictions for strain-rate sensitive anisotropic sheets, *Int. J. Mech. Sci.* 22 (1980) 563–574.
- [126] D. Morales-Palma, A.J. Martínez-Donaire, C. Vallengano, On the use of maximum force criteria to predict localised necking in metal sheets under stretch-bending, *Metals (Basel).* 7 (2017).
- [127] J.K. Mason, J. Lind, S.F. Li, B.W. Reed, M. Kumar, Kinetics and anisotropy of the Monte

- Carlo model of grain growth, *Acta Mater.* 82 (2015) 155–166.
- [128] S. Raghavan, S.S. Sahay, Modeling the grain growth kinetics by cellular automaton, *Mater. Sci. Eng. A.* 445–446 (2007) 203–209.
- [129] M. Jedrychowski, B. Bacroix, J. Tarasiuk, S. Wroński, Monte Carlo modelling of recrystallization in alpha Zirconium, *Comput. Mater. Sci.* 199 (2021).
- [130] D.-K. Kim, W. Woo, W.-W. Park, Y.-T. Im, A. Rollett, Mesoscopic coupled modeling of texture formation during recrystallization considering stored energy decomposition, *Comput. Mater. Sci.* 129 (2017) 55–65.
- [131] F. Chen, H. Zhu, W. Chen, H. Ou, Z. Cui, Multiscale modeling of discontinuous dynamic recrystallization during hot working by coupling multilevel cellular automaton and finite element method, *Int. J. Plast.* 145 (2021) 103064.
- [132] D.-K. Kim, H.W. Lee, K.-H. Jung, Y.-T. Im, Mesoscopic modeling of primary recrystallization of AA1050 with curvature-driven interface migration effect, *Mater. Trans.* 54 (2013) 81–89.
- [133] J.B. Allen, C.F. Cornwell, B.D. Devine, C.R. Welch, Simulations of anisotropic grain growth in single phase materials using Q-state Monte Carlo, *Comput. Mater. Sci.* 71 (2013) 25–32.
- [134] H. Li, X. Sun, H. Yang, A three-dimensional cellular automata-crystal plasticity finite element model for predicting the multiscale interaction among heterogeneous deformation, DRX microstructural evolution and mechanical responses in titanium alloys, *Int. J. Plast.* 87 (2016) 154–180.

- [135] E. Popova, Y. Staraselski, A. Brahme, R.K. Mishra, K. Inal, Coupled crystal plasticity - Probabilistic cellular automata approach to model dynamic recrystallization in magnesium alloys, *Int. J. Plast.* 66 (2015) 85–102.
- [136] O. Diard, S. Leclercq, G. Rousselier, G. Cailletaud, Evaluation of finite element based analysis of 3D multicrystalline aggregates plasticity Application to crystal plasticity model identification and the study of stress and strain fields near grain boundaries, *Int. J. Plast.* 21 (2005) 691–722.
- [137] J. Segurado, J. Llorca, Simulation of the deformation of polycrystalline nanostructured Ti by computational homogenization, *Comput. Mater. Sci.* 76 (2013) 3–11.
- [138] J.Z. Gronostajski, Z. Zimniak, The effect of changing of heterogeneity with strain on the forming limit diagram, *J. Mater. Process. Tech.* 34 (1992) 457–464.
- [139] Y. Lou, J.W. Yoon, H. Huh, Modeling of shear ductile fracture considering a changeable cut-off value for stress triaxiality, *Int. J. Plast.* 54 (2014) 56–80.
- [140] W. Li, S. Yamasaki, M. Mitsuhara, H. Nakashima, In situ EBSD study of deformation behavior of primary α phase in a bimodal Ti-6Al-4V alloy during uniaxial tensile tests, *Mater. Charact.* 163 (2020) 110282.
- [141] M. Calcagnotto, D. Ponge, E. Demir, D. Raabe, Orientation gradients and geometrically necessary dislocations in ultrafine grained dual-phase steels studied by 2D and 3D EBSD, *Mater. Sci. Eng. A.* 527 (2010) 2738–2746.
- [142] A. Kundu, D.P. Field, Influence of plastic deformation heterogeneity on development of geometrically necessary dislocation density in dual phase steel, *Mater. Sci. Eng. A.* 667

- (2016) 435–443.
- [143] B. Meng, M.W. Fu, Size effect on deformation behavior and ductile fracture in microforming of pure copper sheets considering free surface roughening, *Mater. Des.* 83 (2015) 400–412.
- [144] O. Wouters, W.P. Vellinga, R. van Tijum, J.T.M. De Hosson, Effects of crystal structure and grain orientation on the roughness of deformed polycrystalline metals, *Acta Mater.* 54 (2006) 2813–2821.
- [145] M.T. Tran, H. Wang, H.W. Lee, D.-K. Kim, Crystal plasticity finite element analysis of size effect on the formability of ultra-thin ferritic stainless steel sheet for fuel cell bipolar plate, *Int. J. Plast.* 154 (2022) 103298.
- [146] Q. Hu, D. Zhang, H. Fu, K. Huang, Investigation of stamping process of metallic bipolar plates in PEM fuel cell - Numerical simulation and experiments, *Int. J. Hydrogen Energy.* 39 (2014) 13770–13776.
- [147] X. Li, S. Lan, Z. Xu, T. Jiang, L. Peng, Thin metallic wave-like channel bipolar plates for proton exchange membrane fuel cells: Deformation behavior, formability analysis and process design, *J. Power Sources.* 444 (2019) 227217.
- [148] N. Nakagaki, *The newly developed components for the fuel cell vehicle*, Mirai, 2015.
- [149] H.J. Bong, F. Barlat, J. Lee, M.G. Lee, J.H. Kim, Application of central composite design for optimization of two-stage forming process using ultra-thin ferritic stainless steel, *Met. Mater. Int.* 22 (2016) 276–287.
- [150] H.J. Bong, J. Lee, J.H. Kim, F. Barlat, M.G. Lee, Two-stage forming approach for

- manufacturing ferritic stainless steel bipolar plates in PEM fuel cell: Experiments and numerical simulations, *Int. J. Hydrogen Energy*. 42 (2017) 6965–6977.
- [151] R. Zhang, Z. Xu, L. Peng, X. Lai, M.W. Fu, Modelling of ultra-thin steel sheet in two-stage tensile deformation considering strain path change and grain size effect and application in multi-stage microforming, *Int. J. Mach. Tools Manuf.* 164 (2021).
- [152] S.W. Choi, S.H. Park, H.S. Jeong, J.R. Cho, S. Park, M.Y. Ha, Improvement of formability for fabricating thin continuously corrugated structures in sheet metal forming process, *J. Mech. Sci. Technol.* 26 (2012) 2397–2403.
- [153] S. Xu, K. Li, Y. Wei, W. Jiang, Numerical investigation of formed residual stresses and the thickness of stainless steel bipolar plate in PEMFC, *Int. J. Hydrogen Energy*. 41 (2016) 6855–6863.
- [154] M.T. Tran, Z. Shan, H.W. Lee, D.K. Kim, Earing reduction by varying blank holding force in deep drawing with deep neural network, *Metals (Basel)*. 11 (2021) 1–23.
- [155] K. Karacan, S. Celik, S. Toros, M. Alkan, U. Aydin, Investigation of formability of metallic bipolar plates via stamping for light-weight PEM fuel cells, *Int. J. Hydrogen Energy*. 45 (2020) 35149–35161.
- [156] D. Qiu, P. Yi, L. Peng, X. Lai, Study on shape error effect of metallic bipolar plate on the GDL contact pressure distribution in proton exchange membrane fuel cell, *Int. J. Hydrogen Energy*. 38 (2013) 6762–6772.

PUBLICATIONS

- [1] **M.T. Tran**, H. Wang, H.W. Lee, D.-K. Kim, Crystal plasticity finite element analysis of size effect on the formability of ultra-thin ferritic stainless steel sheet for fuel cell bipolar plate, *International Journal of Plasticity* 154, (2022), 103298.
- [2] **M.T. Tran**, T.H. Nguyen, D.-K. Kim, W. Woo, S.-H. Choi, H.W. Lee, H. Wang, Effect of hot isostatic pressing on the cryogenic mechanical properties of CrCoNi medium entropy alloy processed by direct energy deposition, *Materials Science and Engineering A* 828, (2021), 142110.
- [3] **M.T. Tran**, Z. Shan, H.W. Lee, D.-K. Kim, Earing reduction by varying blank holding force in deep drawing with deep neural network, *Metals* 11, (2021), 395.
- [4] H.W. Lee, K.-J. Yu, **M.T. Tran**, I.-Y. Moon, Y.-S. Oh, S.-H. Kang, D.-K. Kim, Effect of quenching tempering-post weld heat treatment on microstructure and mechanical properties of laser-arc hybrid welded boron steel, *Materials* 12, (2019) 2862.
- [5] **M. T. Tran**, S.-K. Hwang, H. W. Lee and D.-K. Kim, Effect of free surface roughening on the micromechanical deformation and ductile failure of ultra-thin steel sheet by in-situ EBSD and crystal plasticity simulation, to be submitted.
- [6] **M.T. Tran**, D.H. Lee, H.W. Lee, D.-K. Kim, Formability improvement in multi-stage stamping of ultra-thin metallic bipolar plate for PEM fuel cell, to be submitted.

CURRICULUM VITAE

Name: Minh Tien Tran

2019.03 – 2022.08 Ph.D Degree

Graduate School of Mechanical Engineering

University of Ulsan, Korea

2017.04 – 2019.02 Production Engineer

Department of Assembly

II-VI Viet Nam Co., Ltd, Vietnam

2015.05 – 2016.12 Master Degree

Department of Mechanical Engineering

University of Technology and Education HCM City, Vietnam

2013.12 – 2015.05 Production Control Engineer

Department of Production Management

Maruei Viet Nam Precision Co., Ltd, Vietnam

2009.09 – 2013.08 Bachelor Degree

Department of Mechanical Engineering

University of Technology and Education HCM City, Vietnam